UNIVERSITY COLLEGE LONDON

DEPARTMENT OF PHYSICS AND ASTRONOMY

Thesis submitted for the degree

Doctor of Philosophy (PhD)

Defended by

Mattia Mena

Dynamic correlations in model quantum magnets in various dimensions investigated with neutron scattering

Thesis Supervisor: Prof Desmond F. McMorrow

Subsidiary Supervisor: Prof Christian Rüegg

Referees :

Prof A. Green - University College London

Dr E. Blackburn - University of Birmingham

Fall 2016

I, Mattia Mena confirm that the work presented in this thesis is my own. Where information has been derived from other sources, I confirm that this has been indicated in the thesis.

Mattia Mena	Date

Abstract

Several properties of a system of correlated spins contribute to the macroscopic behaviour, and amongst them are those of quantum versus classical magnetism, frustration or dimensionality of the system, Ising or Heisenberg interactions, which on their own can lead to a rich and diverse phenomenology. This thesis investigates three materials in order to explain the diverse manifestation of their magnetic excitations and relate it to their physical properties.

The excited spectrum of an ideal antiferromagnetic Ising chain is either bow-tie-shaped continua or a series of discrete cosine-like modes, depending on the presence or absence of a staggered magnetic field. In one physical realization of this system, the hexagonal halide $RbCoCl_3$, which possesses three distinct magnetic phases, both a continuum and discrete Ising spins are observed in the lowest ordered magnetic phase, while only a continuum is found in the other phases. We propose that this is due to the nearest and next-nearest interactions perpendicular to the plane, which lead to either long-range or short-range order. In this compound an unstaggered ordered Ising chain can be observed down to 0 K, allowing for studies of the thermal Ising chain and providing a material where the effect of frustration can be tuned with temperature and affects the dispersion.

In the ferromagnetic insulating pyrochlore $Lu_2V_2O_7$ magnons display a novel thermal equivalent of the Hall effect induced by the Dzyaloshinskii-Moriya interaction (DMI). In an in-depth study of its spectrum, we have measured the full spectrum of $Lu_2V_2O_7$ and confirmed that a minimal Hamiltonian is sufficient to describe it, obtaining the ratio between the ferromagnetic interaction and the DMI, which is the parameter controlling the magnon Hall effect.

$SrCu_2(BO_3)_2$ is a two-dimensional frustrated square compound where the spins form antiferromagnetic dimerized singlets whose elementary excitation is an intra-dimeric singlet-to-triplet transition. Temperature causes

the excited spectrum to decrease in intensity at a temperature much lower than the gap. The exchange between the polarized shells created around the dimers has been suggested to provide the main decay channel for the excited triplets. In this thesis we investigate the $\vec{Q}$-dependence of this decay channel.

Only part of the results summarized in this thesis have been published, in a PRL paper on the magnon dispersion of $Lu_2V_2O_7$ of which I am first author. I am currently drafting a paper on $RbCoCl_3$, with an additional paper authored by N. Hänni on the subject having been already submitted to PRL. Furthermore, I am collaborating on a joint publication on $SrCu_2(BO_3)_2$ with D. Lançon.

Contents

List of Figures

List of Tables

Chapter 1

Introduction on Magnetism

1.1 Classical Magnetism

Electromagnetism is one of the four fundamental forces of the universe, along with the nuclear strong, nuclear weak and gravitational interaction. It couples electrical and magnetic charges. Amongst many excellent books on the topic, noteworthy texts are J. Jackson's *Classical Electrodynamics* [1] or R. Feynman's *Lectures on Physics* [2].

Classical electromagnetism, one of the most important historical branches of physics, culminated with Maxwell's equations, which express relations between the electrical field $\vec{E}$ and the magnetic field $\vec{B}$ (shown here in SI units) [3, 4]:

$$\begin{aligned}
\nabla \cdot \vec{E} &= \frac{\rho}{\epsilon_0}, \\
\nabla \cdot \vec{B} &= 0, \\
\nabla \times \vec{E} &= -\frac{\partial \vec{B}}{\partial t}, \\
\nabla \times \vec{B} &= \mu_0(\vec{J} + \epsilon_0 \frac{\partial \vec{E}}{\partial t}),
\end{aligned}$$

where ρ is the spatial density of electrical charges, ϵ_0 is the permittivity of free space, μ_0 is the permeability of free space and $\vec{J}$ is an electrical current (i.e. a drift through space of electrical charges).

Interestingly, in his original 1865 paper, Maxwell formulated a set of 20 equations, since he didn't use vectors and included additional laws such as

Ohm's $J = \sigma E$ (curiously, Maxwell himself in 1879 edited Henry Cavendish's unpublished notes into a book and found that Cavendish had discovered Ohm's law 50 years earlier than Ohm had [5]). The first person to write Maxwell's equations as we know them today is, thus, not Maxwell but Oliver Heaviside in 1892 [6].

These fields are used to calculate the Lorentz force, i.e. the force experienced by a charged object via its electromagnetic interaction:

$$\vec{F} = q(\vec{E} + \vec{v} \times \vec{B})$$

where q is the charge and $\vec{v}$ is the velocity of the particle. While this law was written in this form to Lorentz in 1893, the contribution of the magnetic field was first derived by Heaviside in 1889 [7].

A magnetic object in an external magnetic field experiences a potential energy $U = -\vec{\mu} \cdot \vec{B}$ where μ is the magnetic moment. This interaction will appear throughout this work as the Zeeman coupling.

Understanding the nature of the magnetic moment in microscopic terms turned out to be difficult for the classical theory of electromagnetism. A dipolar electrical term is written as $\vec{p} = q\vec{l}$, where $\vec{l}$ is the vector separating the two monopoles. However a similar formulation of $\vec{\mu}$ in terms of two spatially separated monopoles is impossible since no magnetic monopole can exist due to Maxwell's second law and hence $\vec{l}$ cannot be non-zero.

This is not a problem for magnetic fields that are generated by currents: an electrical charge that rotates around a loop has an angular momentum $\vec{L}$ and creates a circular current $\vec{J}$, and its magnetic moment is $\vec{\mu} = \gamma\vec{L}$, where γ is the gyromagnetic ratio.

1.2 Spins in Quantum Physics

When it became apparent that electrons possess an intrinsic magnetic moment that cannot be explained in terms of currents, a new fundamental

quantum number was introduced relating to the spin angular momentum operator. The expectation of the square of the total spin angular momentum $\langle \hat{\mathbf{S}} \cdot \hat{\mathbf{S}} \rangle = \hbar S(S+1)$, where S is the total spin quantum number (for electrons, $S = 1/2$). This is related to the spin magnetic moment $\vec{\mu}_S$ via $|\vec{\mu}_S| = 2\mu_B\sqrt{S(S+1)}$, where $\mu_B = e\hbar/2m_e$ is the Bohr magneton. Being a quantum number, the spin operator obeys commutation relations $[\hat{S}_j, \hat{S}_k] = i\hbar\,\epsilon_{jkl}\hat{S}_l$, where ϵ_{jkl} is the Civita-Levi symbol and $\hbar$ the reduced Planck constant. A further magnetic quantum number, the projection m_S, is allowed to have values between $-S$ and S in steps of 1, meaning that for an electron it can only take the values of $-1/2$ and $1/2$ (*spin up* and *spin down*).

Atoms then have a total spin quantum number, which is the sum of the individual spin quantum numbers. In filling an orbital shell (of azimuthal quantum number l), each sub-orbital level (of magnetic quantum number $m \in$ [-l, l]) can host at most two electrons of opposite spins, and Hund's rule predicts that in order to minimize energy electrons will avoid being in the same sublevel if there is an empty sublevel, and will have the same spin direction if they are in half-filled sublevels. This means that the total spin will be zero on a filled shell and will be maximal on a half-filled shell: For instance a half-filled p shell ($l = 2$) will have 5 unpaired electrons, and a total spin of $5/2$. As a consequence, not all elements and compounds present strong magnetic properties: especially if elements bond ionically and lose or gain electrons to form an empty or filled shell, which is magnetically inert.

1.3 Solid State Magnetism

The scientific questions in this thesis are going to be centred on aspects of quantum ($S = 1/2$) magnetism in solid state theory, for which it is important to define a certain number of properties.

In the context of solid state physics, explaining the macroscopic magnetic properties of a material is often achieved by understanding it as an array of interacting spins. The interactions originate not from the direct

electromagnetic exchange between electrons, but rather is ultimately motivated by Pauli's exclusion principle: the wave functions of single electrons in a solid-state system can present substantial overlap – which is important when considering pairs of neighbouring electrons and their quantum numbers. Depending on the specific wave function of the pair (which is antisymmetric with respect to the exchange of particles since it is a system of fermions) and on material-specific parameters, the ground state will require the electrons to be parallel - or antiparallel - and the first excited state will determine the energy required to flip a spin (i.e. to allow two spins to have antiparallel, or parallel, spins without all of their quantum numbers being otherwise the same). This is called an exchange energy.

A simple bilinear formulation of an interactive spin Hamiltonian is:

$$\mathcal{H} = \sum_{j,k} \vec{S}_j^{\dagger} \boldsymbol{J}_{j,k} \vec{S}_k + \sum_j \vec{H}_j \cdot \vec{S}_j$$

where j, k are indexes of all the magnetic sites of the system, and $\boldsymbol{J}_{j,k}$ is the exchange matrix, whose special cases are going to be discussed later, and the second term is the Zeeman energy. Additional exchanges can be introduced, such as a quadratic S_j^2, to go beyond this linear model, but corrections of this sort are not going to be discussed here.

This general expression couples each spin j in the system with every other spin k, but often the Hamiltonian is simplified to contain only the most dominant interactions: in the most usual case, only the nearest-neighbour (nn) coupling is preserved (i.e. $S_{j,k} = 0$ if $|k - j| > 1$). Further terms, such as the next-nearest neighbour (nnn) and so on, can be included.

Many magnetic systems feature ordered states (i.e. long-range ground states of the Hamiltonian) that minimize the energy. These ordered states can exist only below a certain critical temperature T_C, above which the system becomes disordered (i.e. a phase transition). Examples of famous ordered magnetic states include the ferromagnetic and antiferromagnetic configurations, i.e. all spins lying parallel or antiparallel respectively to their

neighbours. A phase transition is usually described with an *order parameter*, a physical property that is zero above the phase transition and non-zero below it. Good order parameters for a ferromagnet are the magnetization or the intensity of a magnetic Bragg reflection, i.e. a Bragg reflection that is due to the periodic order of the magnetic lattice (see the next chapter for more information on Bragg peaks).

Furthermore, many magnetic systems possess distinctive magnetic quantized excitations, such as spin waves or solitons. These excitations are generally observed only below T_C. While phonons are naturally gapless Goldstone modes (i.e. there is at least one phonon branch whose excitation energy goes to zero for $\vec{Q}$, its wave vector, going to zero), magnetic excitations are divided between gapless and gapped (i.e. no excited state, at any propagation vector, has an energy lower than the gap energy Δ).

1.3.1 Dimensionality of the system

While what was discussed in the previous section applies best to three-dimensional systems, changing the geometrical properties of the lattice can change the behaviour of a magnetic system drastically.

When the magnetic terms are aligned along chains so that the only non-negligeable interaction is between sites in the same chain (e.g. the nearest-neighbour distance between sites in the chain is much smaller than any other distance between sites), the system will be dominated by the in-chain exchanges, leading to a *one-dimensional* (1D) material. Similarly, when ions have non-negligeable interactions with other ions on a specific plane, but negligeable interactions to ions on a parallel plane, the system is called *two-dimensional* (2D). Only network of exchanges where ions have non-negligeable interactions along all crystallographic directions leads to a *three-dimensional* (3D) exchange. Intermediate stages also exist, such as ladder systems (i.e. systems of coupled chains, which are between 1D and 2D).

A number of physical properties can change depending on the symmetry

and the dimensionality. For instance, a 3D system with ferromagnetic Ising interactions (explained in the next section) possesses a long-range ordered (LRO) phase (at temperatures below T_C) while an ideal 1D systems doesn't even at 0 K, and can at most display short-range order (SRO). This will be discussed in a later chapter.

1.3.2 Spins: Heisenberg, XY and Ising exchanges

The spins of free electrons have three components, $S_{x,y,z}$, of which only one (conventionally along the magnetization axis z) can be observed. This is not necessarily true of the spins in solid state physics, where the "free" spin is not necessarily a quantum number.

The exchange matrix $\boldsymbol{J}_{j,k}$, as introduced earlier, couples these different components. Depending on the nature of the interaction and on the orbital electronic physics, several simplified typologies of interactions between two spins in a quantum magnetic system can be found: as extremal cases, in Ising-like systems only one spin component couples (conventionally, z) [8], in the XY systems two components couple (conventionally x and y), and in Heisenberg systems all components are coupled [9]. This usually is visualized by interpreting Ising spins as lying along a quantization axis, xy spins as lying on a quantization plane, and Heisenberg spins as being unconstrained.

All of the interactions listed so far have the common feature that (within one coordinate transformation) the matrix $\boldsymbol{J}_{j,k}$ is diagonal, and the difference between these typologies of interaction becomes related to the number of non-zero eigenvalues (one in Ising systems, two in XY, three in Heisenberg) and ideal XY and Heisenberg also require that all the eigenvalues be the same. A notable example of an off-diagonal interaction is the Dzyaloshinsky-Moryia interaction [10, 11], $\vec{D}_{j,k}\cdot(\hat{S}_j\times\hat{S}_k)$, which is equivalent to a traceless matrix with no real, non-zero eigenvalue.

The origin of Ising-like behaviour Ising-like interactions require spins to point along one axis, which can happen due to large anisotropy [12]. One

notable ion that is characterised by Ising-like physics is Dy^{3+} [13], such as for instance in $DyBa_2Cu_3O_{7-\delta}$, whose magnetic behaviour is that of Ising spins arranged on a square 2D lattice [14], or in DySb [15, 16].

In Co^{2+}, another Ising-like ion, the ground state for electrons is ^{4}F, which splits under an octahedral ligand field so that the ground state becomes the $^4T_{1g}$ state. However the angular orbital momentum is not quenched and thus spin-orbit couplings lead to additional splittings into Kramers doublets, hence the effective spin is 1/2. The Jahn-Teller distortion can then act on the Kramers doublets and, depending on the kind (i.e. whether it stretches or compresses) can drive the spin towards an Ising-like or an XY behaviour. This ion, therefore, is very well suited to build non-Heisenberg spin systems.

1.3.3 Geometrical frustration

No matter the dimensionality, the geometry can provide a network of competing interactions so that the pair-wise interactions cannot be all simultaneously minimised: this can influence the order and even suppress T_C to zero Kelvin, resulting in no specific, ordered ground state [17, 18, 19, 20, 21, 22]. A typical example is that of antiferromagnetically interacting spins on a triangular lattice, as sketched in Fig. 1.1: no configuration of three spins on the three vertexes of the triangle can simultaneously minimize all pair-interactions. Although antiferromagnetic triangular, hexagonal, or Kagomé lattices are prime candidates, frustration can also be exhibited by more complex structures, such as spinels [18, 23] or in pyrochlores [24], where it can lead to the spin ice behaviour [25].

1.3.4 Quantum phase transition

A quantum phase transition (QPT) is a transition that is driven by a control parameter other than temperature, and as such can happen even in the limit of 0 K [26, 27, 28, 29, 30, 31], see Fig. 1.2 for two examples. Possible tuning parameters are, for instance, pressure or the chemical potential. In the limit of $T = 0$ K, the transition from a phase to another cannot be due to thermal

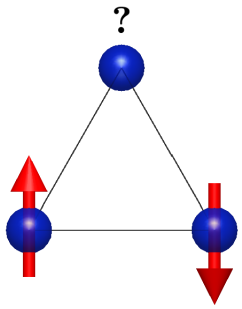

Figure 1.1: Example of a simple frustrated geometry: three antiferromagnetically-interacting Ising spins on a triangular lattice. If any two ions align up and down, the third is equally likely to align up or down.

fluctuations: it must thus be due to quantum fluctuations, which originate from Heisenberg's uncertainty principle.

One specific example of a phase transition is the application of a perpendicular magnetic field in Ising-like systems. As discussed in the previous section, Ising-like systems order with their spins all pointing along one physical direction (by definition z): however at a critical value of the magnetic field H_C spins will minimize their energy by pointing along the magnetic field and not along z, creating a forced collinear ferromagnet. Such a phase transition would happen continuously, which means that if the excitation were gapped at $H = 0$, increasing the field would diminish the gap energy until "closing the gap" at $H = H_C$.

1.4 Compounds studied in the thesis

In this thesis, the three compounds offer three unique combinations of aspects of dimensionality and interaction, from 1D to 3D, and from Ising to Heisenberg, with various degrees of frustration, which highlights how the properties of a system depend on such fundamental factors.

The compound $RbCoCl_3$ (see Chapter 3), is a material dominated by one-dimensional Ising-like chains. Perpendicular to the chains, the spins lie on a hexagonal grid and have ferromagnetic interactions, leading to frustra-

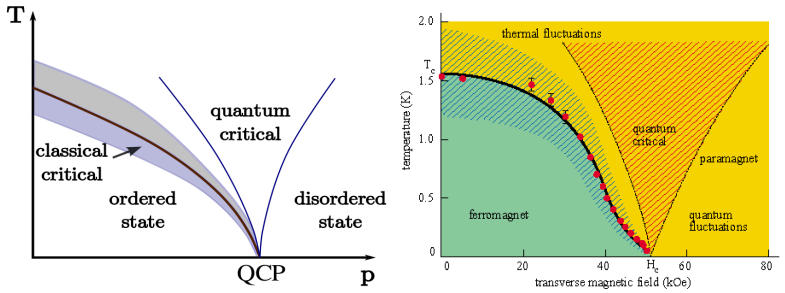

(a) (b)

Figure 1.2: (a) Simplified example of a QPT: both temperature T and the control parameter p can induce a phase transition from an ordered state to a disordered state. Figure reproduced from [32]. (b) Phase diagram of $LiHoF_4$, experimentally determined by Bitko *et al* by measuring the magnetic susceptibility [26]. This material is an Ising ferromagnet which becomes a paramagnet when a magnetic field is applied perpendicular to the Ising direction. The thermal paramagnet and the *quantum paramagnet* phases are connected continuously through the quantum critical region, where thermal and quantum fluctuations are "equally important" to determine the properties of the sample. The phase transition deviates from mean-field theory (an effect visible between 40 kOe and H_C) due to the nuclear hyperfine interaction. Figure reproduced from [33].

tion. Since this compound is Ising-like, it is supposed to display a QPT at a certain magnetic field H_C.

The compound $Lu_2V_2O_2$ (see Chapter 4) crystallizes in a pyrochlore lattice. While for Ising-like exchanges this compound can exhibit frustration due to its structure being comprised of vertex-sharing tetrahedra, spins in $Lu_2V_2O_7$ obey a Heisenberg Hamiltonian and order into a collinear ferromagnet despite the presente of the antisymmetric Dzyaloshinskii-Moriya interaction. This system exhibits the magnon Hall effect, which will be described later.

In the final compound $SrCu_2(BO_3)_2$ (see Chapter 5) the magnetic ions align in square planes that are characterised by strong in-plane and weak out-of-plane interactions, leading to marked two-dimensionality of the magnetic system. Moreover the spins form antiferromagnetic couples (i.e. dimers) and their (Heisenberg) interactions with the spins in other dimers is frustrated. In this system, the dispersion is not dominated by the direct exchange but by the Dzyaloshinskii-Moriya interaction.

In order to investigate the magnetic properties of these compounds we have employed the techinque of neutron scattering, which will be described in the next chapter.

Chapter 2

Introduction to Neutron Scattering

2.1 Theory and Background

2.1.1 Theory of Neutron Scattering

Fundamentals of Neutron Scattering

Neutron scattering is a versatile non-invasive investigation technique that measures density correlations. It is closely related to the complementary technique of X-ray scattering. There are several good graduate-level books developing its theoretical background, such as *Introduction to the Theory of Thermal Neutron Scattering* by Gordon Leslie Squires [34] or *Theory of Neutron Scattering from Condensed Matter* by Stephen W. Lovesey [35], as well as good lecture notes on the subject. I will proceed with a brief introduction on the theoretical fundamentals.

In general, a flux of neutrons is directed at a sample and the number of scattered neutrons per second and per flux unit - i.e. the double derivative of the total neutron density σ - is measured as a function of the scattered neutron energy $dE_{\vec{k'}}$ and solid angle element $d\Omega$:

$$\frac{d^2\sigma}{d\Omega dE_{\vec{k'}}} \propto \frac{number\ of\ scattered\ neutrons\ per\ second}{d\Omega dE_{\vec{k'}}}. \tag{2.1}$$

where $\vec{k'}$ is the wave vector of the outcoming neutron.

This cross section requires all informations about the system and the

interaction between the system and the neutrons, which can be calculated using Fermi's Golden Rule – expressing the probability $p_{i\to f}$ of the system to transition from the initial state i to the final state f through the effect of the perturbating (interacting) Hamiltonian V as:

$$p_{i\to f} = \frac{2\pi}{\hbar} |\langle f|V|i\rangle|^2 \rho_f \tag{2.2}$$

where $|i, f\rangle$ are eigenfunctions of some Hamiltonian $\mathcal{H}$ (which doesn't commute with the perturbation V) and ρ_f is the density of states function evaluated for the final state. In this case, we assume that neutrons trigger a transition in the sample from an initial state λ of probability p_λ to a state λ' via the interaction potential $V(r)$; the neutrons are scattered from a state $(E_{\vec{k}}, \vec{k})$ to a state $(E_{\vec{k'}}, \vec{k'})$. The conservation of energy is included via the delta function $\delta(E_\lambda - E_{\lambda'} + E_{\vec{k}} - E_{\vec{k'}})$, which allows the energy of the sample to be increased/decreased only by the neutron energy loss/gain.

$$\frac{d^2\sigma}{d\Omega dE_{\vec{k'}}} = \frac{k'}{k}\left(\frac{m}{2\pi\hbar^2}\right)^2 \sum_\lambda p_\lambda \sum_{\lambda'} |\langle \vec{k'}\lambda'|V|\vec{k}\lambda\rangle|^2 \, \delta(E_\lambda - E_{\lambda'} + E_{\vec{k}} - E_{\vec{k'}}). \tag{2.3}$$

This is usually written as

$$\frac{d^2\sigma}{d\Omega dE_{\vec{k'}}} = \frac{k'}{k}\frac{\sigma_{tot}}{4\pi} N S(\vec{Q}, \omega) \tag{2.4}$$

where $S(\vec{Q}, \omega)$ is called the *scattering law*, $\vec{Q} = \vec{k} - \vec{k'}$ is the *scattering vector*, see Fig. 2.1, N is the number of atoms in the sample and σ_{tot} is the total scattering, a material-dependent intensity factor.

In the case of nuclear non-magnetic scattering, $S(\vec{Q}, \omega)$ obeys the following relations to the *intermediate function* $I(\vec{Q}, t)$:

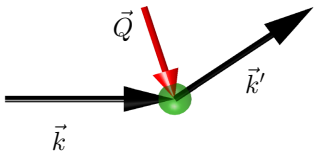

Figure 2.1: Scattering triangle. Neutrons have an initial momentum $\vec{k}$ and a final momentum $\vec{k}'$ (black arrows) after scattering on the sample (green sphere). The momentum transfer is $\vec{Q} = \vec{k} - \vec{k}'$ (red arrow).

$$I(\vec{Q},t) = \frac{1}{N}||\tilde{b}(-\vec{Q},0)\tilde{b}(\vec{Q},t)|| \tag{2.5}$$
$$S(\vec{Q},\omega) = \frac{1}{2\pi\hbar}\int I(\vec{Q},t)e^{-i\omega t}dt,$$

where $\tilde{b}$ is the the Fourier transform of the collection of atomic neutron scattering lengths $\tilde{b}(\vec{Q},t) = \sum_j b_j e^{-i\vec{Q}\cdot\vec{R}_j(t)}$, j being an indexing of the atoms in the system. Here $||...||$ denotes the expectation value. The scattering radius b_j is the same parameter that describes Compton scattering.

We can therefore say that neutron scattering probes the Fourier transform (both in space and in time) of the correlation function between all components of a material.

Furthermore it can be separated between *elastic* and *inelastic* scattering depending on whether energy is exchanged between the sample and the incident neutron. In the case of an ordered lattice, elastic scattering reduces to the expression:

$$\left(\frac{d^2\sigma}{d\Omega dE_{\vec{k}'}}\right)_{el} \propto |F(\vec{Q})|^2 \sum_{\vec{\tau}} \delta(\vec{Q}-\vec{\tau})\,\delta(\omega) \tag{2.6}$$

where $\vec{\tau}$ are all reciprocal lattice vectors and $F(\vec{Q}) = \sum_n b_n W_n(\vec{Q})\, e^{-i\vec{Q}\cdot\vec{d}_n}$,

with n counting all atoms contained in a unit cell, is called the *structure factor*. Here $W_n(\vec{Q}) = \exp(-\alpha T Q^2/2)$ is the Debye-Waller factor, which takes into account the small deviations of ions from their lattice site due to the temperature T (α is a material-dependent constant in this approximation).

This formula can be shown to be related to Bragg scattering: elastic scattering from a crystal will only be observed when $\vec{Q} = \vec{\tau}$, i.e. when the momentum transfer matches a reciprocal lattice vector. Since $\vec{Q} = \vec{k} - \vec{k'}$ and $|\vec{k}| = |\vec{k'}|$ (elastic condition), then $Q := |\vec{Q}| = 2|\vec{k}|\sin\theta = 4\pi/\lambda \sin\theta = |\vec{\tau}| = 2\pi/d$, i.e. $\lambda = 2d\sin\theta$, the condition of the first Bragg reflection. Therefore elastic neutron scattering, i.e. *neutron diffraction*, is commonly used to determine the structure of crystalline materials.

Inelastic scattering, on the other hand, does not preserve the energy of the incident neutron. Due to the conservation of energy and momentum, this requires a quasi-particle to have been excited in the material, carrying a momentum and an energy that can be deduced from the change in speed and direction of the neutron.

Magnetic Neutron Scattering

Neutrons have a magnetic moment and are able to couple to spin density distributions – both elastically and inelastically. This enables a direct probe of magnetic structures and excitations.

The introduction of the spin formalism allows to write a scattering law analogous to Equation 2.4:

$$\left(\frac{d^2\sigma}{d\Omega dE_{\vec{k'}}}\right)_{mag} = \frac{N}{2\pi\hbar}\frac{k'}{k}(\gamma r_0)^2 \sum_{\alpha\beta dd'} (\delta_{\alpha\beta} - \kappa_\alpha\kappa_\beta)\left(\frac{1}{2}g_d F_d(\vec{Q})\right)\left(\frac{1}{2}g_{d'}F_{d'}(\vec{Q})\right) e^{-W_d(\vec{Q})-W_{d'}(\vec{Q})} S^{\alpha\beta}_{dd'}(\vec{Q},\omega) \tag{2.7}$$

where d is an index that runs over all magnetic atoms in the unit cell, α and β are x, y and z, γ is the gyromagnetic ratio and r_0 the classical electron radius; $\kappa = \vec{Q}/|\vec{Q}|$ is the direction of $\vec{Q}$, $W_d(\vec{Q})$ is the Debye-Waller factor,

$F_d(\vec{Q})$ is the *magnetic structure factor*, i.e. the time-independent Fourier transform of the magnetization distributions of each atom in the unit cell. The magnetic scattering law $S^{\alpha\beta}_{dd'}(\vec{Q},\omega)$ is a new measure of the correlation of the system that differs from Eq. 2.5 by considering operators of the magnetic density instead of structural densities.

In analogy to nuclear scattering, magnetic scattering probes the correlation in magnetization density in reciprocal space but, in contrast to nuclear scattering, the term $(\delta_{\alpha\beta} - \kappa_\alpha\kappa_\beta)$ selects the *transverse* component of the magnetization. To show this, it is useful to look at the limit case that all correlation is along z – i.e. $S^{\alpha\beta}_{dd'} = 0$ for α, β other than z: if $\vec{Q}$ is along z as well there will be no magnetic scattering, while if $\vec{Q}$ is along x or y the observed signal will be maximal. This term is called the *polarization factor*, and neutron scattering is unable to probe magnetic moments parallel to the transferred momentum $\vec{Q}$.

It has also to be noted that in nuclear scattering neutrons interact with nuclei, which can be considered to be point-like objects with respect to the wavelength of neutrons; the contribution of the probed object to the form factor is the Fourier transform of a delta function – i.e. a constant. In magnetic scattering neutrons interact with magnetic distributions that are not point-like; if they are assumed to be similar to Gaussian functions centred on the atoms then their Fourier transform also has the shape of a Gaussian centred at $\vec{Q} = 0$. This has the effect that magnetic neutron scattering will suffer a significant decrease of intensity as $|\vec{Q}|$ increases.

Instrumental resolution

While the technical part of a neutron scattering experiment has not been discussed yet, one important side of it is the *instrumental resolution*, which affects the signal as a convolution of the scattering law and the instrumental resolution function $R(\vec{Q},\omega)$, which in most cases is an ellipsoidal pseudo-Voigt function:

$$S(\vec{Q},\omega)_{exp} = S(\vec{Q},\omega) \otimes R(\vec{Q},\omega) \tag{2.8}$$

where $\otimes$ is a convolution.

This effectively means that, while the mathematical expressions contain delta functions, an experimental result will always have a certain, instrument-dependent intrinsic width.

Important instrumental factors that affect the resolution are, for instance, the size of the detector and of the sample, the divergence of the neutron beam (which is produced by focusing), or the distance between the neutron source, the sample and the detector. Most of these properties also affect the neutron flux – for instance, focusing the neutrons on the sample will increase the flux but introduce an uncertainty on the incoming wavevector, worsening the resolution. This relation between the resolution and the flux leads to a tradeoff between the accuracy of the data and the time required to acquire them.

2.1.2 Experimental techniques

The purpose of this section is to give a short summary of the instruments used in neutron scattering. A brief sketch of the triple-axis and ToF instruments employed during this thesis will be included.

Producing and guiding neutrons

The first way to produce a beam of neutrons is to use the excess neutrons from a stable uranium fission core. This generally produces a bright and continuous flux of neutrons. A notable such source is at the Institut Laue-Langevin (ILL) in Grenoble, France.

The second way requires directing a beam of protons (sped up in an accelerator) towards a metallic target (e.g. tungsten). In the subsequent *spallation* process, some atoms of the target have a chance of absorbing an

incoming proton and then releasing a series of light particles (e.g. alpha particles and neutrons). Some of the experiments in this thesis have been performed at the Paul Scherrer Institute (PSI) in Villigen, Switzerland, a continuous spallation source, and others at the ISIS facility in Didcot, United Kingdom, which uses a pulsed spallation source.

Once the neutrons leave the fission or spallation core, their kinetic energy is excessive for a neutron experiment. They are therefore *moderated* and thermalized, usually by passing through water (which is a powerful scatterer due to the presence of hydrogen, and thus a good moderator). For reference, a neutron which thermalises in room-temperature water will have a kinetic energy of roughly 30 meV. Standard terminology separates neutrons into *cold* (below 5 meV), *thermal* (between 5 and 100 meV), *epithermal* (between 100 meV and 1 eV) and above.

Neutrons exit the moderator and propagate to the measurement instrument. Lacking an electrical moment, neutrons cannot be deviated or accelerated by electrical fields, which is a challenge when trying to manipulate their path. Being waves, they are subject to the phenomenon of *total reflection*, which allows to create supermirrors that reflect the beam: this can be used to bend its path over long distances, or provide some degree of focusing to maximize the flux on the sample.

Selecting the incoming energy and detecting the outcoming neutrons

All but a handful of techniques (such as Laue or ToF diffraction) require neutrons with a precise energy or wavelength (i.e. a monochromatic beam) to reach the sample position.

In general this is achieved by discarding all neutrons of other incoming energies, which can be achieved by:

- employing a monochromator, i.e. a single crystal in the beam that diverts neutrons with a specific wavelength according to Bragg's law: controlling the angle at which the beam is incident on the monochro-

mator allows us to change the energy of the neutrons that are deflected out of the beam (i.e. deflected towards the sample).

- employing a chopper system, i.e. a set of rotating parts that allow neutrons to pass through only at a certain time (e.g. a rotating disc with a window in it). By absorbing all the neutrons that do not pass at the right time through all the openings, only neutrons with the desired speed reach the sample position.

After the sample position, neutron detectors are installed to count the signal in a specific region of the outcoming solid angle. Detectors are based generally on the absorption of neutrons and measure the electrical impulses that follow the relaxation of the excited nuclei. Historically the most relevant absorber in detectors is $^3_2$He.

As neutron spectroscopy investigates the energy transfer, it is necessary to measure the kinetic energy of the outcoming neutrons. Again, there are fundamentally two ways (although other possibilities, such as spin-echo techniques, are available and will not be discussed here).

- An analyser crystal is placed between the sample and the detector: relying again on Bragg diffraction and working like a monochromator, the analyser deflects into the detector only the neutrons with the energy and wavelength that satisfy the Bragg condition. Rotating the analyser allows to scan over a range of outcoming energies.

- If the time at which the neutron hits the sample is known (which is typically the case with pulsed sources or with chopper systems) then measuring the time at which the neutron hits the detector allows to calculate the speed of the outcoming neutron, and thus its kinetic energy. This technique, called *time-of-flight* (ToF), measures over a continuous range of outcoming energies for each pulse.

Triple-axis spectroscopy

A common instrumental setup for INS is the class of triple-axis spectrometers (TAS), which relies on a monochromator and an analyser to determine the energy transfer. Refer to Fig. 2.2 for an example.

While their magnitude is controlled by the energy, the wave vectors $\vec{k}$ and $\vec{k'}$ are controlled via the instrument geometry: $\vec{k}$ points along the axis between the monochromator and the sample, and $\vec{k'}$ along the axis that unites the sample and the analyser. These are controlled by physically moving the parts of the instrument.

In order to match $\vec{Q}$ to a desired reciprocal lattice vector the sample can be rotated. Commonly the sample is attached to a vertical sample stick, which allows a horizontal rotation of 360; however there are ways of achieving any rotation in the solid angle if one uses, for instance, a Euler cradle.

The advantage of this technique is the potential control over many experimental parameters; the instruments tend to be modular, allowing the setup to be changed to best suit the experiment – such as in the case of polarized analysis. These experiments, however, generally allow only one single combination of E and $\vec{Q}$ to be probed at one time, so that measuring the intensity of the scattering over a large volume of $\vec{Q}$-space will require a proportional number of scans.

During my PhD I have had the chance to take part in experiments performed at the TAS instruments IN20 and IN22 (ILL), EIGER and TASP (SINQ).

ToF spectroscopy

In ToF instruments, the time of flight of the neutron is used to calculate their velocity and hence their energy. This technique relies on a pulsed monochromatic incoming neutron beam and time-sensitive detectors. While the same geometric argument is valid for $\vec{Q}$, the speed of the outgoing neutron determines the energy transfer to the sample and, as the intensity of neutrons

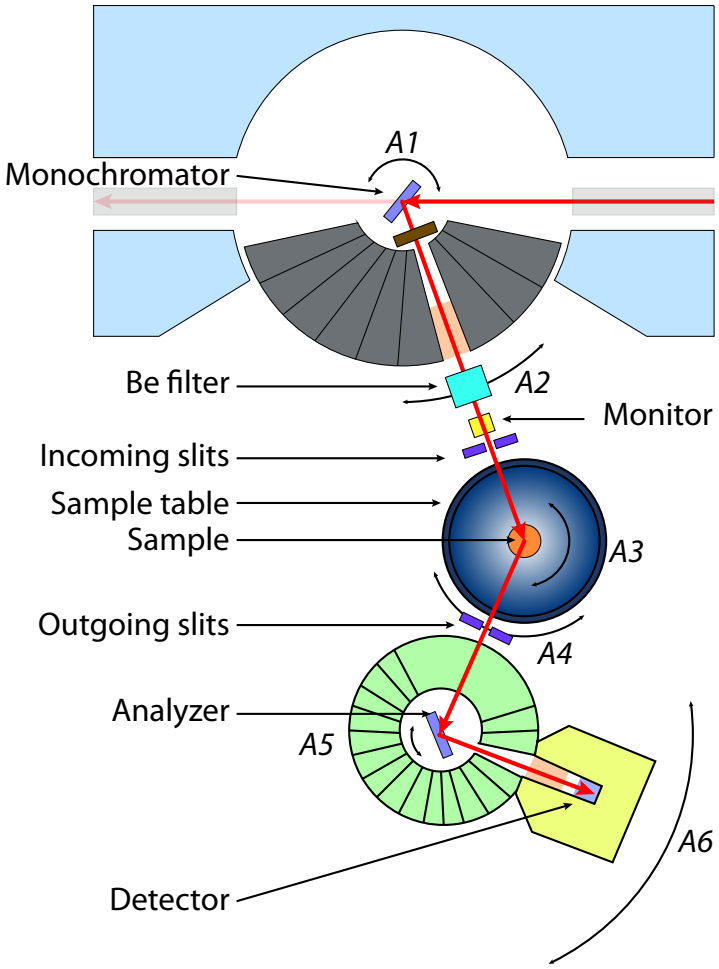

Figure 2.2: Schematic view of a typical triple-axis instrument (IN14 at ILL). A flux of neutrons (red) travels inside a neutron guide (light gray). At the monochromator, part of the beam is directed towards the sample (orange) via Bragg diffraction. The sample table (deep blue) is in general a modular space where the required equipment can be deployed (e.g. cryostat, magnet, pressure cell). After the scattering event, the outcoming energy is selected by the analyser (light green), and the neutrons that have undergone Bragg diffraction are counted in the detector (yellow). A1 to A6 are the angles that can be controlled to select the correct incoming and outcoming energy, as well as the projection of $\vec{Q}$ on the reciprocal space of the sample. Further components, such as the monitor, the incoming slits, the outgoing slits, a ^{3}He polarization filter (not shown) allow further control over the instrumental conditions. Image reproduced from Ref. [36].

can be recorded as a function of time, one single detector measures the intensity as a function of transfer energies for the same value of $\vec{k'}/|\vec{k'}|$. There is therefore no need for an analyser based on Bragg diffraction. See Fig. 2.3 for an example.

ToF spectrometry has seen substantial development in the last decades in the direction of pixelated wide-angle detectors in order to maximize the measured volume of $\vec{Q}$-space. This is made advantageous by the fact that no analyser is required between the sample and the detector, simplifying the design, and these detectors can today have a total angular coverage of ∼180 degrees horizontally and ∼60 degrees vertically. As the signal is a function of two physical coordinates and one time component, such a detector maps a three-dimensional curved submanifold in $(\vec{Q}, \omega)$-space.

A clear advantage of this technique is the huge area that can be simultaneously measured and the possibility to theoretically map the entire $(\vec{Q}, \omega)$-space within the kinematic limits.

During this thesis experiments have been performed at the ToF spectrometers MERLIN, OSIRIS and LET (ISIS).

Data treatment and visualization

On instruments such as Merlin or LET, the data is collected by single detector units, which work like pixels. The dataset originally thus has two space coordinates (the pixel ID, which tells the horizontal and vertical position) and one time coordinate (i.e. the time elapsed between the pulse of the source and the time of impact of the neutron in the detector). This information is converted to energy and momentum transfer and is normalized for detector efficiency, integrated neutron flux and sometimes mass of the sample.

The pixels lie on a three-dimensional submanifold of $(\vec{Q},\omega)$. A technique that compensates for the lack of data in the rest of $(\vec{Q},\omega)$-space is the so-called *Horace scan*, in which the sample itself is rotated in order to provide a third space coordinate.

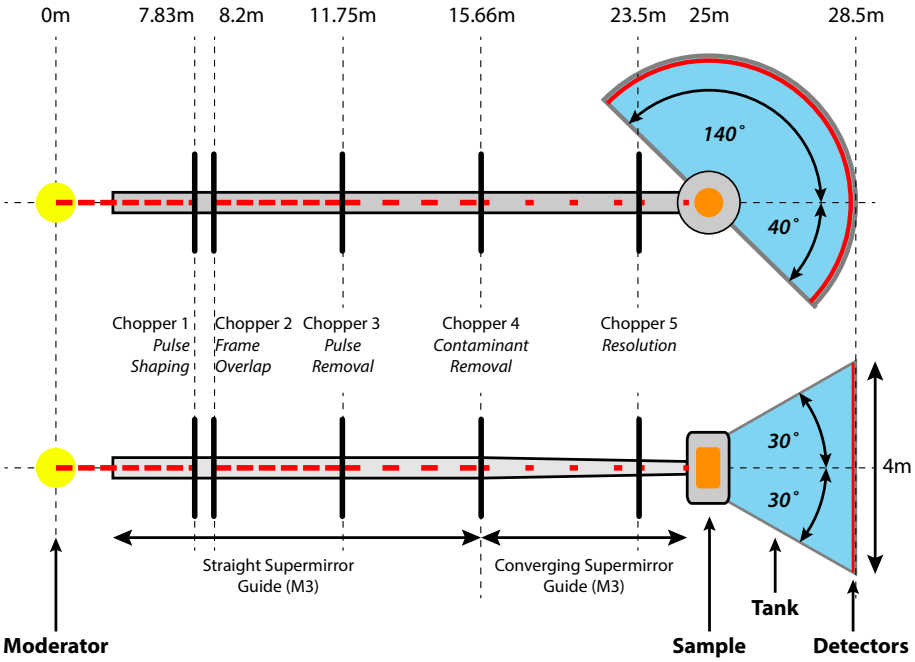

Figure 2.3: Schematic view of the time-of-flight spectrometer LET (ISIS) from the top (top) and from the side (bottom). A flux of neutrons (red) travels inside a focusing neutron guide (light gray) from the pulsed moderated source (yellow) to the sample (orange). A series of choppers (black) allow only the neutrons with the correct incoming energy to reach the sample (note: several ToF instruments have a much simpler chopper system). After the sample, the neutrons travel through an evacuated tank (light blue) and are collected in the detectors (red), a series of 4 m tall ^{3}He tubes arranged on a half-cylinder around the sample. The time of absorption of the neutron is measured and allows determining of the energy transfer. Image reproduced from Ref. [36].

In order to be displayed, the data is usually binned: all pixels are sorted into bins according to an arbitrary grid and then averaged within the bin, so that the density of pixels in different bins, which is not constant, does not increase the overall intensity in the bin. Furthermore, the data is presented in *cuts*, which are one-dimensional, and *slices*, which are two-dimensional. The visual data is therefore projected, binned, and averaged within the bin. The reduction from full four-dimensional data to a two-dimensional slice or a one-dimensional cut is to be done carefully and potentially introduces problems that must be taken into account: for instance, in one-dimensional systems, the dispersion does not vary with respect to two $\vec{Q}$ directions but the its intensity does (e.g. the magnetic form factor decreases the intensity of the as a function of $|\vec{Q}|^2$). Therefore it is e.g. possible to measure a certain part of the spectrum in a part of $\vec{Q}$-space where it has a significant structure factor, and another part of the spectrum in a volume where the structure facture is much lower: this creates a modulation of intensity that is equally explained by the scattering function and by the instrumental measurement. This will be the case for instance in $RbCoCl_3$, in the next chapter, where the signal in the $L-E$ slices is strong for L between -1.5 and -0.5 r.l.u. and much weaker outside of that. Slices of 3D systems can be even more complex, as they will "flatten" one spatial dimension, creating a picture that explicitly depends only on two coordinates (say, H and K) but where each pixel has a different L and E coordinate: this will be the case in $Lu_2V_2O_7$, where the spectrum should have a certain symmetry (say, spherical at some energies, or cubic at other energies) but the averaging deforms what should be perfect rings or squares, making them appear more ovoidal or rounded. All of these possible issues can be taken into account in the calculation if the full four-dimensional spectrum is simulated, and remain of importance only in understanding the visual representation of the data.

Chapter 3

The temperature-dependent soliton spectrum of the 1D chain compound $RbCoCl_3$

3.1 Scientific background

The interest in low-dimensional physics, especially concerning the magnetic properties, is the rich typology of phenomena and excitations that derive from a deceivingly simple – and often exactly solvable – Hamiltonian. A notable example of these, of particular relevance to the thesis, is the Ising system.

The recent technological developments in spectroscopy, particularly in neutron scattering, offer a chance and give a reason to revisit one-dimensional (1D) quantum magnetic systems and investigate in much greater depth their properties.

Amongst the most ideal 1D quantum magnetic systems are the realizations of the Ising-like Hamiltonian, of which the ABX_3 (A = Cs, Rb; B = Co, Cu; C = Cl, Br) compounds are notable examples. As this family has never before been investigated with a modern high-resolution instrument, we have performed a comprehensive series of experiments on $RbCoCl_3$, including neutron diffraction [37] and neutron spectroscopy.

As it will be discussed, $RbCoCl_3$ has two magnetic ordering phase transitions. This allows an experiment to tune and access distinct regimes of the thermal Ising chain – at the lowest temperature the sample displays a

perfectly ordered ferrimagnetic honeycomb pattern; between temperatures it is described as a partially disordered antiferromagnetic state; and above the phase transition the chains are isolated from other chains due to thermal fluctuations.

An additional reason of interest in the 1D systems is the presence of quantum phase transitions. A system such as $RbCoCl_3$ is a prime candidate to observe this phenomenon and part of our motivation in studying this compound was the hope that the gap could be closed; however it will be discussed how the magnetic field required exceeds the current technical capabilities.

The structure of this chapter is as follows: I will start by describing the cases of $CoNb_2O_6$ [38] and $BaCo_2V_2O_8$ [39], prototypical examples of 1D Ising-like physics and quantum phase transitions which have been the subject of numerous recent experiments.

I will then proceed to describe the experimental details of our inelastic neutron scattering experiment on $RbCoCl_3$ and to describe the data.

I will then summarize the relevant literature, with particular attention to the theory. I will argue for a unique interplay between the long-range 3D order and the 1D excitations of the system. Having established the terms of the Hamiltonian, I will then show the fits. I shall claim an excellent agreement between the data and the simulations to a set of exchange parameters.

The last section will be dedicated to a discussion of the long-range 3D order, including Monte Carlo simulations to interpret the fitted relative intensity parameters.

This work is part of a collaboration between N. Hänni (University of Bern, Switzerland), who has investigated the structural phase transitions [40, 37], Dr. E. Hirtenlechner (ETH Zürich, Switzerland), who has investigated the effects of temperature in greater detail [41], and myself. I was the main investigator in the experiment at LET, and I took part in the magnetic susceptibility and elastic neutron scattering measurements performed by N. Hänni. I performed the analysis, writing and improving the formulas

for the cross section and the Hamiltonian, and subsequently implemented a Monte-Carlo algorithm to relate structural and dynamic properties of this compound. A number of papers on this compound are in preparation.

3.2 Examples of Ising-like 1D physics

3.2.1 $CoNb_2O_6$

$CoNb_2O_6$ is an insulating quasi-1D ferromagnet where the magnetic Co^{2+} ions form zigzag chains of spins whose interaction is close to the Ising model [38, 42, 43]. This compound orders ferromagnetically at $T_N = 2.95$ K and, due to its Ising-like nature, its excitations are couples of moving domain walls. The weak intra-chain interactions, which lead to 3D order, induce a uniform staggered field on all sites.

When applying a field transverse to the direction of the spins, e.g. along $\vec{b}$, it is possible to drive the system through a quantum phase transition at $B_C = 5.5$ T, to a transverse ordered state whose elementary excitations are spin-flip quasiparticles [38].

A picture of the zero-field excitations of $CoNb_2O_6$ is reproduced in Fig. 3.1. Above the critical temperature the spectrum is comprised of a broad two-domain continuum and a kinetic bound mode, while below the critical temperature the continuum splits into confined bound states. These bound states can be understood in terms of a Zeeman ladder induced by the weak intra-chain interactions.

Its excitations under a quasi-critical field obey a description that can be linked with the E_8 Lie symmetry. This behaviour may be found in other, if not all, Ising chains, but is so far only found in this compound.

3.2.2 $BaCo_2V_2O_8$

The magnetism in the tetragonal $BaCo_2V_2O_8$ is characterised by screw chains of Co^{2+} ions along the c axis, with the magnetic ordering emerging at $T_N \approx 5.5$ K. A fit of the spectrum, shown in Fig. 3.2, reveals that

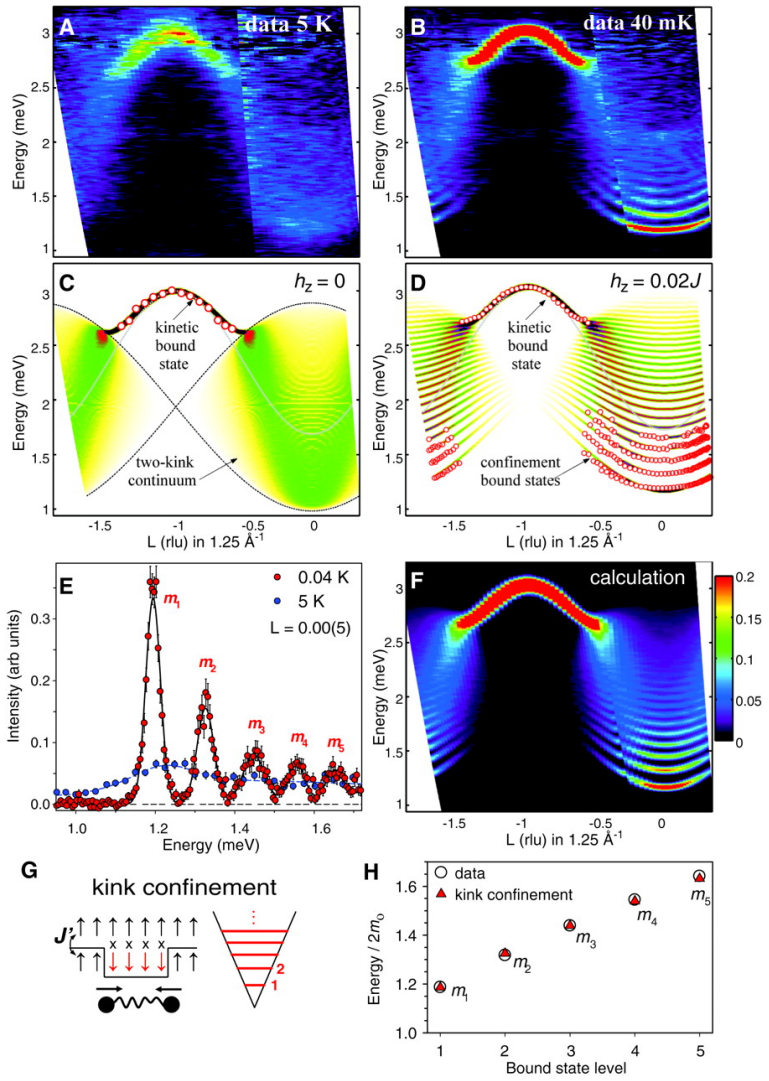

Figure 3.1: Zero-field excitations in the Ising-like 1D ferromagnet $CoNb_2O_6$, figure courtesy of [38]. Above the ordering temperature $T_N = 2.95$ K the spectrum consists of a two-kink (spin-flip) continuum and a kinetic bound state (panels A, C), while below T_N the two-kink continuum splits into confined bound states (panels B, D). This behaviour was discussed in terms of a "kink confinement" model.

the main interaction J is 5.6 meV and the Ising-like anisotropy ϵ is 0.46.

The excitations of this system display discrete bound modes within a bow-tie-like area, see Fig. 3.2. The energies of the bound modes can be explained using the zeros of the Airy function.

The magnitude of ϵ places this compound almost exactly half-way between prototypical Ising and prototypical Heisenberg models. In a domain-wall system, we can define *transverse* (*longitudinal*) modes as characterised by an odd (even) number of spins being flipped. The intensity of longitudinal modes typically scales with ϵ^2 [44], so that they can be observed only for large ϵ. Owing to its ϵ =0.46, the longitudinal modes are however measured in $BaCo_2V_2O_6$, and can be distinguished experimentally by their dependence on the polarization factor.

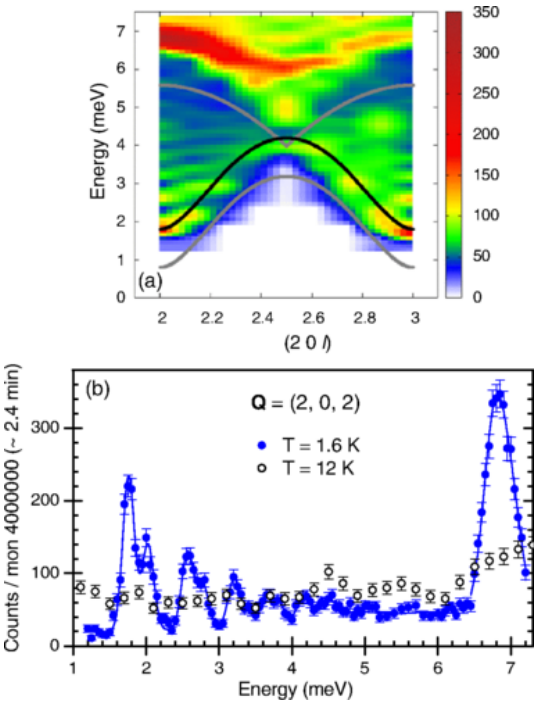

Figure 3.2: Magnetic excitations in $BaCo_2V_2O_8$, figure courtesy of [39]. Longitudinal and transverse modes form discrete bound modes in a bow-tie shaped area (between the gray curves).

3.3 The magnetic properties of $RbCoCl_3$

$RbCoCl_3$ is a hexagonal perovskite that crystallises in the $P6_3/mmc$ space group ($a = b = 7.0003$ and $c = 5.9989$ Å). In this crystal structure, which is sketched in Fig. 3.3, the Co^{2+} ions are contained into Cl^- antiprisms and form straight chains along the c axis. The distance between Co^{2+} ions is 3 Å along the c axis and 7 Å along $\vec{a}$ or $\vec{b}$, creating a strongly one-dimensional environment.

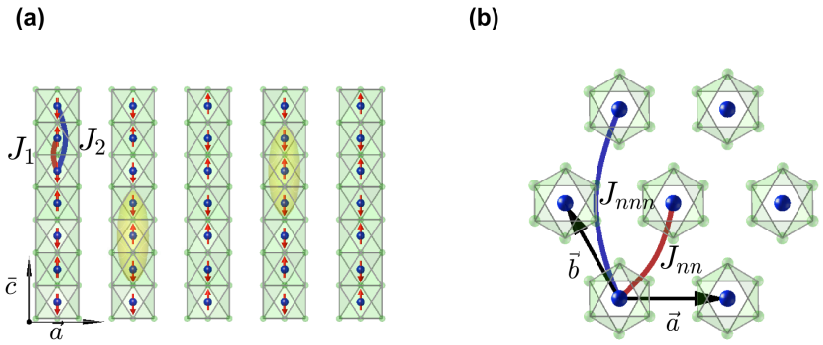

Figure 3.3: Structure of $RbCoCl_3$ and its interactions. (a)View of the a-c plane. The Co^{2+} ions (blue) are embedded into Cl^- antiprisms (light green) and their spins interact most strongly with spins along the c direction (with exchanges J_1, J_2) than with spins located along a or b: this results in the formation of spin chains along the c axis. The two yellow ovoids contain two solitons, at which ends are domain walls: the domain walls can be distinguished as they are comprised of two parallel spins, instead of being antiparallel. (b) View of the a-b hexagonal plane perpendicular to the chains, and of the two"in-plane" interactions J_{nn} and J_{nnn}.

As preliminary work to the INS part, it is useful and necessary to discuss briefly the magnetic properties of $RbCoCl_3$ as revealed by magnetic susceptibility and neutron diffraction experiments.

3.3.1 Magnetic susceptibility

The molar magnetic susceptibility of $RbCoCl_3$ was measured and the results are displayed in Fig. 3.4. The behaviour is consistent with the models for Ising chains, with a more structured response along the c axis, a kink at 12 K (the temperature, as discussed later, of a phase transition), and a broad maximum around 70 K, suggesting a coupling in the order of 70 K [40].

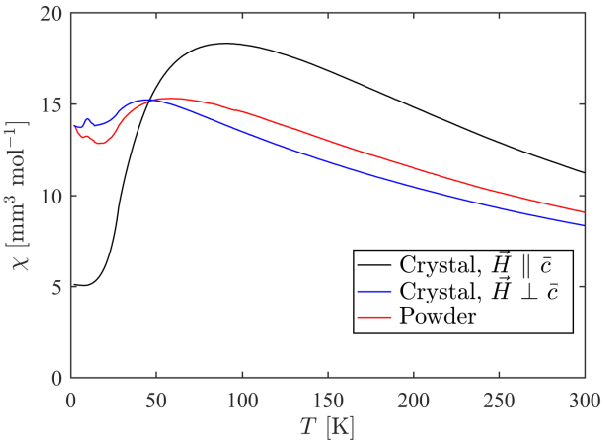

Figure 3.4: Molar dc magnetic susceptibility of both powder and crystalline $RbCoCl_3$ [40].

3.3.2 Diffraction and phase transitions

A series of neutron scattering experiments were performed, notably on HRPT, TRICS and EIGER (SINQ, PSI, Switzerland). A comprehensive summary of these results and their analysis can be found in [37, 40].

Neutron powder diffraction down to 1.5 K confirmed the $P6_3/mmc$ symmetry, preserving thus both the linearity of the chains and the hexagonality of the planes.

Furthermore, diffraction reveals two low-temperature magnetic phases, at $T_{N2} = 12$ K and $T_{N1} = 28$ K. Exemplary scans along the $(H\ H\ 1)$ direction, performed at the triple-axis neutron spectrometer EIGER (SINQ, PSI, Switzerland), are shown in Fig. 3.5 at three temperatures: below T_{N2},

between T_{N2} and T_{N1}, and above T_{N1}.

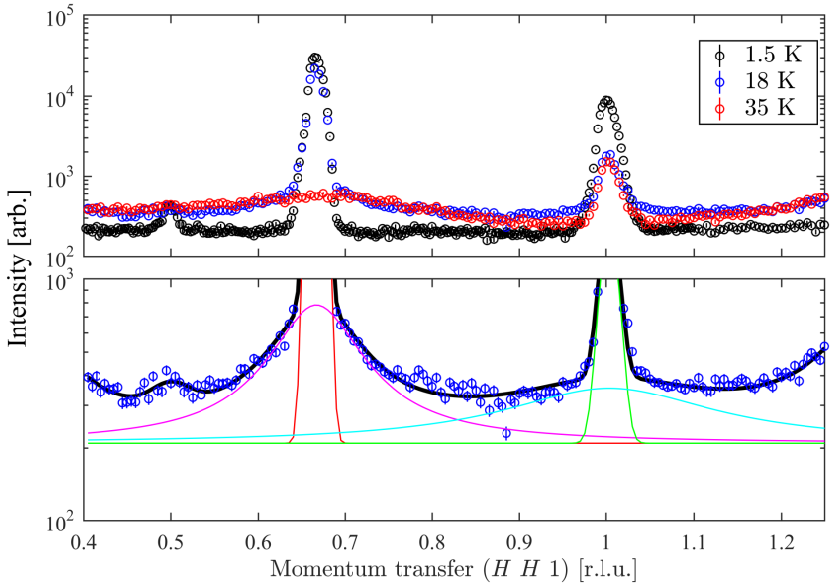

Figure 3.5: (a) Neutron diffraction scans performed at EIGER at $T = 1.5$ K, 18 K and 35 K. The peak at (2/3 2/3 1) is purely magnetic, vanishing above T_{N1}. The peak at (1 1 1) is present above T_{N1} despite being structurally forbidden, due to imperfections in the crystal. (b) Fits of the scan at 18 K. Each peak is the sum of two components: a sharp Gaussian peak (red, green) and a broad Lorentzian peak (magenta, cyan). Below 0.45 and above 1.2 the tails of the (1/3 1/3 1) and (4/3 4/3 1) Bragg peaks can be measured and have been included in the fit. An additional peak can be resolved at (1/2 1/2 1).

The intensities of the purely magnetic (2/3 2/3 1) and (1 1 1) peaks are plotted in Fig. 3.6. It can be seen how the (1 1 1) reflection disappears at 12 K (aside from a residual peak that is due to an imperfection of the sample), while the (2/3 2/3 1) undergoes two power-law-like drops at both phase transitions.

Each magnetic reflection is modelled as the sum of two components: a resolution-limited Gaussian peak of constant width, and a broader Lorentzian peak whose width varies with temperature, which is diffused

scattering due to short-range order. The integrated intensity of the two components changes in temperature, with all intensity in the Gaussian peak at the lowest temperature, and a transfer of the intensity to the Lorentzian component in the proximity of the phase transition.

Below T_{N2} both peaks are resolution-limited, signifying a perfect 3D honeycomb order throughout the sample. Between T_{N2} and T_{N1} the significant diffuse scattering is due to partial disorder and lack of long-range order (which later will be identified as a partially disordered antiferromagnetic state). Above T_{N1} the ordered moment vanishes quickly but not completely due to the permanence of short-range order, which is expected to be observed up to 70 K (as confirmed by the magnetic susceptibility).

The diffraction on $RbCoCl_3$ has outlined as well the presence of the (1/2 1/2 1) magnetic reflection below T_{N2}[1], which has been interpreted in terms of a second $\vec{k}$-vector. A full discussion on the magnetic ordered structure of this compound can be found in [40]. Due to the weakness of this peak, however, in the present work we consider it as the expression of an impurity phase.

3.4 Experimental work on $RbCoCl_3$

I measured and studied the spectrum of $RbCoCl_3$ as a function of temperature in order to establish its properties in the three phases.

An initial INS experiment was performed on the ToF spectrometer LET (ISIS, UK) in autumn 2011. Three single crystals, see Fig. 3.7, were grown using the Bridgman technique in a vertical moving furnace with a temperature gradient [40] and were coaligned with (HHL) in the horizontal scattering plane. The sample was sealed in a Helium can due to its sensitivity to air.

For the experiment, the sample was inserted in a conventional Orange cryostat (1.5 to 300 K) and orientated with $\vec{k}_i$ parallel to $(00L)$. Data were

[1] It has been confirmed not to be spurious, e.g. a so-called $\lambda/2$ (1 1 2) peak, and to be magnetic in nature.

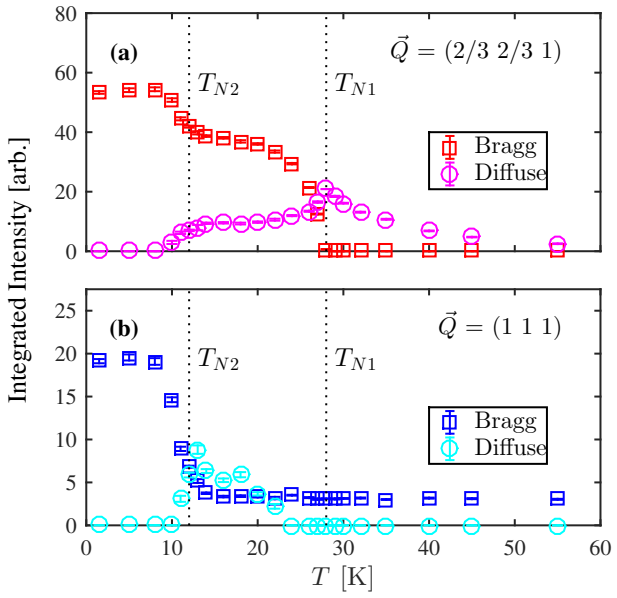

Figure 3.6: Integrated intensities of (a) the (2/3 2/3 1) peak and (b) the (1 1 1) peak as a function of temperature. Each peak is modelled as a resolution-limited Gaussian peak (i.e. Bragg scattering) and a broader Lorentzian peak (i.e. diffuse scattering), signifying a shift from perfect order to short-range correlation with temperature. The black vertical dotted lines mark the transition temperatures. Note that the intensity of the (1 1 1) peak does not vanish above T_{N1}, as the (2/3 2/3 1) peak does, due to an imperfection of the crystal.

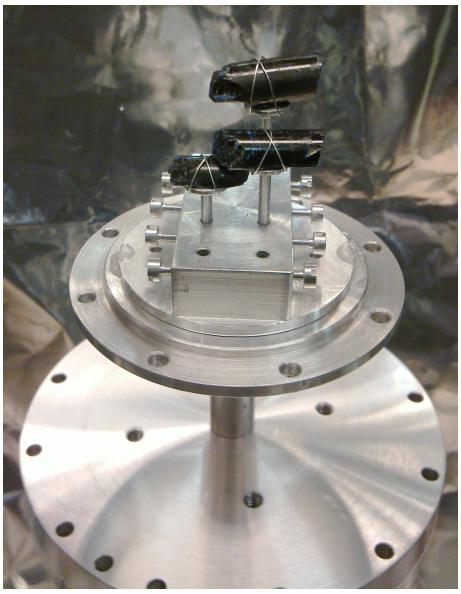

Figure 3.7: Photo of the coaligned $RbCoCl_3$ sample used in the LET experiment. The three single crystals (black) were secured to an aluminium mount, which was sealed inside a can.

collected at 4 K $< T_{N2}$, $T_{N2} <$ 18 K $< T_{N1}$ and $T_{N1} <$ 35 K, i.e. in the two ordered phases and just above the Néel temperature, with $E_i = 25$ meV (chopper frequency: 200 Hz, calculated resolution at the elastic line: 0.8 meV) and measuring times typically around 18 hours per temperature. Additional, measurements with lower counting statistics scans at 8.5, 10.5 and 23 K were performed using $E_i = 20$ meV (chopper frequency: 200 Hz, calculated resolution at the elastic line: 0.6 meV), a configuration that offers a higher neutron flux but samples a decreased section of $(\vec{Q}, \omega)$-space.

The data were normalized with respect to the proton integrated current which the ISIS target received and were corrected for detector efficiency and outcoming versus incoming wavevector ratio k_f/k_i using the program MANTID [45, 46]. The resulting $S(\vec{Q}, \omega)$ datasets were analysed with the HORACE [47] software package.

At the time of the experiment the pixelated detector of LET counted 40960 detector units (of typical size a square inch), of which 33397 were

retained in the final dataset. The time of flight was transformed into 242 energy bins, producing roughly 8 million individual pixels.

The first question to be addressed regards the one-dimensionality of the measured spectrum.

3.4.1 One-dimensionality of the spectrum

Figure 3.8 shows slices of the data at 4 K as a function of K and L, while Fig. 3.9 shows the energy of the four main modes and their fits. It is shown that the H and K dependence of the dispersion of the modes (over several periods) is smaller than 0.3 meV, which is the instrumental resolution at that energy transfer.

It is hence concluded that the system can be satisfyingly described as 1D within the goodness of the data. Therefore for the rest of the discussion all the data is projected to the $L-E$ plane and averaged in order to maximize the statistics.

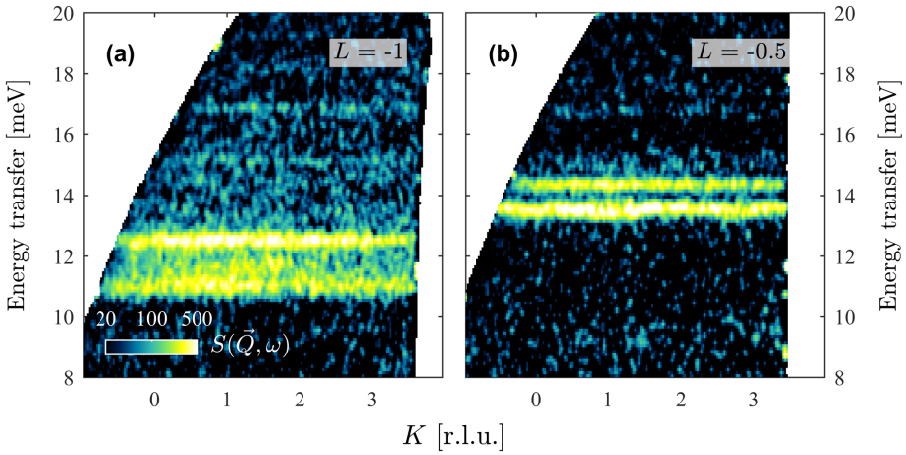

Figure 3.8: Two slices of the data, averaged for all values of H and for (a) -1.05 $< L <$ -0.95 and (b) -0.55 $< L <$ -0.45.

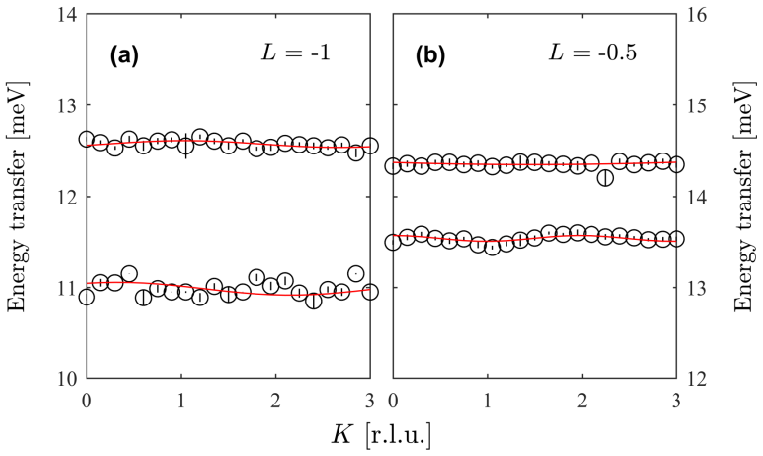

Figure 3.9: Fits of the energies of the modes from Fig. 3.8. All four modes, both for (a) -1.05 < L < -0.95 and (b) -0.55 < L < -0.45, are fitted to cosinusoidal curves whose fitted widths are smaller than the instrumental resolution.

3.4.2 Overview of the data

The data collected during the experiment is displayed in Fig. 3.10 for E_i = 25 meV and in Fig. 3.11 for E_i = 20 meV[2]. Cuts around L = -1 and L = -0.5 are presented in Fig. 3.12 for 4, 18 and 35 K, and in Fig. 3.13 for 8.5, 10.5 and 23 K.

A number of preliminary observations are summarized below:

- At 4 K and L = -1 the first feature is a peaked continuum with a maximum at its lowest edge (about 11 meV). A sharp mode at about 12.5 meV is also observed. The presence of two modes is an indication of the presence of two inequivalent magnetic sites, each with a characteristic spectrum, which will be discussed later.

- Still below T_{N2}, there are at least 3 modes between 11 and 13 meV at

[2]The data collected with E_i = 20 meV was multiplied with a normalization factor for its background to match the background with 25 meV, in order to compensate for the different flux and scaling. This is due to the normalization being in terms of the proton integrated flux and not the neutron monitor.

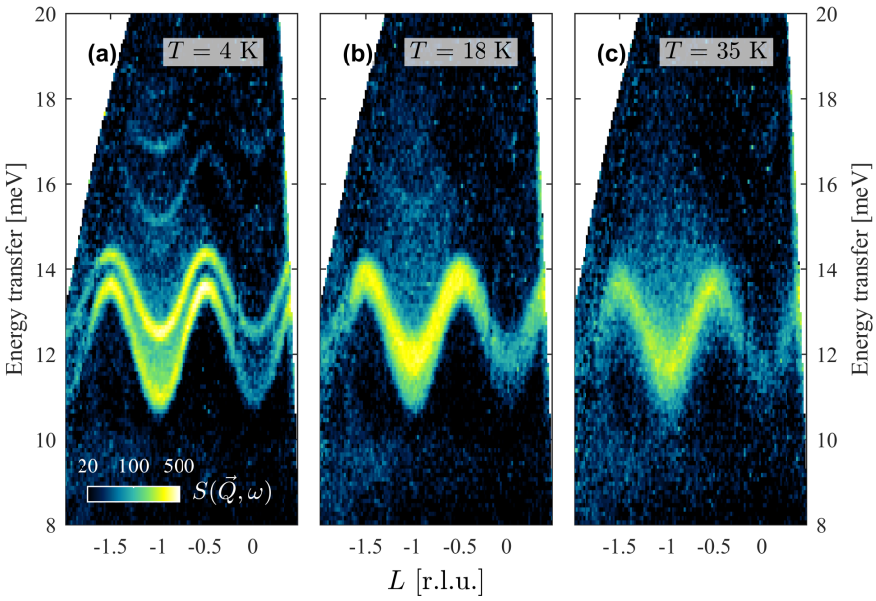

Figure 3.10: Slices of the experimental data at (a) 4, (b) 18 and (c) 35 K. The data is averaged with respect to H and K, and is displayed with a common logarithmic scale.

L = -1 at 8.5 and 10.5 K. Figure 3.14 compares a cut at 4 and 8.5 K to display the appearance of one such peak: the number of dispersive modes, and their relative intensity, changes with temperature.

- The temperature shifts the intensity to a central broad peak, as for instance at 18 K. At 35 K the peak's intensity decreases but its tails become more prominent.

The soliton is thus characterised as a function of temperature:

- Above T_{N1} a continuum is observed, most prominently between L = -1.5 and -0.5, with its intensity dominated by a cosine-like dispersive mode at its lowest edge. A similar continuum would be observed between -0.5 and 0.5 (due to its periodicity), but is not seen due to the overall decrease in intensity in this sector. This spectrum is, in first approach, bow-tie shaped and consistent with the idea of an Ishimura-Shiba solution for an isolated Ising chain, as will be discussed.

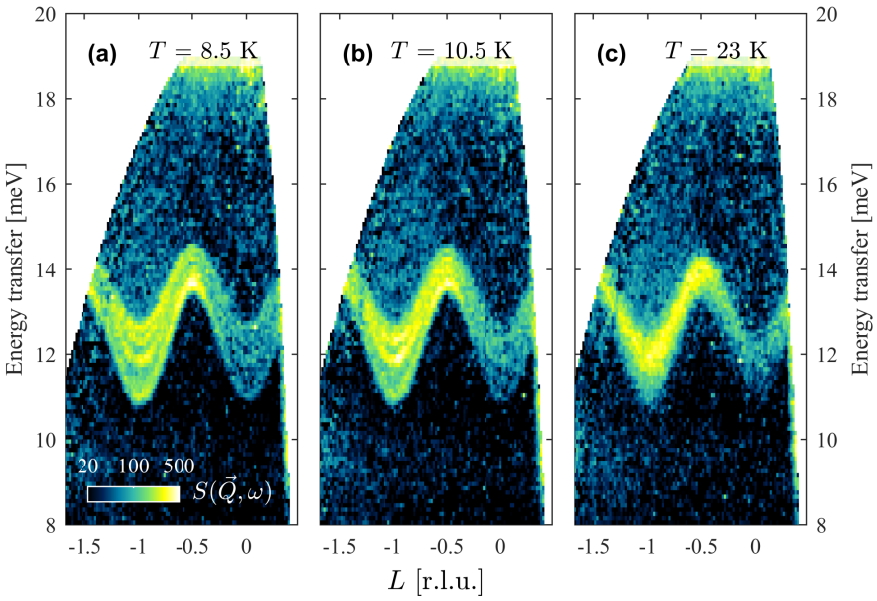

Figure 3.11: Slices of the experimental data at (a) 8.5, (b) 10.5 and (c) 23 K. The data is averaged with respect to H and K, and is displayed with a common logarithmic scale.

- Between T_{N2} and T_{N1} a similar picture is measured, although the central peak is sharper and the tails are less pronounced.
- Below T_{N1} we observe a series of sharp lines. The lowers-lying in energy (between 11 and 13.8 meV) is not a single mode but a very sharp continuum, while the modes at higher energies (respectively between 12.5 and 14.25 meV, 15 and 16.5 meV, 17 and 18 meV) are resolution-sharp. At 8.5 K and 10.5 K more dispersive lines can be seen at intermediate energies.

3.4.3 Further experiments on $RbCoCl_3$

While I will be discussing mostly the data obtained in the 2011 LET experiment, there have been a number of other INS measurements.

Part of them were performed at triple-axis instruments, namely IN20 (ILL, France) and EIGER (SINQ, PSI, Switzerland), performing scans a

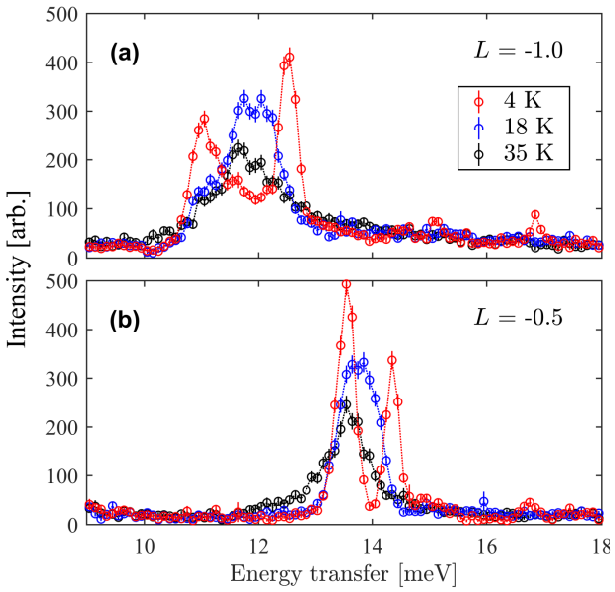

Figure 3.12: Cuts of the experimental data at 4 (red), 18 (blue) and 35 K (black). The data is averaged for (a) -1.05 < L < -0.95 and (b) -0.55 < L < -0.45, i.e. the point of maximum and minimum extent of the dispersion.

much smaller number of $\vec{Q}$-points but at more temperatures. The analysis of this data has been performed Dr. E. Hirtenlechner, and these results can be found in her thesis [41].

Another experiment on LET was however performed in spring 2015. The goal of this experiment was to apply a magnetic field to observe its effect on the soliton dispersion, but it also offered some other insight. These results will be discussed later, and only briefly.

3.5 Modelling of the system

The problem of the low-energy effective spin Hamiltonian of the family of compounds ABX_3 has attracted attention for being one of the closest realizations of several ideal theoretical paradigms. However, the spin Hamiltonian is still the subject of some controversy. A short historical perspective follows here.

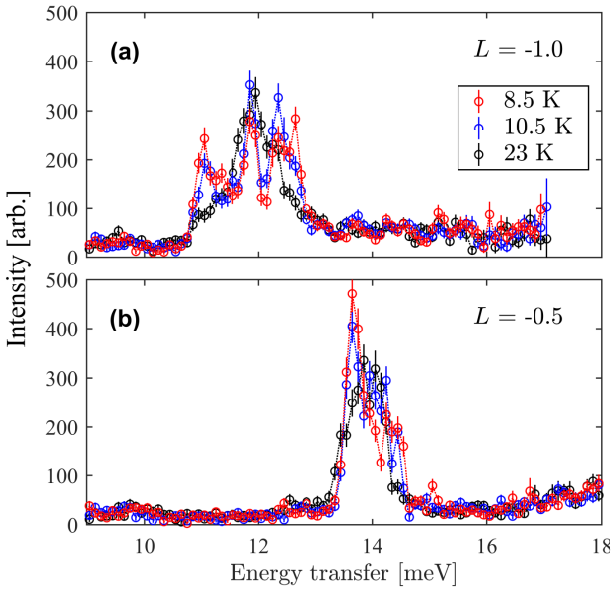

Figure 3.13: Cuts of the LET experimental data at 8.5 (red), 10.5 (blue) and 23 K (black). The data is averaged for (a) -1.05 < L < -0.95 and (b) -0.55 < L < -0.45.

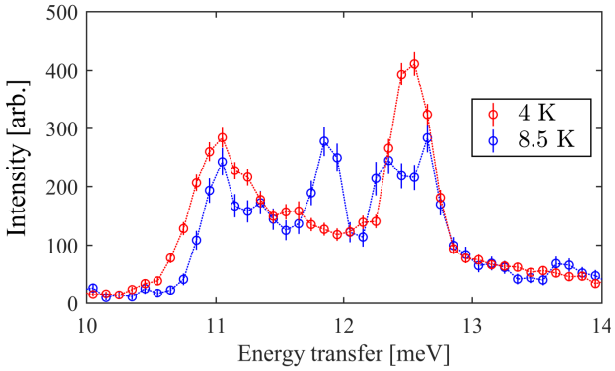

Figure 3.14: Cuts of the LET experimental data at 4 (red) and 8.5 K (blue). The data is averaged for -1.05 < L < -0.95 and displays the appearance of a mode at 11.9 meV, as well as a decrease in the intensity of the mode at 12.5 meV.

The solution of the Ising model The one-dimensional Ising model, named after Ernst Ising [8, 77, 20], is one of the simplest and most celebrated models for spin systems. It was the basis for the understanding of several thermodynamic magnetic systems, as well as being the starting point for several, more complex systems it is worth mentioning Lars Onsager's analytical solution of the 2D lattice [78].

In its original formulation, it studies the 1D ferromagnetic Hamiltonian:

$$\mathcal{H}_{\text{Ising}} = -2J \sum_{j=1}^{N-1} \hat{S}_j^z \hat{S}_{j+1}^z - \sum_{j=1}^{N} h_j \hat{S}_j^z, \tag{3.1}$$

where J is a (positive) exchange interaction and h_j is a (local) magnetic field acting on the spins (in meV)[3]. The energy is trivially minimized by parallel spins.

The problem of the behaviour with respect to temperature of this system was first studied with statistical mechanics. As a reminder, given a spin configuration $\{S^z\} = (S_j^z)_{\forall j}$ we can write the partition function[4] as

$$\mathcal{Z} = \sum_{\{S^z\}} e^{-\beta \mathcal{H}_{\text{Ising}}(\{S^z\})}, \tag{3.2}$$

where $\beta = 1/k_B T$, with k_B the Boltzmann constant. The probability of a single configuration obeys the Boltzmann statistics:

$$p(\{S^z\}) = \frac{e^{-\beta \mathcal{H}_{\text{Ising}}(\{S^z\})}}{\mathcal{Z}}. \tag{3.3}$$

The expectation of any observable f of the spin configuration (e.g. the magnetization) can be calculated as a weighted average:

[3]Notations vary in literature. In this convention, flipping the j-th spin has an energy cost of h_j.

[4]Temperature dependences of several functions, such as $\mathcal{Z} = \mathcal{Z}(T)$, are omitted

$$\langle f \rangle = \sum_{\{S^z\}} f(\{S^z\})\, p(\{S^z\}) \tag{3.4}$$

and, without derivation, the energy of the system is

$$\langle E \rangle = -\frac{1}{\mathcal{Z}} \frac{\partial \mathcal{Z}}{\partial \beta} = -\frac{\partial \ln(\mathcal{Z})}{\partial \beta} \tag{3.5}$$

It is a well-known fact that the magnetization of the 1D Ising chain (in a homogeneous field) is

$$\begin{aligned} m(T) &= \frac{1}{\beta N} \frac{\partial \ln(\mathcal{Z})}{\partial h} = ... = \\ &= \frac{\sinh(\beta h)}{\sqrt{\cosh^2(\beta h) - 2e^{-4\beta J}\sinh(4\beta J)}}. \end{aligned} \tag{3.6}$$

There are no magnetic phase transitions in the absence of a magnetic field, as $m(T) \propto \sinh(\beta h) = 0 \forall T$ if $h = 0$. This is interpreted in terms of the maximization of entropy prevailing over the minimization of energy. This is not true in higher dimensions due to the increase in the coordination number, which already in 2D is enough to induce a phase transition [78].

This is a strong argument for the relevance of the interactions in the plane in RbCoCl3, without which the system could not order.

The Ising problem and the Bethe solution. A more general expressions for a spin Hamiltonian is the xxz model, which can also be identified with a generalized anisotropic Heisenberg model[5]:

[5] As a remark about conventions, the convention used through this work is such that $S^z = \pm 1/2$ and the energy required to excite a spin from the ordered AF ground state, i.e. creating two domain walls, is $2J$.

$$\mathcal{H}_{xxz} = 2\sum_j \left(J_{zz}S_j^zS_{j+1}^z + J_{xy}(S_j^xS_{j+1}^x + S_j^yS_{j+1}^y)\right)$$
$$=: 2J\sum_j \left(S_j^zS_{j+1}^z + \epsilon(S_j^xS_{j+1}^x + S_j^yS_{j+1}^y)\right). \tag{3.7}$$

This expression has several special cases, notably the isotropic Heisenberg Hamiltonian for $J_{xy} = J_{zz}$ or $\epsilon = 1$ [9], the Ising Hamiltonian for $J_{xy} = 0$ or $\epsilon = 0$ [8], and the xy model $J_{zz} = 0$. The case $\epsilon \ll 1$ is called Ising-like, or quasi-Ising.

The properties of the anisotropic Heisenberg model have been studied extensively since the 1930's [48, 49, 50]. Famously, the Bethe Ansatz [51, 52, 53] permits the determination of the spectrum both in the case $\epsilon = 1$, i.e. the Heisenberg case [54], and in the case $\epsilon < 1$ [55]. These solutions are called respectively the des Cloizeaux-Pearson (dC-P) and des Cloizeaus-Gaudin (dC-G) spectra.

The excitation can be characterized as singlet-to-triplet and therefore has three branches, corresponding to the quantum number of the quasi-particle: $\hbar\omega_{-1}$, $\hbar\omega_0$ and $\hbar\omega_1$, which in neutron scattering can be interpreted as flips, or lack thereof, of the spin of the neutron. To express the dispersion one needs to define the intermediate variable ϕ_0, which for $\epsilon =: 1/\cosh(\Phi) < 1$ satisfies:

$$|L| = \frac{1}{2} - \frac{2}{\pi}\sum_{n=-\infty}^{\infty}\left(\operatorname{atan}\big(\exp(\frac{\phi_0\pi}{2\Phi} + \frac{n\pi^2}{\Phi})\big) - \operatorname{atan}\big(\exp(\frac{n\pi^2}{\Phi})\big)\right). \tag{3.8}$$

This relation maps bijectively $\phi_0 \in [-\pi,\pi]$ into $L \in [0,1]$. Then:

$$\hbar\omega_0(L) = \frac{J\pi}{2\Phi}\sum_{n=-\infty}^{\infty}\left(\frac{\sinh(\Phi)}{\cosh(\frac{\pi\phi_0}{2\Phi} + \frac{n\pi^2}{\Phi})} - \frac{\sinh(\Phi)}{\cosh(\frac{\pi^2}{2\Phi} + \frac{n\pi^2}{\Phi})}\right), \tag{3.9}$$

$$\hbar\omega_{\pm1}(L) = \frac{J\sinh(\Phi)}{2}\sum_{n=-\infty}^{\infty}\frac{e^{-in\phi_0} + (-1)^n}{\cosh(n\Phi)}. \tag{3.10}$$

Figure 3.15 shows the dispersions for three values of ϵ: $\hbar\omega_0$ are gapless spin waves, while $\hbar\omega_{\pm1}$ are gapped.

There are several compounds, e.g. in CuCl·2N(C_5D_5) [56], that realize these predictions.

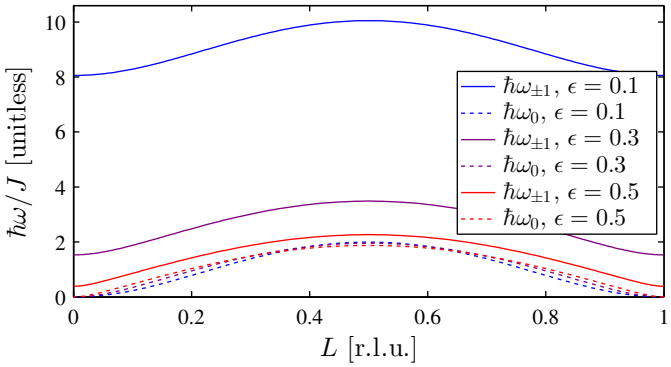

Figure 3.15: dC-G dispersion of the 1D XXZ model calculated for three values of ϵ according to Eqs. (3.8-3.9). Dotted curves are $\hbar\omega_0$ and solid curves are $\hbar\omega_{\pm1}$. For $\epsilon = 1$, all modes are degenerate.

M. Mekata (1976) and the magnetic order of the planes. An AF hexagonal lattice is a prototypical candidate for frustration, yet several diffraction experiments had found evidence of planar order in the isostructural compounds $CsCoCl_3$, $CsCoBr_3$ and $RbCoCl_3$, namely magnetic reflections at (1/3 1/3 1) and (1 1 1) [57, 58, 59, 60]. M. Mekata [61] rigorously showed that an hexagonal lattice with an AF *nn* interaction (J_{nn}) and a weaker FM *nnn* interaction (J_{nnn}) in the absence of an external magnetic field can have up to three local energy minima. By labelling $< \sigma_{1,2,3} >$ the average *relative magnetization*[6] of the chains of the three inequivalent sites of the extended unit cell[7] of the hexagonal lattice, the non-trivial solutions are:

- $< \sigma_1 > = < \sigma_2 > = - < \sigma_3 >$, the ordered honeycomb lattice. This

[6]The total magnetization of an AF chain is clearly zero. Consistently with the nomenclature used by M. Mekata, the relative magnetization is calculated as $\sum_j (-1)^j S_j^z$ and is non-zero when the chain is ordered.

[7]In the extended unit cell, the lattice vectors (which are $\sqrt{3}$ times longer) connect a magnetic site with its next-nearest neighbour. The c axis remains the same.

phase is ferrimagnetic.

- $< \sigma_1 >= 0$ and $< \sigma_2 >= - < \sigma_3 >$, the partially disordered (PD) phase. The average magnetization of a plane is zero. $< \sigma_1 > = 0$ mean that the chain is disordered, which does not preclude short-range order.

- $< \sigma_1 >=< \sigma_2 >$ and $< \sigma_1 > \neq < \sigma_3 >$, a solution that is sometimes called the 3-site ferrimagnetic phase. There is no constraint on $< \sigma_3 >$.

It was shown that these solutions exhibit magnetic reflections of different magnitude at (1/3 1/3 1); it was moreover suggested that the appreciable change in intensity measured in the experiments was due to a transition between the ferrimagnetic state ($T < T_{N2}$) and the PD state ($T_{N2} < T < T_{N1}$). The Néel temperature was approximated as

$$T_{N1} = \frac{6S^2}{k_B}(2J_{nnn} - J_{nn}) \tag{3.11}$$

although no equivalent expression was derived for T_{N2}. In this first analysis the Néel temperature does not depend on the dominant in-chain AF exchange J.

N. Ishimura and H. Shiba (1980) and the domain-wall solution. As experimental evidence was being presented that several 1D compounds did not display spin waves or spinons, it was argued by N. Ishimura and H. Shiba [44] that the Bethe Ansatz did not capture the behaviour of the system in the Ising-like regime. It was then proposed that ϵ acts as a perturbation of the pure Ising limit, whose ground state consists of spins pointing along z. Unlike in the gapless dC-G spectrum, the excitations of an Ising system are couples of domain walls (i.e. solitons), which require an energy transfer around $2J$ to be created.

Furthermore, using $S^{\pm} = S^x \pm iS^y$ one can rewrite Eq. (3.7) as.

$$\mathcal{H}_{\mathrm{IS}} = 2J \sum_j \left(S_j^z S_{j+1}^z + \frac{\epsilon}{2} (S_j^+ S_{j+1}^- + S_j^- S_{j+1}^+) \right) =$$
$$=: \mathcal{H}^{zz} + \mathcal{H}^{\pm}. \tag{3.12}$$

While $\mathcal{H}^{zz}$ fixes the ground state (i.e. Ising chains) and its excited states (i.e. couples of domain walls), $\mathcal{H}^{\pm}$ allows the domain walls to move independently one from the other along the chain.

In order to analytically find the excitations of this system, we start with the doubly-degenerate Néel ground states of the unperturbed chain, $|\text{Néel}, \searrow\rangle = |... \uparrow\downarrow\uparrow\downarrow ...\rangle$ and $|\text{Néel}, \nearrow\rangle = |... \downarrow\uparrow\downarrow\uparrow ...\rangle$, but due to symmetry we can consider just one Néel state. The base elements of the excited Hilbert space are:

$$|\vec{Q}, 1\rangle = \sqrt{\frac{2}{N}} \sum_j e^{i\vec{Q}\cdot\vec{R}_j} S_j^+ \, |\text{Néel}, \nearrow\rangle \,,$$
$$|\vec{Q}, 3\rangle = \sqrt{\frac{2}{N}} \sum_j e^{i\vec{Q}\cdot\vec{R}_j} S_j^+ S_{j+1}^- S_{j+2}^+ \, |\text{Néel}, \nearrow\rangle \,,$$
$$|\vec{Q}, \nu\rangle = \sqrt{\frac{2}{N}} \sum_j e^{i\vec{Q}\cdot\vec{R}_j} S_j^+ \dots S_{j+\nu-1}^+ \, |\text{Néel}, \nearrow\rangle \,,$$

where N is the number of spins in the chain and ν represents the distance between the domain walls. In this base we can now express the Hamiltonian $\mathcal{H}_{\mathrm{IS}}$ in matrix form:

$$\langle \vec{Q}, \nu | \mathcal{H}_{\mathrm{IS}} | \vec{Q}, \nu' \rangle = \begin{cases} 2J & \text{for } \nu = \nu' \\ V & \text{for } \nu = \nu' - 2 \\ V^* & \text{for } \nu = \nu' + 2 \\ 0 & \text{otherwise} \end{cases} \tag{3.13}$$

with $V = \epsilon J \, (1 + e^{-2i\pi L})$. Figure 3.16(a) shows the solutions of the di-

agonalization of this matrix: for $N \to \infty$ they form a continuum of excitations between the extremal modes $\hbar\omega_1(L) = 2J(1 - 2\epsilon\cos(\pi L))$ and $\hbar\omega_2(L) = 2J(1 + 2\epsilon\cos(\pi L))$.

The next question to be addressed is the spectral weight of the modes, which are dominated by the transverse response S_{xx}. Using Green theory, we can express it in the first order of ϵ as:

$$S_{xx}(L,\omega) \simeq -\frac{1}{4\pi}\mathrm{Im}\Big(\big(1-\epsilon\cos(\pi L)\big)^2\,\mathcal{G}(1,1) - ... \\ \big(1-\epsilon\cos(\pi L)\big)\big(\frac{V}{2J}\,\mathcal{G}(1,2) + \frac{V^*}{2J}\,\mathcal{G}(2,1)\big) + \mathcal{O}(\epsilon^2)\Big) \tag{3.14}$$

with the Green's function $\mathcal{G}(\nu,\nu')$ defined as:

$$\mathcal{G}(\nu,\nu') = \langle\vec{Q},\nu|\,(\hbar\omega - \mathcal{H}_{\mathrm{IS}} + i\delta)^{-1}\,|\vec{Q},\nu'\rangle \tag{3.15}$$

where δ is small enough. A simulation of S_{xx} is presented in Fig. 3.16(b-c).

The equivalence between $S_{xx}(L,\omega)$ and $S_{yy}(L,\omega)$ is trivial due to the symmetry of the Hamiltonian. N. Ishimura and H. Shiba also computed the other terms, such as $S_{zz}(L,\omega)$, concluding that their spectral weight is two orders of magnitude weaker than $S_{xx}(L,\omega)$. This term will be neglected in this work.

H. Shiba (1980) and the Zeeman ladder. The Ishimura-Shiba (IS) solution holds only for ordered chains that do not interact with their surrounding. N. Shiba [62] added a molecular field to Eq. (3.12):

$$\mathcal{H}_{\mathrm{S}} = \mathcal{H}_{\mathrm{IS}} - \sum_j h_j S_j^z \tag{3.16}$$

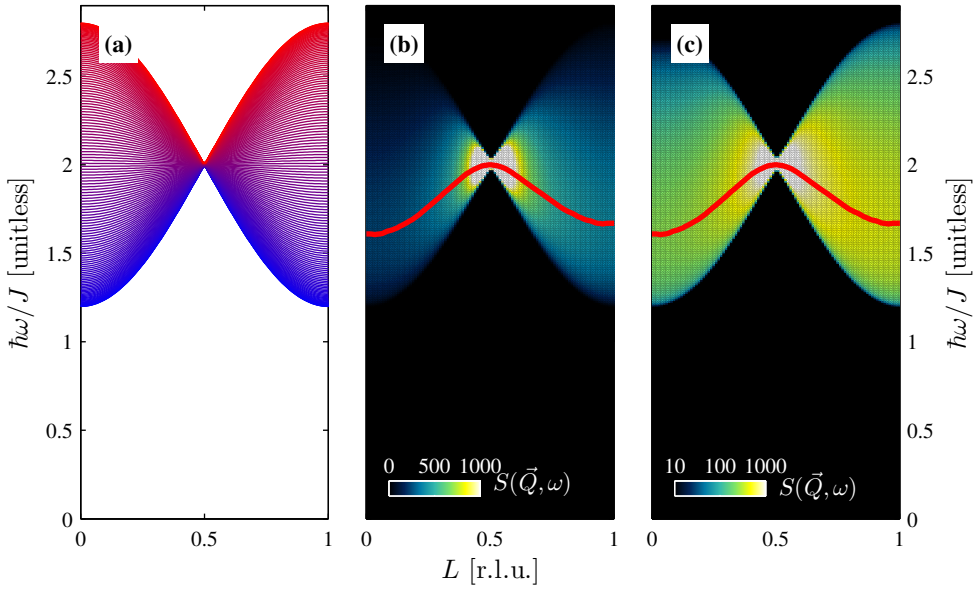

Figure 3.16: Simulations of the Ishimura-Shiba Hamiltonian. (a) The complete spectrum of the Hamiltonian (3.13) for an arbitrary value of $\epsilon = 0.2$. The soliton excitations form a bow-tie-shaped continuum around $2J$. (b) Simulation of the neutron scattering intensity in the (0 0 L) plane calculated using Eq. (3.14). The red curve represents the maximum intensity as a function of L. (c) The same as (b) in logarithmic colour scale.

where the *staggered field* h_j is the sum of the interactions in the plane; under the assumption that only nearest-neighbour interactions are relevant, this is

$$h_j = J_{nn} \sum_{k \in \hexagon} S^z_{k,j} \tag{3.17}$$

where (k, j) are the six spins on the j-th plane that neighbour the j-th spin of the chain. This expression can be generalized to the next-nearest neighbours, or to any number of neighbours, by introducing a series of interaction parameters (J_{nnn} and so on).

It was noted that this Hamiltonian is formally equivalent to that of the 1D tight-binding model for electrons in a uniform electric field. The excitations of the latter system are quantized and referred to as *Stark ladder*; by analogy the quantized soliton spectrum was called a *Zeeman ladder*. Previous magnon Raman spectra [63, 64] were interpreted in terms of a Zeeman ladder, the *nn* interaction explaining the staggered field. At the phase transition at T_{N2} the weight associated to each staggered field changed: at lower temperatures the Raman scattering was dominated by $h_j = 6J_{nn}$ in accordance with Mekata's prediction for the honeycomb lattice, while at intermediate temperatures the Zeeman ladder induced by $2J_{nn}$ and $4J_{nn}$ gained intensity because of the thermal disorder. In analogy to Eq. (3.13), this Hamiltonian can be expressed as:

$$\langle \vec{Q}, \nu | \mathcal{H}_{\mathrm{S}} | \vec{Q}, \nu' \rangle = \begin{cases} 2J(1+\epsilon^2) + h & \text{for } \nu = \nu' = 1 \\ 2J(1+\frac{3}{2}\epsilon^2) + \nu h & \text{for } \nu = \nu' > 1 \\ V & \text{for } \nu = \nu' - 2 \\ V^* & \text{for } \nu = \nu' + 2 \\ V_2 & \text{for } \nu = \nu' - 4 \\ V_2^* & \text{for } \nu = \nu' + 4 \\ 0 & \text{otherwise} \end{cases} \tag{3.18}$$

with $V_2 = -\frac{\epsilon^2}{2} J \left(1 + e^{-4i\pi L}\right)$. The quadratic terms in ϵ are included in order to offer a better qualitative agreement with the experimental data.

It was moreover noted that Eq. (3.11), having been derived in a purely two-dimensional context, was insufficient to relate the phase transition temperatures and the magnitude of the exchange interactions. Using Scalapino-Imry-Pincus theory [65], the following set of conditions could be obtained:

$$\begin{aligned} 2k_B T_{N2}\, e^{-J/k_B T_{N2}} &= -6J_{nnn}, \\ 2k_B T_{N1}\, e^{-J/k_B T_{N1}} &= 3J_{nn} - 6J_{nnn}. \end{aligned} \tag{3.19}$$

Applied to $CsCoCl_3$, this means $J = 6.46$ meV, $J_{nn} \sim 0.36$ meV and $J_{nnn} \sim 0.01 J_{nn}$.

F. Matsubara (1991) and further Raman scattering. While H. Shiba had provided a good model to motivate the ladder of excitations and W. Lehmann *et al.* [66] further compared calculations and experimental results (mostly Raman spectroscopy), F. Matsubara *et al.* [67] noticed that some outstanding discrepancies remained unaddressed: firstly, different values of ϵ had been proposed for each branch of the Zeeman ladder (a result necessary for the fitting but unphysical), and that the experimental weights associated with different staggered fields didn't behave as theoretically predicted.

In order to solve these important issues, a FM *nnn* interaction J_2 along the chains was introduced (the *nn* AF interaction, previously J, is from here onwards noted as J_1). The Hamiltonian is then written as

$$\begin{aligned}\mathcal{H}_{\mathrm{M}} = &\sum_j 2J_1\big(S_j^z S_{j+1}^z + \epsilon(S_j^x S_{j+1}^x + S_j^y S_{j+1}^y)\big) + \\ &\sum_j 2J_2\big(S_j^z S_{j+2}^z + \epsilon(S_j^x S_{j+2}^x + S_j^y S_{j+2}^y)\big) + \\ &\sum_j h_j^{ic} S_j^z,\end{aligned} \tag{3.20}$$

and its matrix form is

$$\langle \vec{Q}, \nu | \mathcal{H}_{\mathrm{M}} | \vec{Q}, \nu' \rangle = \begin{cases} 2J_1(1+\epsilon^2) + 2J_2\big(1 - \epsilon\cos(2\pi L)\big) + h & \text{for } \nu = \nu' = 1 \\ 2J_1(1+\frac{3}{2}\epsilon^2) + 4J_2 + \nu h & \text{for } \nu = \nu' \\ V & \text{for } \nu = \nu' - 2 \\ V^* & \text{for } \nu = \nu' + 2 \\ V_2 & \text{for } \nu = \nu' - 4 \\ V_2^* & \text{for } \nu = \nu' + 4 \\ 0 & \text{otherwise.} \end{cases} \tag{3.21}$$

Consistently, the Hamiltonian (3.18) is a special case of (3.21) for $J_2 = 0$. The authors claimed to have "excellently explained" the magnon Raman scattering in $CsCoCl_3$, $CsCoBr_3$ and $RbCoCl_3$ in terms of Ising chains with an AF *nn* interaction and a FM *nnn* interaction, $|J_1/J_2| \simeq 0.135$, and staggered fields induced by the in-plane *nn* interaction. They remarked that the weights associated with the staggered fields could be understood by considering the presence of ferrimagnetic domains in the planes: the typical domain size required to explain their ratios was typically 10 unit cells in the ordered phase and 5 unit cells in the intermediate phase.

J. Goff (1995) and the exchange mixing. Regarding the result $|J_2/J_1| \simeq 0.1$ by F. Matsubara *et al.* as being unphysically large, J. Goff *et al.* [68] described the splitting of the lowest Kramers doublet as asymmetric. In other terms, the energy difference between $|\uparrow\uparrow\downarrow\rangle$ and $|\uparrow\uparrow\uparrow\rangle$, noted as $J - \Delta$, is different from the energy difference between $|\uparrow\uparrow\downarrow\rangle$ and $|\downarrow\uparrow\downarrow\rangle$, which is $J + \Delta$. As a consequence, while exciting a soliton of length 1 spin costs $2J$, exciting a soliton of length 3 or more costs $2J + 2\Delta$. The best approximation for Δ, self-consistently calculated starting from the known crystal-field parameters, was $0.09J$. Equation (3.13) is therefore modified as:

$$\langle \vec{Q}, \nu | \mathcal{H}_{\mathrm{G}} | \vec{Q}, \nu' \rangle = \begin{cases} 2J + h & \text{for } \nu = \nu' = 1 \\ 2J + 2\Delta + \nu h & \text{for } \nu = \nu' \\ V & \text{for } \nu = \nu' - 2 \\ V^* & \text{for } \nu = \nu' + 2 \\ 0 & \text{otherwise.} \end{cases} \tag{3.22}$$

No second-order terms in ϵ were introduced. A neutron inelastic experiment at MARI (ISIS, UK) was interpreted as in agreement with this model, and the authors suggested that there was no evidence for a large in-chain *nnn* interaction.

H. Shiba (2003) and the crystal-field excited states. Disagreements between the approaches and conclusions of F. Matsubara and J. Goff were apparent enough for H. Shiba *et al.* [69] to publish a theoretical study mentioning as a motivation, in their introduction, that "the relation between the two proposals as well as the question of which one is appropriate has not been clarified yet".

This study developed a theory of the crystal field states, analogous to that done by J. Goff, but to a different degree of approximation. Relations could be established between the (unknown) coefficients of the wave function

of the electrons around the Co^{2+} ions and the parameters J_1, J_2, ϵ_1 and ϵ_2 – the last one being the anisotropy of the *nnn* interaction. With some educated guesses it was then suggested that:

- the sign of J_2 is opposite to the sign of J_1, i.e the in-chain *nnn* interaction is FM if the *nn* interaction is AF;
- ϵ_1 and ϵ_2 have distinct values;
- ϵ_1 is likely to be small (Ising-like);
- ϵ_2 is likely to be close to unity.

No information about the in-plane interactions J_{nn} and J_{nnn} could be derived using his method.

Comparison between experimental magnetization curves of $CsCoCl_3$ and theoretical predictions based on this theory give an overall good agreement for $J_1 \sim 6.5$ meV, $\epsilon_1 = 0.16$, $-J_2/J_1 \sim 0.07$ and $\epsilon_2 \sim 0.7$. This study concluded noting that the presented approach is in agreement with F. Matsubara's phenomenological model, and is not in contradiction with J. Goff's proposal – pointing out that the mean-field approach used in the latter is the reason why the Hamiltonians are different.

Todoroki (2004) and the phase transitions of the plane. The exact nature of the two phase transitions, as well as the role of the 3-site ferrimagnetic phase described by M. Mekata, was not perfectly clear. Using a Monte Carlo algorithm, Todoroki *et al.* [70] argued that the 3-site ferrimagnetic phase is never realized. They also calculated the density of domain walls along the chains on each sublattice of the extended unit cell, revealing a sharp increase in one site at roughly $T = J/5k_B$, a temperature compatible with T_{N2}. They concluded that the transition from the ferrimagnetic phase to the PD phase is physically explained by a discontinuous increase in domain wall density in one site, which becomes disordered. Since the number of domain walls is small compared to the number of spins in the sample,

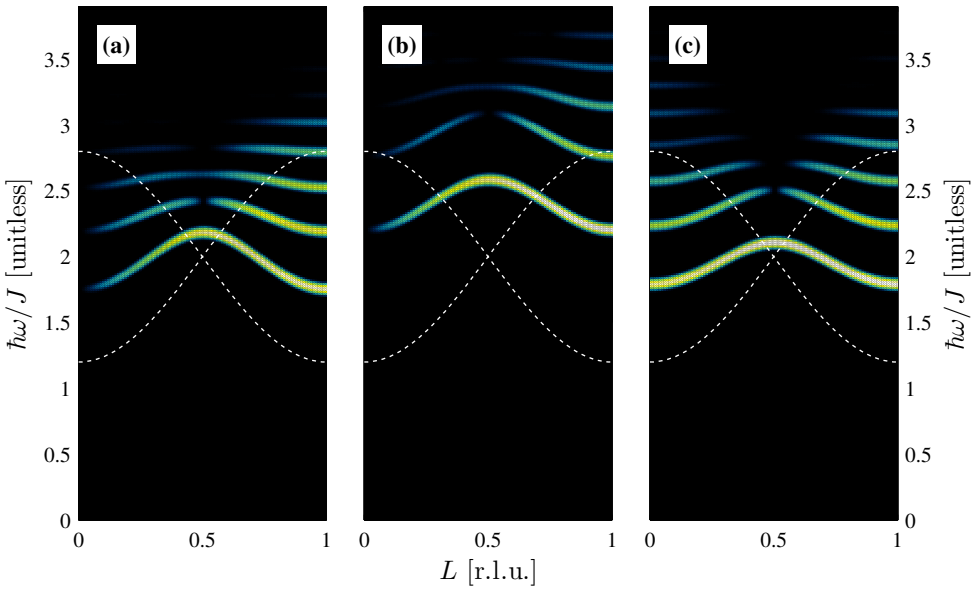

Figure 3.17: Simulations of $S_{xx}(\vec{Q},\omega)$ for three Hamiltonians. The staggered field results in the appearance of a Zeeman ladder. The white dotted curves mark the boundaries of the IS continuum, see Fig. 3.16, outlining the vestigial bow-tie shape of the Zeeman ladders. The intensity is in logarithmic scale. (a) $S_{xx}(\vec{Q},\omega)$ calculated after H. Shiba's Hamiltonian, Eq. (3.18), for arbitrary values $\epsilon = 0.2$ and $h = J/10$. (b) $S_{xx}(\vec{Q},\omega)$ calculated after F. Matsubara's Hamiltonian, Eq. (3.21), for arbitrary values $\epsilon = 0.2$, $h = J/10$ and $J' = J/6$. (c) $S_{xx}(\vec{Q},\omega)$ calculated after J. Goff's Hamiltonian, Eq. (3.22), for arbitrary values $\epsilon = 0.2$, $h = J/10$ and $\Delta = J/10$.

this also explains why this 1st order phase transition has a minimal latent heat.

Summary The low-energy spin Hamiltonian of the compounds of the family ABX_3 (importantly $CsCoCl_3$, $CsCoBr_3$ and $RbCoCl_3$), and its excitations, have been studied in several iterations. A summary of its proposed key properties is given here.

- The 1D chains are dominated by AF *nn* Ising-like interactions, whose lowest-lying excitations are couples of moving domain walls, i.e. solitons, and form a continuum in the case of the isolated chain (N. Ishimura and H. Shiba).
- The crystal field induces corrections to the in-chain interactions, either an asymmetric splitting of the Kramers doublet (J. Goff) or a FM *nnn* interaction (F. Matsubara, H. Shiba).
- The in-plane neighbours are necessary to explain the emergence of the honeycomb order, and have been linked to two phase transitions at temperatures much lower than the main exchange interaction J. In particular, there is a strong indication that AF *nn* and FM *nnn* exchanges in the plane are necessary to induce the ferrimagnetic state at the lowest temperatures (M. Mekata).
- The in-plane interactions induce a staggered field that splits the continuous spectrum into a Zeeman ladder (H. Shiba). Each staggered field is associated with a population factor, which depends on the order of the plane.

Literature values for the various exchange parameters are given in Table (3.1). While they vary depending on the compound and on the specific modelling, there seems to be an agreement on $J \sim 6$ meV, ϵ between 0.1 and 0.2, and J_{nn} between one and two orders of magnitude below J. The study on $TlCoCl_3$ by A. Oosawa *et al.* [71] is the only experimental work,

to the best of our knowledge, to have interpreted the scattering exclusively as a IS continuum, while all other major works have modelled it in terms of a Zeeman ladder. Conversely H. Shiba was the only author to attempt at evaluating the *nnn* interaction J_{nnn}.

Spectral weight While the Hamiltonians are sufficient to calculate the energies, the spectral weight presented in Eqs. (3.14-3.15) has to be completed for the scope of a neutron scattering experiment by adding the polarization factor and the magnetic form factor, which for radially symmetrical ions has the general formula:

$$F(\vec{Q})^2 = Ae^{-a|\vec{Q}|^2} + Be^{-b|\vec{Q}|^2} + Ce^{-c|\vec{Q}|^2} + D. \tag{3.23}$$

The parameters for Co^{2+} are known: $A = 0.4332$, $a = 14.355$ Å^2, $B = 0.5857$, $b = 4.608$ Å^2, $C = 0.0382$, $c = 0.134$ Å^2, $D = 0.0179$ [74].

Additionally, in order to compensate the approximations used in obtaining 3.14, we introduced an empirical correction factor:

$$C_F(L) = 1 + f_1 \cos(\pi L/2) + f_2 \sin(\pi L/2) + f_3 \cos(\pi L) + f_4 \sin(\pi L). \tag{3.24}$$

This is just a Fourier Ansatz containing only $L/2$ and L as frequencies with coefficients f_ι to be fitted experimentally. It must be noted that while this expressions only contains L, it should be understood as $C_F\big(H(L), K(L), L\big)$. By construction $C_F(L)$ is difficult to associate to physical properties of the system, but merely serves to compensate to all the other approximations done during the derivations of the spectral weight.

3.5.1 Effects of the temperature

The effect of temperature is threefold. Firstly, the population factors associated with each staggered field depend on temperature. At the lowest

Compound	Author	J [meV]	ϵ	Other exchanges [meV]
$CsCoBr_3$	Lehmann [66]	7.81	∼0.2	$J_{nn} = 0.15$
	Nagler [72]	6.70	0.14	$J_{nn} = 0.40$
	Matsubara [67]	6.14	0.17	$J' = 0.61$ $J_{nn} = 0.16$
$CsCoCl_3$	Shiba [62]	6.46	0.13	$J_{nn} = 0.39$ $J_{nnn} = 0.004$
	Lehmann [66]	6.05	∼0.1	$J_{nn} = 0.076$
	Nagler [72]	6.19	0.12	$J_{nn} = 0.12$
	Matsubara [67]	5.48	0.15	$J' = 0.52$ $J_{nn} = 0.062$
	Goff [68]	6.37	0.15	$\Delta = 0.7$ $J_{nn} = 0.051$
$RbCoCl_3$	Lockwood [73]	∼6.0	∼0.1	$J_{nn} \simeq 0.18$
	Matsubara [67]	6.19	0.15	$J' = 0.84$ $J_{nn} = 0.12$
$TlCoCl_3$	Oosawa [71]	6.4	0.14	

Table 3.1: Values for the exchange parameters of ABX_3 quasi-Ising chain compounds as described in literature, ordered chronologically. These values have been found using various methods, such as Raman spectroscopy (e.g. F. Matsubara *et. al.*) or inelastic neutron scattering (e.g. J. Goff *et. al.*). Results are displayed to the second meaningful place if available, with no errors.

temperature we expect a honeycomb lattice with 1/3 of the spins experiencing a staggered field of -6J_{nn} and 2/3 of the spins experiencing none (their neighbours being inevitably three ups and three downs). At intermediate temperatures we expect the disorder in the plane to populate all possible fields. At the highest temperature we expect the staggered fields to average to zero due to the high population of solitons, and thus every chain to scatter similarly to an isolated chain.

The temperature also affects the order by introducing domain walls along the chains [70]. The density of domain walls grows continuously and leads to a reduction of the lifetime and of the mobility of the solitons.

Several studies focus on the dynamic structure factor of the thermal quasi-Ising chain. A result of particular interest to us [75] is that an increase in temperaturature leads to a narrower band, i.e. a decreased value for ϵ_1 (with no shift in J_1). This can be understood in terms of a decrease in mobility, as $\epsilon_1(S_j^+ S_{j+1}^- + S_j^- S_{j+1}^+)$ is the propagative term of the soliton.

A simplified model for the soliton lifetime is to assume an exponential decay, and Fourier transform of $e^{-\Gamma\omega}$, which is $\sqrt{2/\pi}$ $(\Gamma^2/(\Gamma^2+\omega^2) + \Gamma^2/(\Gamma^2-\omega^2))$, two Lorentzians. Hence, via the convolution with the Gaussian instrumental resolution, the lineshape of the soliton is expected to be a Voigt function with a fixed instrumental resolution σ and a temperature-dependent dampening $\Gamma(T)$ linked to the lifetime of the soliton.

The previously cited theoretical analysis [75] also highlights that this widening is in truth asymmetric. However we will use a conventional Voigt function as a simplified model for the lifetime of the particle.

3.5.2 Fitting procedure

The fitting was performed using functionalities of the MATLAB packages *Horace* [47] and *Spec1d* [76]. While the fit algorithm is conventional, the following points are brought to the attention of the keen reader:

- The four-dimensional data was simulated in its completeness (which makes a difference e.g. for the $|\vec{Q}|^2$-dependent magnetic form factor,

or the polarization factor). The simulation was then averaged to a L vs E slice, which was compared to the experimental data.

- The high-statistics data (i.e. 4, 18 and 35 K) were multifitted (i.e. fitted simultaneously) while the low-statistics data were not fitted. The result is therefore the best fit to the high-statistics data.

- In the absence of a reference run, the background was fitted to a collinear term $a_0 + a_1 E$.

- The in-plane *nnn* FM interaction, of magnitude J_{nnn}, is expected to be at least one order of magnitude below the in-plane *nn* AF interaction J_{nn}. Given a J_{nn} in units of some tenth of a meV, i.e. comparable with the instrumental resolution, J_{nnn} is too small to be observed.

- There are therefore four modes that should be observed experimentally, belonging to the staggered fields $h_{ic} = 0$, $2J_{nn}$, $4J_{nn}$ and $6J_{nn}$. The intensities of each single modes are expressed by a scale factor W_n – as a convention, the staggered field $h_{ic} = nJ_{nn}$ relates to W_n[8]. We will however more often present this as a *population factor*, i.e. $I_n = W_n/(W_0 + W_2 + W_4 + W_6)$, expressed as a percentage.

3.6 Analysis according to Matsubara's Hamiltonian

A multifit was performed to a $\chi^2 = 1.96$. The exchange parameters are presented in Table 3.2, where they are compared to F. Matsubara's results for $CsCoBr_3$, $CsCoCl_3$ and $RbCoCl_3$ for reference.

The values are found to be generally consistent with those found across the whole $ACoX_3$ family. A close comparison between the results for $RbCoCl_3$ highlights lower estimates for J_1, ϵ_1 and J_2, and a good agreement

[8] Conventions vary in literature. Particularly, Shiba [62] and Matsubara [67] use $\tilde{W}_C$ for I_0, $\tilde{W}_{B_2}$ for I_2, $\tilde{W}_{B_1}$ for I_4 and $\tilde{W}_A$ for I_6. This study prefers a more systematic naming scheme.

	Present work	$RbCoCl_3$ [67]	$CsCoCl_3$ [67]	$CsCoBr_3$ [67]
J_1	5.889(1)	6.19	5.48	6.14
ϵ_1	0.126(1)	0.15	0.15	0.17
J_2	0.518(1)	0.84	0.52	0.61
ϵ_2	0.605(1)	0.15	0.15	0.17
J_{nn}	0.129(1)	0.12	0.06	0.16

Table 3.2: Comparison of the fitted parameters between the present work (first column) and F. Matsubara's analysis of several $ACoX_3$ compounds [67]. The errors on these results are not available. All exchange parameters J are in meV, and isotropies ϵ are unitless. For the values of ϵ_1, only the result at 4 K is presented for this work. F. Matsubara's work assumed $\epsilon_2 = \epsilon_1$.

for J_{nn}. It must be noted that the comparison is not completely accurate as in F. Matsubara's work it was assumed that $\epsilon_1 = \epsilon_2$. However, as predicted by H. Shiba [69], we find ϵ_2 to be much closer to 1.

The instrumental resolution at the transfer energy of the soliton is 0.324(8) meV. The empirical correction factors, as explained in Eq. 3.24, are $f_{1,2,3,4}$ = 0.25(1), 0.52(1), 0.12(3) and -0.12(2).

In the following section, the fits will be presented and will be followed by an in-depth analysis of the changes with temperature of specific aspects, such as anisotropy, Lorentzian width, and distribution of the staggered fields. The problems of the higher branches of the Zeeman ladder will then be discussed.

3.6.1 Results at 35 K

A comparison between the experimental data and the associated fit result at 35 K is shown in Fig. 3.18. Cuts at the zone boundary and zone centre are shown in Fig. 3.19.

At this temperature we find $\epsilon_1 = 0.0955(4)$ and $\Gamma = 0.93(2)$ meV, which is much bigger than the instrumental resolution. Finally, 71(3) % of the

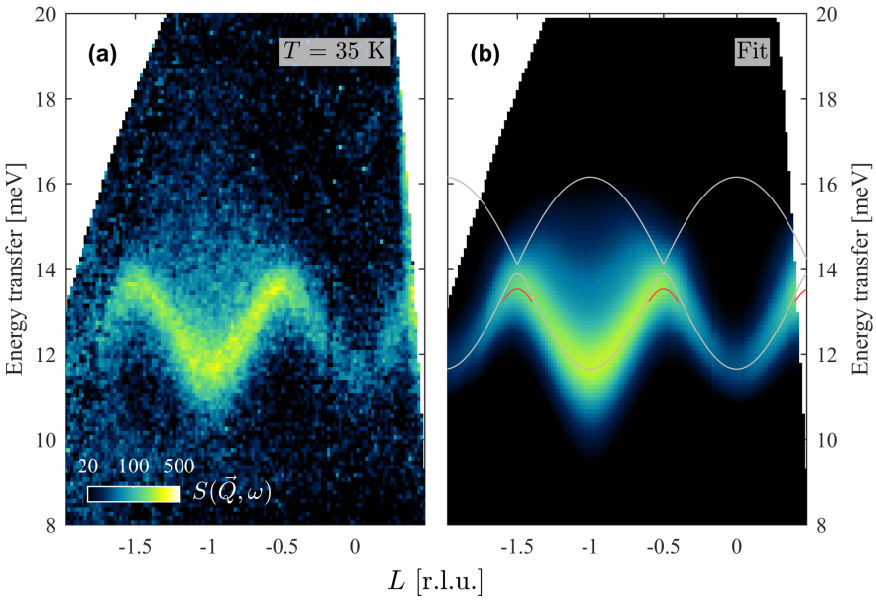

Figure 3.18: Slice of (a) the experimental results at 35 K and (b) fit thereof. In the fit, the grey lines mark the extent of the continuum and the red curves mark the bound mode that separates from the continuum L = -0.5.

scattering is associated to the non-staggered chain, $h_{ic} = 0$, and 28(4) % with $h_{ic} = 2J_{nn}$, with almost no contribution from more coordinated configurations. This is compatible with a scenario where thermal fluctuations prevent higher staggered fields from forming.

3.6.2 Results at 18 K

A comparison between the experimental data and the associated fit result at 18 K is shown in Fig. 3.20. Cuts at the zone boundary and zone centre are shown in Fig. 3.21.

As expected, ϵ_1 has increased to 0.112(1) and Γ has decreased to 0.25(1) meV, comparable with the instrumental resolution and roughly one quarter of its value at 35 K. The scattering is distributed as 38(1) % to $h_{ic} = 0$, 34(1) % to $h_{ic} = 2J_{nn}$, 26(1) % to $h_{ic} = 4J_{nn}$ and a negligible contribution from $h_{ic} = 6J_{nn}$.

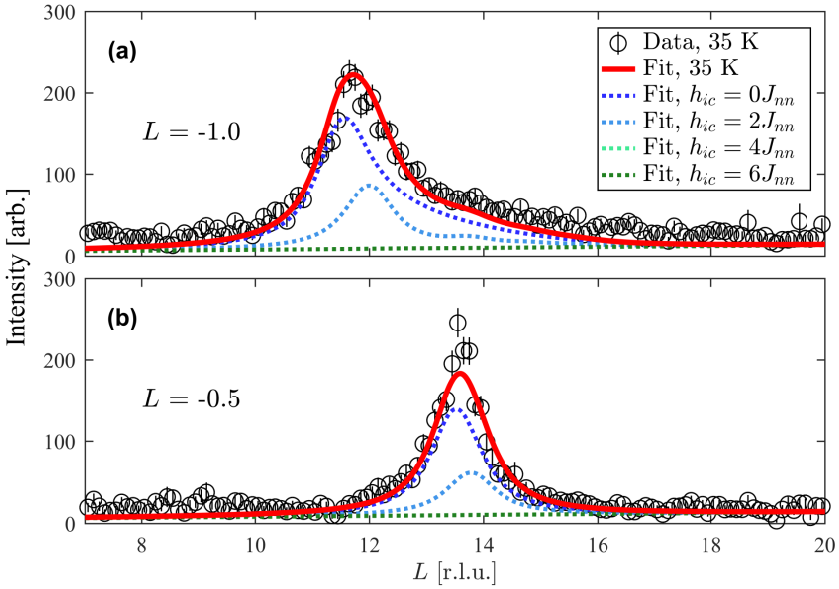

Figure 3.19: Comparison between cuts of the data (black) and the fit (red). The dotted blue-to-green curves show the contribution of single staggered fields h_{ic}, which are integer multiples of J_{nn}. The fit is dominated by the continuum-like spectrum of the isolated Ising chain, although there is a meaningful contribution from $h_{ic} = 2J_{nn}$.

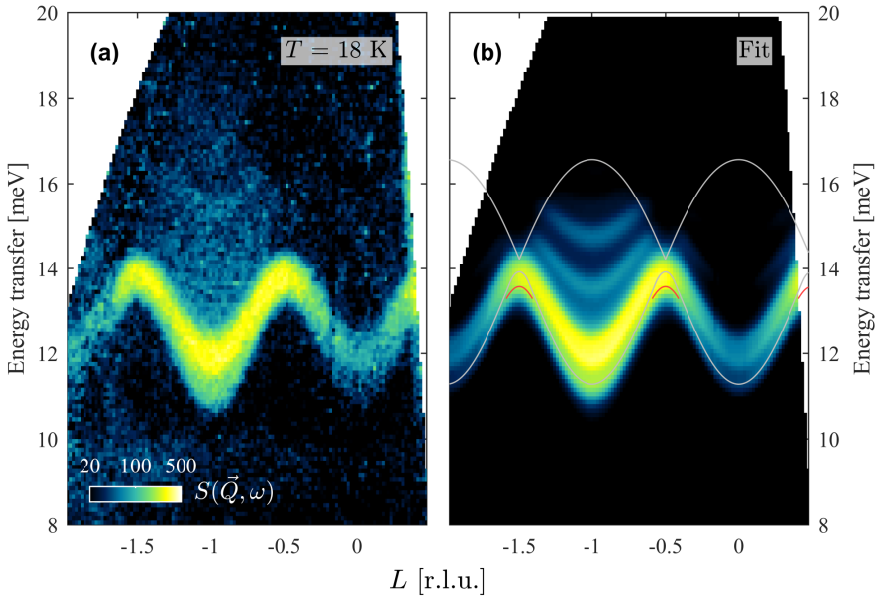

Figure 3.20: Slice of (a) the experimental results at 18 K and (b) fit thereof. In the fit, the grey curves mark the extent of the continuum and the red curves mark the bound mode that separates from the continuum around L = -0.5.

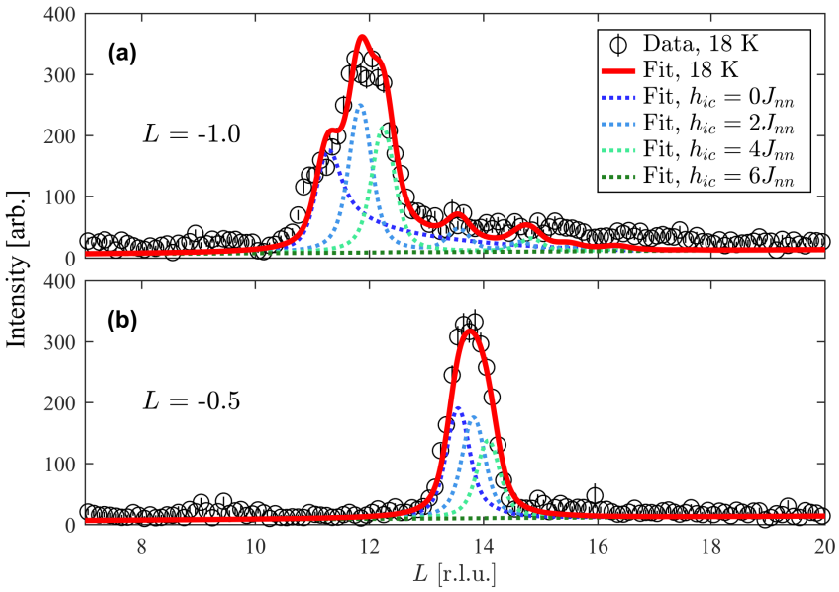

Figure 3.21: Comparison between cuts of the data (black) and the fit (red). The dotted blue-to-green curves show the contribution of single staggered fields h_{ic}, which are integer multiples of J_{nn}.

3.6.3 Results at 4 K

A comparison between the experimental data and the associated fit result at 4 K is shown in Fig. 3.22. Cuts at the zone boundary and zone centre are shown in Fig. 3.23.

At the lowest temperature, ϵ_1 has reached its maximum value of 0.125(1) and $\Gamma = 0.102(8)$ meV is negligible next to the instrumental resolution. The scattering is distributed as 66(2) % to $h_{ic} = 0$, 3(1) % to $h_{ic} = 2J_{nn}$, no contribution from $h_{ic} = 4J_{nn}$ and 30(1) % from $h_{ic} = 6J_{nn}$, i.e. distributed according to a honeycomb geometry.

Considerations about the higher modes of the Zeeman ladder, i.e. the two faint modes visible between 15 and 19 meV, will be discussed in section 3.8.2.

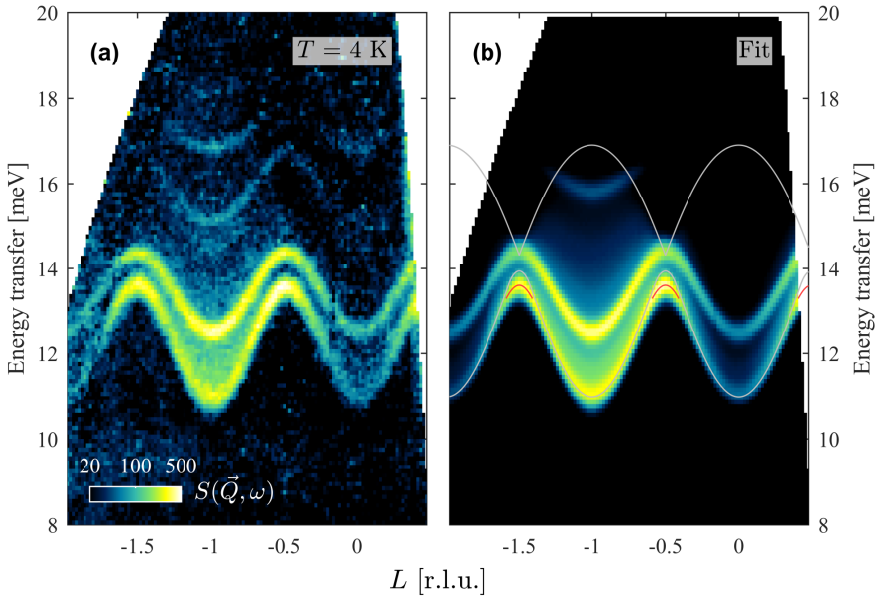

Figure 3.22: Slice of (a) the experimental results at 4 K and (b) fit thereof. In the fit, the grey curves mark the extent of the continuum and the red curves mark the bound mode that separates from the continuum around L = -0.5.

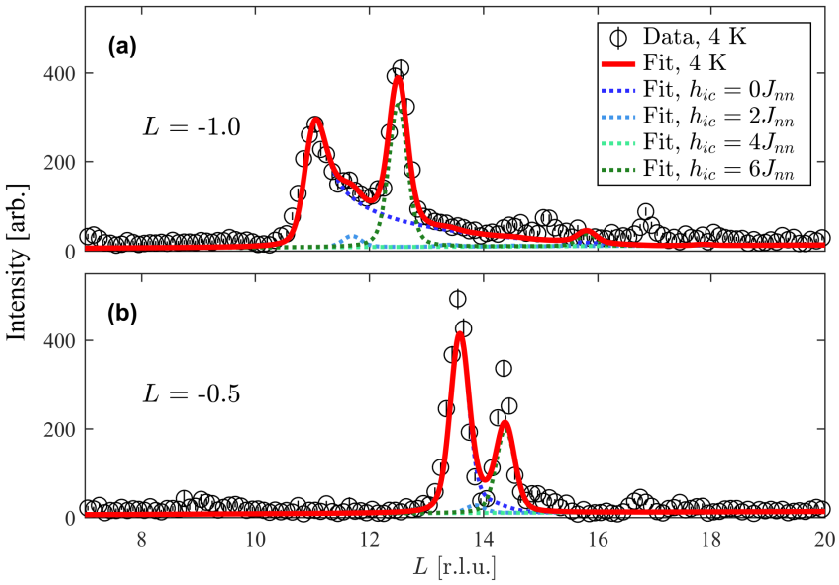

Figure 3.23: Comparison between cuts of the data (black) and the fit (red). The dotted blue-to-green curves show the contribution of single staggered fields h_{ic}, which are integer multiples of J_{nn}.

3.6.4 Fits at 8.5, 10.5 and 23 K

Subsequent fits were performed on the low-statics data using the results of the high-statistics data to ensure consistency. These fits are shown and explained in Figs. 3.24-3.26.

The decrease in incoming energy E_i from 25 to 20 meV severely affects the dynamic range that is sampled by neutrons; as a consequence the edge of the detector is much closer to the region of interest – this can be clearly appreciated in the much higher background at L = -1. Combined with the lower statistics, this results in a fit of lower precision.

The specific fitted parameters will be listed in the following sections when reviewing the evolution of single aspects with temperature.

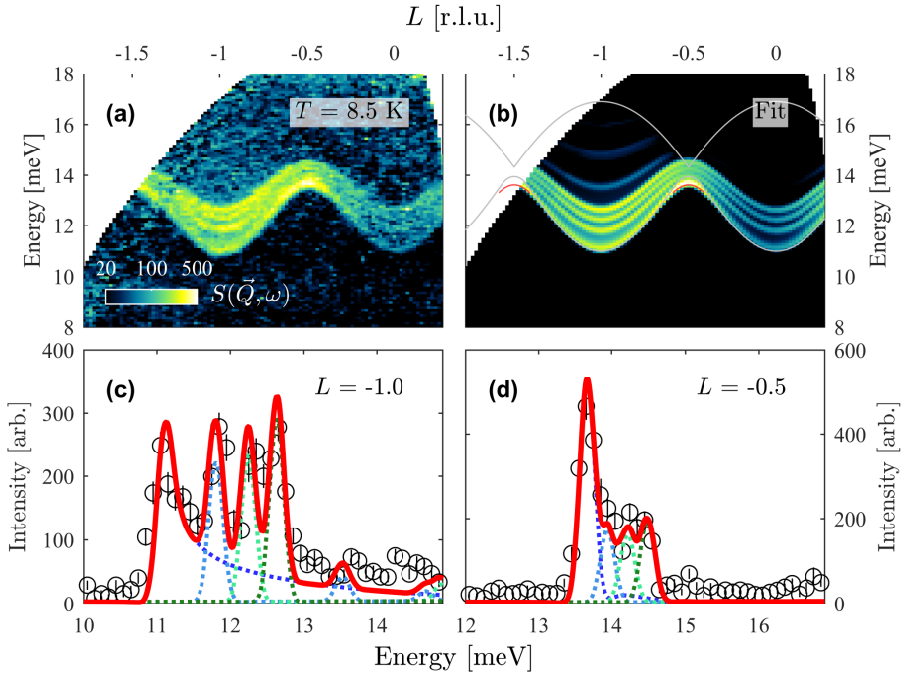

Figure 3.24: (a) Experimental data at 8.5 K. (b) Slice of the fit of the experimental data. The fit clearly displays four separate modes, corresponding to h_{ic} from 0 to $6J_{nn}$. (c) Cut of the data at L = -1.0, showing the fit and the single components. Refer to Fig. (3.23) for the legend. (d) Cut of the data at L = -0.5.

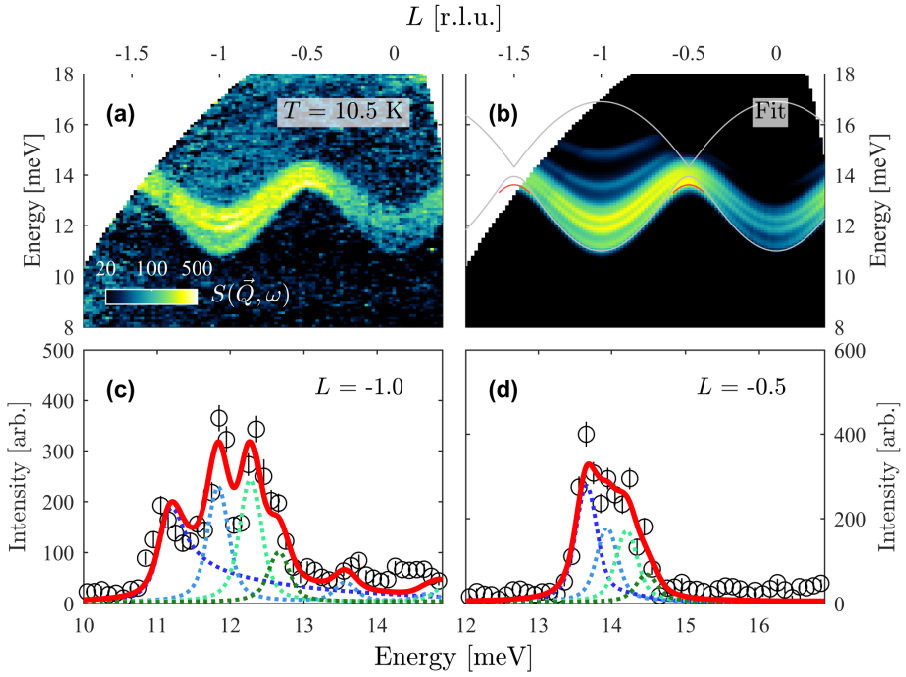

Figure 3.25: (a) Experimental data at 10.5 K. (b) Slice of the fit of the experimental data. The fit clearly displays four separate modes, corresponding to h_{ic} from 0 to $6J_{nn}$. (c) Cut of the data at L = -1.0, showing the fit and the single components. Refer to Fig. (3.23) for the legend. (d) Cut of the data at L = -0.5.

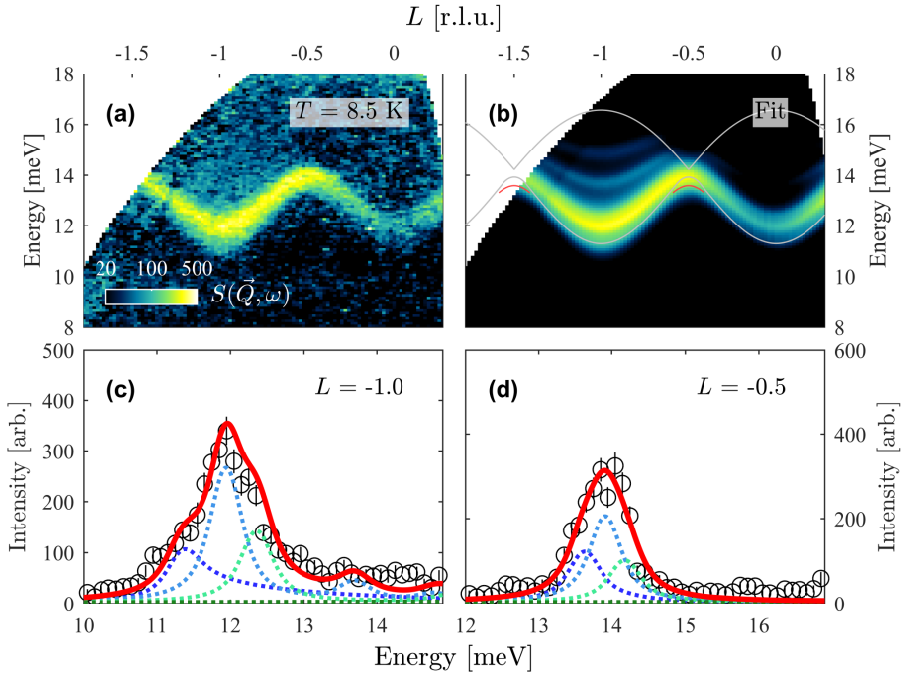

Figure 3.26: (a) Experimental data at 23 K. (b) Slice of the fit of the experimental data. The fit clearly displays four separate modes, corresponding to h_{ic} from 0 to $6J_{nn}$. (c) Cut of the data at L = -1.0, showing the fit and the single components. Refer to Fig. (3.23) for the legend. (d) Cut of the data at L = -0.5.

3.6.5 Mobility and lifetime as a function of temperature

Figure 3.27(a-b) show the anisotropy ϵ_1 and the Lorentzian width Γ as a function of temperature. As expected from the phenomenological argument from decreasing lifetime and mobility, ϵ_1 is a decreasing function of temperature while Γ is increasing.

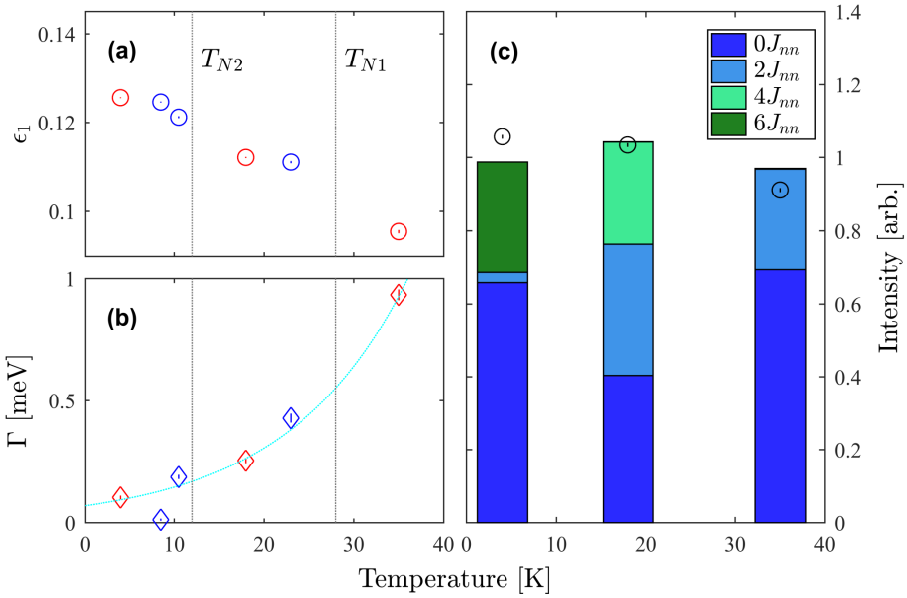

Figure 3.27: (a) Ising-like parameter ϵ_1 as a function of temperature. The decrease in ϵ_1 marks a decrease in the mobility of the solitons. Red (blue) points are taken from high-statistics (low-statistics) datasets. Dotted constant lines are drawn in each phase as a guide to the eye. (b) Lorentzian linewidth Γ as a function of temperature. The increase in Γ marks a decrease in lifetime. The azure exponential is a guide to the eye. The anomalous data point at 8.5 K is most likely the result of the imperfection of the fits of the low-statistics datasets. (c) Weights associated to each staggered field versus temperature, normalized so that their average is 1. The black data points are the integrated intensity of the raw data, also roughly scaled to unity.

T [K]	I_0	I_2	I_4	I_6
4	66(2)	3(1)	0(1)	30(1)
8.5	50(9)	16(3)	14(3)	18(3)
10.5	41(8)	25(5)	24(4)	9(2)
18	38(1)	34(1)	26(1)	0(1)
23	29(7)	48(9)	23(4)	0(1)
35	71(3)	28(4)	0(2)	0(1)

Table 3.3: Summary of the behaviour of the percentage of chains in a certain configuration. I_n is the percentage of scattering on a chain that experiences a staggered field $h_{ic} = nJ_{nn}$. The sum of the intensities does not reach 100% due to the errorbars.

3.6.6 Population factors as a function of temperature

Figure 3.27(c) shows the distribution of staggered fields as a function of temperature.

Aside from the integrated scattered intensity, which can be thought of as being roughly constant, Table 3.3 summarizes the percentages associated to each staggered field as a function of temperature.

Previous studies on $RbCoCl_3$, while generally agreeing on the population factors of the honeycomb lattice, considered diversified approaches to the thermal frustrated hexagonal lattice. A list of results in literature is presented in Table 3.4. For instance, for their only scan between T_{N2} and T_{N1}, at 17 K, J. Goff [68] assumed a perfectly random PDAF with coefficients of 5/12, 3/12, 3/12 and 1/12 (i.e. 42 %, 25 %, 25 % and 12 %) for h_{ic} from 0 to $6J_{nn}$, a distribution which is remarkably close to the populations factors found at 10.5 K – still below T_{N2}, but where the meaningful diffuse scattering suggests detectable amounts disorder.

The complexity of the temperature evolution of the population factors observed in this study is not fully grasped in the previous studies on these

T [K]	Author	I_0	I_2	I_4	I_6
2	Lehmann [66]	41	18	7	37
2	Goff [68]	67	0	0	33
2.3	Matsubara [67]	31	19	13	37
12	Lehmann [66]	14	43	29	10
13.7	Matsubara [67]	18	40	29	13
17	Goff [68]	42	25	25	12
$T > T_{N1}$	Goff [68]	100	0	0	0

Table 3.4: Overview of the population factors of the chains in literature. Note that the results by Lehmann and Goff refer to $CsCoCl_3$, while the results by Matsubara are for $RbCoCl_3$.

compounds, between which the results vary significantly. Qualitatively understanding the population factors requires a full thermodynamic modelling of the order in $RbCoCl_3$, which will be obtain via a Monte Carlo algorithm, as explained in the next section.

3.6.7 Cluster Heat Bath Monte Carlo method

Monte Carlo algorithms [79, 80] are a common numerical method to find simple solutions to complicated problems. The Metropolis-Hastings algorithm is a Markov chain[9] Monte Carlo method [82, 83, 84, 85, 86] that is commonly used in solid state physics [87]. In systems where only spin-flips are allowed, as is the case in Ising systems, it can be summarized as follows:

- Randomly create an initial set of spins.
- Randomly pick one spin. Calculate the energy difference dE between

[9] A Markov chain is a stochastic process (i.e. a collection of random variables that evolve in time) that satisfies the Markov property of being memoryless (i.e. a state can influence the probabilities that create the next state in the process, but does not influence any subsequent probability) [81].

the system before and after flipping the spin.

- If dE is negative, i.e. the total energy would decrease, always flip the spin. If dE is positive, i.e. the total energy would increase, there is a probability $e^{-\beta\, dE}$ that the spin is flipped. Flips are thus more likely when going against small energy gaps dE, or when the temperature is higher (and β smaller). This prevents the system from stopping in a local minima, and introduces thermal fluctuations and disorder.

- Randomly pick a new spin and repeat until convergence/equilibrium.

- Once equilibrium has been reached, compute and average the relevant observables (e.g. magnetization, energy) over a number of subsequent iterations.

The Metropolis-Hastings algorithm, while a good generalist method, is less suited for a system such as $RbCoCl_3$ since it focuses on a single spin at a time: as the system orders locally, the number of spins likely to flip decreases, slowing the process progressively.

In order to prevent the critical slowing down of the process, a number of cluster Monte Carlo algorithms have been developed. They rely not on flipping a single unit, but rather on clustering units and operating on them globally.

The Cluster Heat Bath (CHB) algorithm has been developed specifically for quasi-one dimensional Ising compounds [88, 89, 90]. In its essence, the CHB method does not focus on a single spin but instead rearranges simultaneously entire chains according to the Boltzmann distribution, Eq. 3.3.

At any step of the algorithm, one entire chain of the sample is considered. Its configuration is determined using the probability functions that the j-th spin is pointing upwards or downwards, $p(S_j^z = \uparrow)$ and $p(S_j^z = \downarrow)$. The staggered field is h_j.

This algorithm will be first sketched for a single chain to simplify the notation. For the first spin in the chain:

$$p(S_1^z = \uparrow) = \frac{e^{-\beta h_1}}{\mathcal{Z}_1},$$
$$p(S_1^z = \downarrow) = \frac{e^{+\beta h_1}}{\mathcal{Z}_1}, \tag{3.25}$$

where $\mathcal{Z}_1$ is a normalization factor to ensure that the total probability is 1 – i.e. $\mathcal{Z}_1 = \exp(-\beta h_1) + \exp(+\beta h_1)$, the partition function for a one-spin system. A positive (negative) value for h_1, i.e. most neighbouring spins pointing upwards (downwards), favours the probability that the spin points downwards (upwards), enforcing the AF order in the chain. Note that this criterion is for now equivalent to the Metropolis-Hastings approach.

Then, for any further spin along the chain, the probabilities are treated as conditional: the question is the probability of the spin j being up or down given the probabilities for the site j-1 and given the staggered field. This can be expressed symbolically as:

$$p(S_j^z = \uparrow) = \Big(p(S_{j-1}^z = \uparrow)\, p(S_j^z = \uparrow | S_{j-1}^z = \uparrow) + ... \\ p(S_{j-1}^z = \downarrow)\, p(S_j^z = \uparrow | S_{j-1}^z = \downarrow) \Big)\, p(S_j^z = \uparrow | h_j), \tag{3.26}$$

where the conditioned probabilities can be easily calculated and the probabilities of the j-1-th spin are known iteratively:

$$p(S_j^z = \uparrow) = \Big(p(S_{j-1}^z = \uparrow)\, e^{-2\beta J} + ... \\ p(S_{j-1}^z = \downarrow)\, e^{+2\beta J} \Big) \frac{e^{-\beta h_j}}{\mathcal{Z}_j},$$
$$p(S_j^z = \downarrow) = \Big(p(S_{j-1}^z = \uparrow)\, e^{2\beta J} + ... \\ p(S_{j-1}^z = \downarrow)\, e^{-2\beta J} \Big) \frac{e^{+\beta h_j}}{\mathcal{Z}_j}. \tag{3.27}$$

Simplifying the notation, in general it is written that:

$$p(S_j^z) = \frac{1}{\mathcal{Z}_j} \sum_{S_{j-1}^z=\uparrow,\downarrow} p(S_{j-1}^z)\, e^{-2\beta J S_{j-1}^z S_j^z - \beta h_j S_j^z}. \tag{3.28}$$

The probabillity of a specific sequence $\{S^z\}$ can be then, according to [88, 89, 90], be computed as:

$$\begin{aligned} p(\{S^z\}) &= \prod_j \frac{p(S_j^z)}{\mathcal{Z}_j} = ... \\ &= (\prod_j \frac{1}{\mathcal{Z}_j}) \exp\big(-2\beta J \sum_{j=1}^{N-1} S_j^z S_{j+1}^z - \beta \sum_{j=1}^{N} h_j S_j^z \big) = ... \\ &= \frac{e^{\beta \mathcal{H}_{\text{Ising}}(\{S^z\}))}}{\mathcal{Z}}. \end{aligned} \tag{3.29}$$

This proves that the probabilities behave according to Boltzmann statistics: the clusters (i.e. chains) are generated in thermal equilibrium with the heat bath of their surroundings.

The algorithm works as follows:

- Randomly create an initial set of spins of a certain size.
- Randomly pick one chain of spins. Compute the staggered field h_j and the probabilities $p(S_j^z)$ for each spin of the chain.
- Rearrange the chain according to $p(S_j^z)$: if $p(S_j^z = \uparrow) > c$, where $c \in [0,1]$ is a random number, then $S_j^z = \uparrow$.
- Pick a new spin and repeat until convergence/equilibrium.
- Once equilibrium has been reached, compute and average the relevant observables over a number of subsequent iterations.

This method has been proven to reproduce closely the magnetic phase transitions of $CsCoBr_3$ and $CsCoCl_3$ [90]. Its applications are, however, very general, and CHB simulations have been performed e.g. to demonstrate a

glass phase transition in a 2D random Ising model or to show the ferromagnetic transition in $SrTiO_3$.

The application in $RbCoCl_3$ is straightforward. The two interactions in the plane can be included to compute h_j, while including a next-nearest neighbour interaction along the chain (associated to an exchange parameter J_2) requires a slight extension of Eq. 3.28:

$$\begin{aligned}
p(S_1^z) &= \frac{1}{\mathcal{Z}_1} e^{-\beta h_j S_1^z}, \\
p(S_2^z) &= \frac{1}{\mathcal{Z}_2} \sum_{S_1^z} p(S_1^z)\ e^{-2\beta J_1 S_1^z S_2^z - \beta h_j S_2^z}, \\
p(S_j^z) &= \frac{1}{\mathcal{Z}_j} \sum_{S_{j-2}^z} \sum_{S_{j-1}^z} p(S_{j-2}^z) p(S_{j-1}^z)\ e^{-2\beta J_1 S_{j-1}^z S_j^z - 2\beta J_2 S_{j-2}^z S_j^z - \beta h_j S_j^z}. \quad (3.30)
\end{aligned}$$

I will here further propose one expansion of this method in the following section.

Extension of the CHB method to the order in the plane

This method can be generalized to order the planes faster by increasing the size of clusters – considering sequences of chains instead of single chains.

The planar CHB (pCHB) method used for this study can be formulated as follows:

- Randomly create an initial set of spins of a certain size.
- Randomly select a path $\gamma = \{(x_k, y_k)\}_{k \in I}$, I being an index set. The coordinates (x_k, y_k) reference a specific chain of spins, i.e. a set $(S_{j,k}^z)$. The following list of conditions has been used through this study:
  - γ defines a connected path between an initial spin (x_1, y_1) and a final spin (x_n, y_n).
  - The path doesn't loop on itself.
  - The path can be of any length.
  - Periodic boundary conditions are imposed.

An exemplary sketch of a path is sketched in Fig. 3.28.

- For each spin in γ the probability $p(S^z_{j,k})$ is calculated iteratively and conditionally. Importantly enough, the probabilities of $p(S^z_{j,k+1})$ do not influence $p(S^z_{j,k})$ in the same way that $p(S^z_{k,j})$ doesn't depend on $p(S^z_{j+1,k})$. This allows for a faster exit from local minima.
- Rearrange the spins in γ according to $p(S^z_{j,k})$.
- Repeat from 2 until convergence/equilibrium.
- Once equilibrium has been reached, compute and average the relevant observables over a number of subsequent iterations.

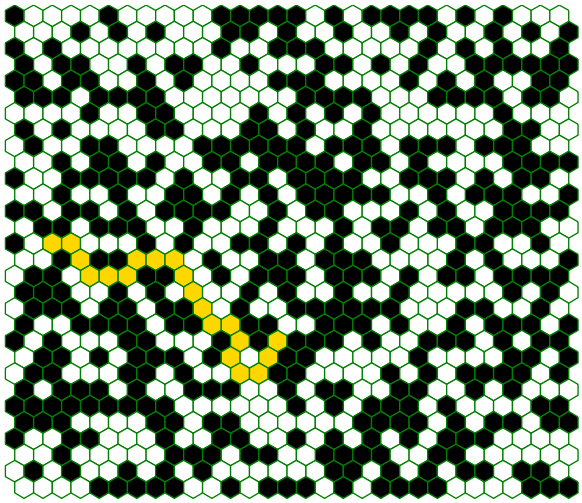

Figure 3.28: Sketch of a possible situation in the planar CHB method. A single plane of a set of random spins are generated (black and white), and a path γ (yellow) is chosen. The spins are to be rearranged as to being in thermal equilibrium with their heat bath.

Similarly to the conventional CHB method, the rearranged spins satisfy Boltzmann statistics by construction. Simultaneously flipping large amount

of spins allows to propagate changes in the spin structure faster than the Metropolis-Hastings method – hence improving performance.

3.7 Comparison between the CHB method and the fits

CHB simulations were performed on a 120x120x5000 spin lattice, running over 8000 cycles. During even-numbered cycles a random[10] number of conventional CHB operations took place (i.e. chains were flipped individually), while the odd-numbered cycles consisted in a single pCHB loop (reordering, however, a random number of chains). Additionally the temperature of the system was lowered during the 8000 cycles (similarly to simulated annealing).

The fitted interaction constants $J_{1,2,nn}$ were used for this simulation. In the absence of a better approximation it was furthermore assumed that $J_{nnn} = J_{nn}/10$.

Table 3.5 shows comparisons between fit results and CHB calculations. It has to be noted that the CHB calculations were not set to stabilize the temperature, but rather to obtain the best fit to the experimental population factors (i.e. the temperature of the simulations is not necessarily 4 and 18 K).

The spin configurations are then visualized allowing a direct comparison. For the visualization in Fig. (3.29-3.30), what is shown is not a single plane but a 2D collapsed schematic view: a single chain $\{S_j^z\}$ is used to compute the sum $\sum_j (-1)^j S_j^z$, which is ± 1 for fully ordered chains, and between these extremes for partially disordered chains.

Furthermore the spin structure can be Fourier-transformed along the (H H 1) to simulate the Bragg scattering from the magnetic lattice, as in Fig. 3.5. A full simulation of the diffraction data is not within the scope of the present study, and thus no other terms and corrections (e.g. the magnetic

[10] Less than 120.

T [K]	I_0^{fit}	I_0^{CHB}	I_2^{fit}	I_2^{CHB}	I_4^{fit}	I_4^{CHB}	I_6^{fit}	I_6^{CHB}
4	66(2)	61	3(1)	6	0(1)	5	30(1)	28
8.5	50(9)	51	16(3)	17	14(3)	14	18(3)	18
10.5	41(8)	40	25(5)	29	24(4)	19	9(2)	9
18	38(1)	35	34(1)	32	26(1)	18	0(1)	5
23	29(7)	35	48(9)	32	23(4)	18	0(1)	5

Table 3.5: Comparison between population factors (in percentage of the total scattering) as obtained in the fits and in the CHB algorithm for 4 and 18 K, as explained in the text. The CHB calculations for 18 K do not add up to 100% due to weight being allocated to negative staggered fields (which were neglected during the fits).

form factor) are included except for a convolution with a Gaussian profile to simulate the instrumental resolution.

The spin configuration obtained for 4 K displays large domains of honeycomb-ordered spins, in agreement with the known structure. The interfaces between domains have simple shapes (resembling straight lines) to minimize the geometrical frustration. Most of the chains are fully ordered. The Fourier transform of this spin structure is dominated by a peak at (2/3 2/3 1), with a peak at (1 1 1) roughly one order of magnitude less intense. This is in excellent agreement with the behaviour described in the introduction to this chapter.

The spin configuration for 18 K lacks the large domains that characterise the 4 K structure, but does retain meaningful local honeycomb order. Moreover the number of domain walls inside the chains has increased to a very relevant amount. At this temperature the AF *nn* in-plane interaction is still relevant, creating a situation where spins in the plane prefer to be antiparallel, but the FM *nnn* in-plane interaction that stabilises the long-range hexagonal order is no longer relevant compared to thermal disorder.

Fig. 3.31 shows the simulated Bragg diffractions from the spin structures

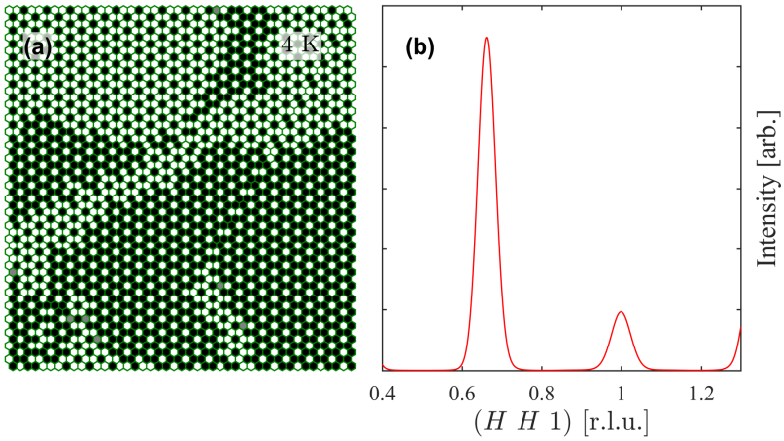

Figure 3.29: (a) Schematic view of a section of the Monte Carlo simulation of $RbCoCl_3$ for 4 K as discussed in the text. Black and white hexagons are ordered chains of opposite orientations, while grey hexagons are disordered chains. There are wide domains of honeycomb-ordered spins with mostly-straight "well-behaved" domain walls. This phase is ordered. (b) Simulation of the Bragg diffraction from the spin structure for 4 K. Peaks can be found at (2/3 2/3 1) and (1 1 1) with an order of magnitude of difference in their intensity, in satisfactory agreement with the experimental data, see Fig. 3.5.

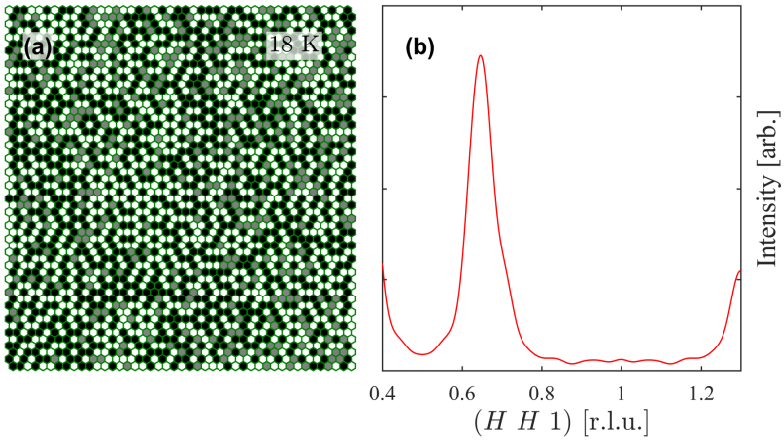

Figure 3.30: (a) Schematic view of a section of the Monte Carlo simulation of $RbCoCl_3$ for 18 K. There are no long-range domains to be found, but the structure displays considerable local ordering. We propose this structure as a more physical generalization of the simplistic PDAF structure as explained in literature. (b) Simulation of the Bragg diffraction from the spin structure at 18 K. A peak can be found at (2/3 2/3 1) while there is none at (1 1 1); additionally the tails of the peaks are much broader – a result compatible with the rise of the diffuse scattering, see Figs. (3.5-3.6).

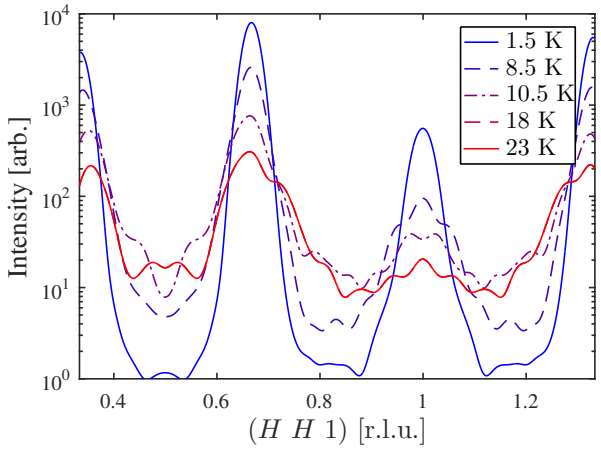

Figure 3.31: Simulation of the Bragg diffraction from the calculated spin structures at all experimental temperatures except 35 K along the $(H\ H\ 1)$ direction. The magnetic structure peaks are sharp at the lowest temperatures and become broader and less intense as the temperature increases.

at all temperatures. In good agreement with the experimental diffraction data presented in the beginning of the chapter, the magnetic peaks are sharper at lower temperatures and broader at higher temperatures, and their intensity decreases with temperature. Simultaneously, the scattered intensity at $\vec{Q}$-points outside of the peaks increases, which is an indication of the diffuse scattering emerging around the peaks. At this stage the resulting scattered patterns still show many computational artifacts (e.g. not many peaks are close to be Gaussians, or Lorentzians), but this is due to the insufficient size along x and y of the simulated spin array, which is a computational constrain. However, even at this stage the calculation confirms some important experimental observations on $RbCoCl_3$: namely, the transition from a more ordered to a more disordered spin structure is associated to the weakening of sharp Bragg peaks and the emergence of diffuse scattering around them.

It has to be reiterated that this is calculated entirely from the population factors (themselves a result of the fitting of the spectrum) and the spin Hamiltonian, without any information about the experimental Bragg

diffraction being required or considered.

The agreement between fitted and simulated population factors is satisfying but not perfect: for instance with the CHB predicting 5 % occupation for I_6 for 18 K when the fit does not allocate any weight to that component. There are however a number of physical considerations that haven't been included in the Monte Carlo calculation, such as imperfections in the lattice which can lead to pinning.

Finally, the CHB simulation did not give any comparably accurate result for 35 K. We interpret this as an indication that the population factors above T_{N1} are not deduced from a static structure – which does not exhibit any sort of detectable order – but rather from dynamic considerations, i.e. the staggered field on a chain is no longer the sum of the interactions with the neighbouring chains but also the time average: since at that temperature there are abundant thermally-excited solitons (which flip spins when propagating) the time-average drives the staggered fields towards zero.

3.8 Further aspects of the spectrum

3.8.1 The Villain mode

While the gapped excitations between 10 and 20 meV are the result of scattering on an ordered chain, it is possible to scatter on a domain wall as well. This excitation is, thus, intrinsically gapped, and is called a Villain mode [49].

The Villain mode is theoretically predicted to be centred on $L = \pm 1$, being otherwise H- and K-independent, and its intensity scales with the Bose-Einstein factor $n(\hbar\omega, T)$.

Usually ToF instruments have intense elastic lines, owing to the elastic and incoherent scattering on components such as the cryostat[11], which is a problem to detect a gapless mode. However, by modelling the signal at

[11] A conventional way to reduce these contributions would be via the use of a radial collimator; however LET is not provided with one at this point in time.

temperature T – $S(\vec{Q},\hbar\omega)_T$ – as the sum of a temperature-independent part $A(\vec{Q})$ and a temperature-dependent part $B(\vec{Q},T)$, it is true that

$$S(\vec{Q},\hbar\omega)_{T_2} - S(\vec{Q},\hbar\omega)_{T_1} = V(\vec{Q},T_2) - V(\vec{Q},T_1)$$

and by assuming that $B(\vec{Q},T_1) = n(\hbar\omega,T)V(\vec{Q})$ – i.e. the Villain spectrum does not evolve with temperature but is rather weighted by a conventional statistical distribution – then the Villain mode is found as

$$V(\vec{Q},\omega) = \frac{1}{n(\hbar\omega,T_2) - n(\hbar\omega,T_1)}\big(S(\vec{Q},\hbar\omega)_{T_2} - S(\vec{Q},\hbar\omega)_{T_1}\big).$$

Figure 3.32 shows the Villain mode for all high-statistics datasets. It follows the known expectations for such a mode. While a more in-depth look into its properties is not required in this present study, we note here that the mere presence of the Villain mode reinforces the position of $RbCoCl_3$ as an almost-ideal quasi-1D Ising-like chain.

3.8.2 Higher modes of the Zeeman ladder

At 4 K the presence of additional modes at a higher energy transfer is particularly apparent[12], see Fig. 3.22. These modes are particularly problematic as they are not explained by our fits: in Fig. 3.23(a) the presence of two Zeeman ladder higher modes, at about 15 meV and 17 meV, is highlighted – yet the fitted Hamiltonian only predicts one Zeeman ladder mode, at about 16 meV.

The difficulty lies firstly in the low statistical weight of these higher modes: the fitting procedure is sensitive exclusively to the continuum spectrum and to the first mode of the $h_{ic} = 6J_{nn}$ chain.

A way to circumvent this problem is to fit the modes to the energy of the modes (which can be accurately obtained by fitting 1D cuts with Gaussian

[12] At higher temperatures the Lorentzian broadening of the modes makes it impossible to distinguish them from the background.

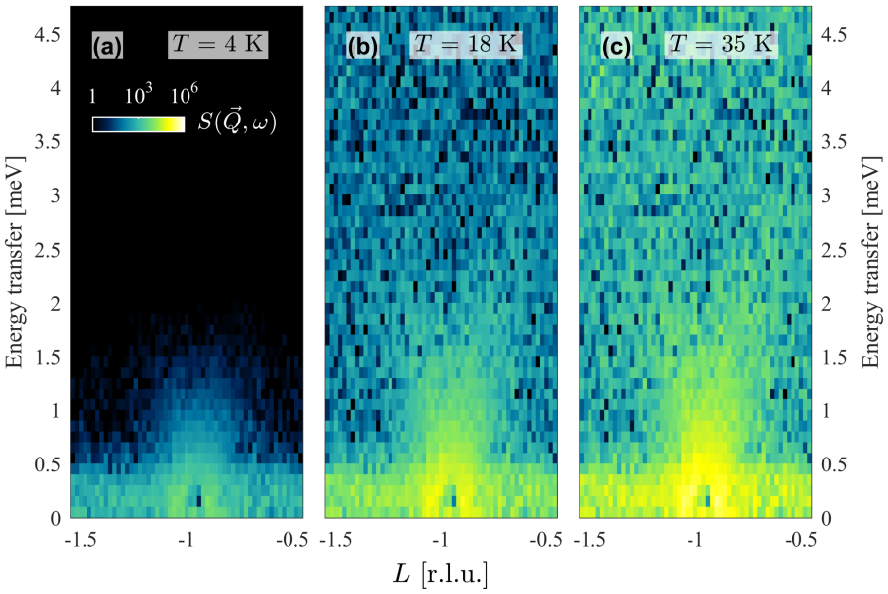

Figure 3.32: Villain mode at three temperatures. In general the mode can be characterised as being gapless and depending only on L, and is the result of scattering on domain walls.

functions). This approach neglects the intensity of the mode and cannot address issues such as the lineshape, but it is a useful exercise. Its results are displayed in Fig. 3.33.

The reader might be interested in some clarifications on the fitting procedure:

- During the fits either three or four curves will be considered. The first is not a mode but is rather the maximum of the continuum, while the other three are the first three modes of the Zeeman ladder belonging to $h_{ic} = 6J_{nn}$ chain.

- All exchange parameters can be fitted, although the first mode is assumed to have $h_{ic} = 0$. Figure 3.33(a) shows an unconstrained fit, while (b) shows a fit where J_1 was constrained to be equal to the previously fitted one.

A picture of the fits is presented in Fig. 3.33. Table 3.6 summarizes the

results.

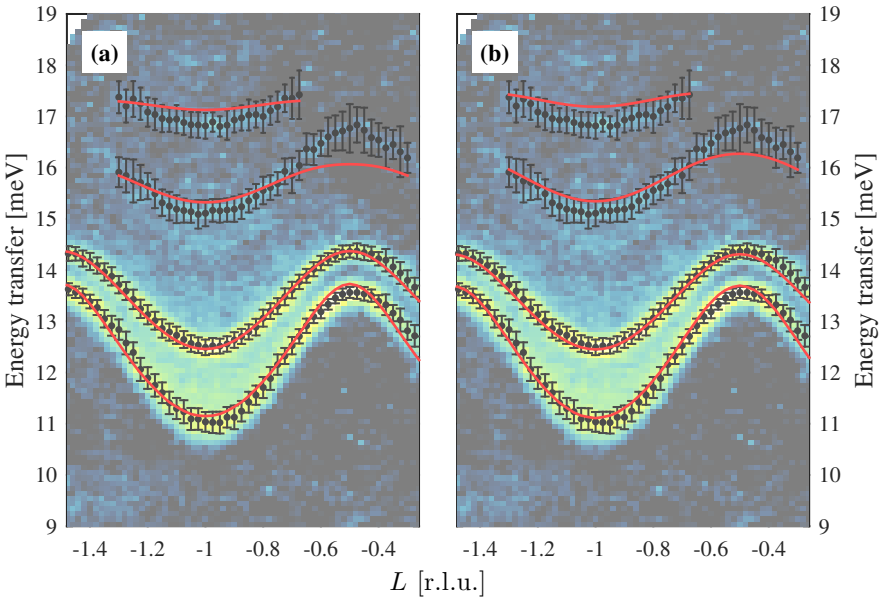

Figure 3.33: Fits of the modes. The energy of the maximum of the intensity of the continuum and the energies of the three visible steps of the Zeeman ladder (black data points) were fitted from the data (semitransparent colormap) and fitted to the model (red). (a) Fits with free parameters. (b) Fit with the constraint on J_1 to be as fitted previously.

It must be noted that even the fits that neglect the intensity fail to fully reproduce the higher excited states of the Zeeman ladder, seen between 15 and 18 meV in Fig. 3.33. However, this calculation is sufficient to get an approximate value for their average energy.

While it must be concluded that the Hamiltonian is missing terms necessary to describe the higher modes of the Zeeman ladder, it provides a satisfying explanation for the first, and most intense, mode.

3.8.3 Analysis according to Goff's Hamiltonian

All of the preceding results were obtained using F. Matsubara's model. A similar analysis can be carried through using J. Goff's Hamiltonian.

	J_1 [meV]	ϵ_1	J_2 [meV]	ϵ_2	$6J_{nn}$
Reference	5.889(1)	0.126(1)	0.518(1)	0.605(1)	0.77(1)
"Free"	6.00(8)	0.12(1)	0.48(5)	0.6(1)	0.63(4)
"Constrained"	5.889	0.135(9)	0.59(3)	0.45(7)	0.60(4)

Table 3.6: Comparison between the fitted parameters of the Hamiltonian as fitted previously ("reference"), freely fitted to the modes ("free"), or fitted with a fixed J_1 ("constrained").

	Present work	$CsCoCl_3$ [68]
J [meV]	6.79(1)	6.37
ϵ	0.17(1)	0.145
Δ [meV]	0.92(1)	0.70
J_{nn} [meV]	0.088(1)	0.05

Table 3.7: Comparison of the fitted parameters between the present work (first column) and J. Goff's analysis. The errors on these results are not available. For the values of ϵ, only the result at 4 K is presented.

A multifit was performed to a $\chi^2 = 2.21$. The exchange parameters are presented in Table 3.7, where they are compared to J. Goff's results for $CsCoCl_3$ for reference.

The values are found to be close to the results in literature, although with an unusually high value for ϵ. The fits are displayed in Fig. 3.34. While the agreement at higher temperatures is sufficient, this model fails to reproduce the dispersion at low temperature, specifically concerning the sharpness of the continuum, see panel 3.34(b), and the spacing between the modes, 3.34(c).

We propose, as one of the results of this study, that F. Matsubara's Hamiltonian, which has been used in all the previous part of the study, is the best suited to describe this class of compounds.

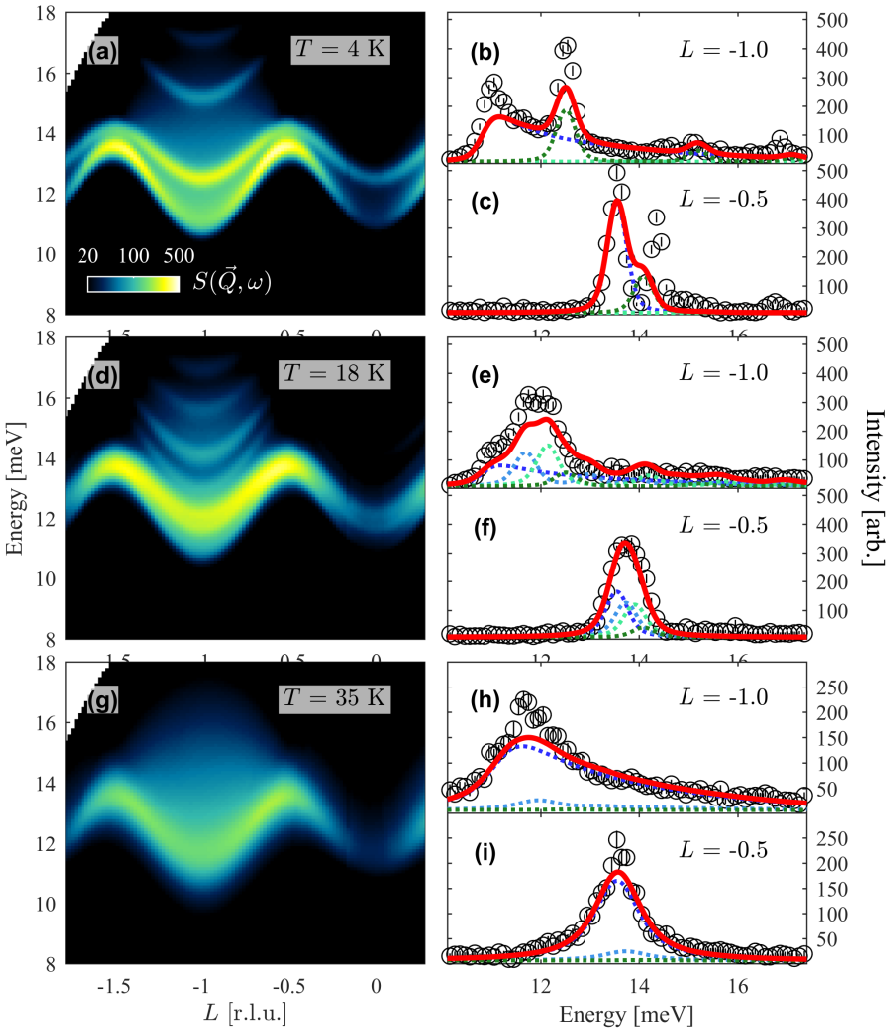

Figure 3.34: Results of the fitting procedure according to J. Goff's proposed Hamiltonian. All averaging intervals are the same as before, see Fig. 3.18-3.19. (a,d,g) Simulation of the fitted model at 4, 18 and 35 K. (b,c,e,f,h,i) Cuts at each temperature for L = -1.0 and -0.5 r.l.u.

3.8.4 Higher energy-transfer data

As mentioned in Section 3.4.3, an experiment on $RbCoCl_3$ was performed at LET in 2015. For this experiment we employed two of the three single crystals used in 2011.

While the focus was applying a magnetic field, improvements on the instrumental data collection procedure meant that multirep (see introduction) could be employed. This allowed to simultaneously measure at different incoming energies – specifically at $E_i = 88$ meV, offering an insight in the high-energy-transfer data of the spectrum of $RbCoCl_3$.

Figure 3.35 shows the data measured with $E_i = 88$ meV. A sharp mode appears at 40 meV: while to the best of our knowledge there is little literature on this topic, we suggest that it is a crystal field excitation, due to its extreme flatness[13] and their $\vec{Q}$-dependence: phonon intensities tend to increase with $\vec{Q}$, while magnetic or crystal field excitations tend to decrease in intensity (owing to the form factor of the orbital shells).

3.9 Conclusions and outlook

As the conclusion of this study we can summarise the results as follows.

- We have measured the soliton dispersion in $RbCoCl_3$ and explained it in terms of a simple, fundamental model (following Matsubara and Shiba's proposals).
- We have assessed that the dominant exchange parameter J_1 is 5.889(1) within the model. That is much bigger than those found in similar other chain compounds such as $CoNb_2O_6$ and $BaCo_2V_2O_8$, and the critical magnetic field required to trigger a quantum phase transition in $RbCoCl_3$ is beyond modern neutron scattering capability.

[13] Crystal fields excitations can be thought as almost perfectly localized in space. Their $\vec{Q}$-dependence is in first approximation negligible as the Fourier transform of a delta function is a constant.

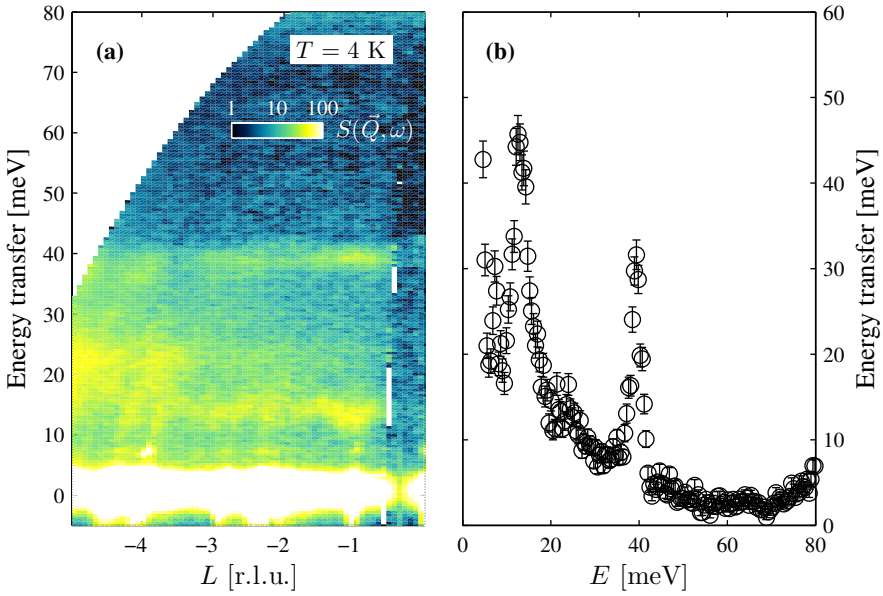

Figure 3.35: (a) Slice of the data collected at $E_i = 88$ meV, $T = 4$ K, and no magnetic field. The data was normalized to the proton current, meaning an overall scaling of the intensities compared to the previously shown data. Dominant features are the bright elastic line, the first modes of the soliton spectrum between 10 and 20 meV, and a further mode at ~ 40 meV. The data at $L < 3$ r.l.u. also shows heavy background contamination due to the cryostat and the magnet. (b) Cut of the data for -1.15 $< L <$ -0.85. The various branches of the soliton cannot be distinguished, and a resolution-sharp mode appears ~ 40 meV. It has to be noted that the shape of the background up to 50 meV could be due to the elastic line, while the increase of signal above 70 meV is due to the next pulse of the beam.

- We have shown that the one-dimensionality of the system is outstanding, with an Ising-like coefficient ϵ_1 of 0.15 (compared e.g. with 0.46 in $BaCo_2V_2O_8$). This solidifies the position of the $ACoX_3$ compounds as being amongst the closest realizations of spin chains in the Ising limit.

- We have explained the spectrum in terms of dispersions associated to staggered fields. A vanishing staggered field is associated to an Ishimura-Shiba-like continuum (which can display a bound mode, similarly to $CoNb_2O_6$), while non-vanishing staggered fields are associated with a series of bound modes called a Zeeman ladder. The simultaneous presence of a IS continuum and of a Zeeman ladder is due to the honeycomb geometry.

- We have traced the evolution of the spectrum as a function of temperature in all the magnetic regimes of the phase diagram of $RbCoCl_3$, in excellent agreement with several models for the structure. We have furthermore modelled the effects of temperature in terms of mobility and lifetime of the excitations, obtaining a self-consistent picture.

- We have furthermore explained the population factors associated to each staggered field not just qualitatively, but with a special Monte Carlo algorithm which we have developed for this purpose (pCHB) from an already specialized pre-existent algorithm (CHB). The agreement between our simulation and the fitted population factors is extremely encouraging.

We have no doubt that this understanding of the system is an important step forward in both the $ACoX_3$ compounds, but also Ising-like physics in general.

This study leaves some questions unanswered, and highlights several new aspects to be further investigated.

- The question of the quantum phase transition of $RbCoCl_3$, and its

excitations, are still open due to the magnitude of the gap, around 11 meV. We have to stress that, in order to answer these question in an INS experiment, significant technological advances have to be made.

- What is the full evolution versus temperature of the Ising-like anisotropy $\epsilon_1(T)$, of the Lorentzian width $\Gamma(T)$, and of the population factors? With at most three temperatures in any phase, our data are not sensitive enough to accurately explain the effects of thermal disorder, although it is more than sufficient to establish a trend. Part of this can be found in E. Hirtenlechner's thesis [41].

- Can the effect of temperature be modelled in more realistic terms? While the argument from mobility and lifetime is accurate within the goodness of the data, theoretical studies have presented more nuanced models. For instance, some authors [75] have presented results that are compatible with a decrease in ϵ_1, but have also introduced an asymmetric and more complicated linewidth, while our data were analysed on the assumption of a simple Lorentzian widening.

- What is the value of J_{nnn}? A ferromagnetic next-nearest neighbour interaction is necessary in order to lift the frustration and enforce the honeycomb order, but its value is less than the instrumental resolution. Further studies are needed to shed light on this issue.

- How can the higher modes of the Zeeman ladder be explained? While the most intense modes of the fits at all temperatures are satisfyingly explained, the modes that can be measured between 15.5 and 18 meV are as of now not modelled correctly. We hope that this study will motivate interest from the theoretical community on this particular issue.

A new set of experiments would be needed to address these questions. On one hand measurements of the full $\vec{Q}$-dependence of the diffuse scattering (for instance on an instrument like WISH, at ISIS) would allow to test the

CHB model as a function of temperature and obtain a good understanding of the evolution of the local staggered field. Alternatively, depending on the crystallographic location where they stop, muons might be used to determine the number, value and prevalence of staggered fields in the compound at any given temperature.

Chapter 4

The spin-wave spectrum of the magnon Hall pyrochlore $Lu_2V_2O_7$

4.1 Scientific background

In the cubic pyrochlore lattice, ions can form vertex-sharing tetrahedra: in such configuration each ions has six equidistant neighbours, or three in each tetrahedra (see Fig. 4.1). Due to its unique geometry, this structure allows for high frustration depending on the nature of the magnetic interactions and the spin symmetry. A variety of interesting phenomena have been reported when the magnetic sites are decorated with "classical" spins (large S) [91].

The most famous example is the spin-ice behaviour, first reported in $Ho_2Ti_2O_7$, which emerges from Ising spins and leads to the description of magnetic monopoles [25, 92, 93, 94, 95, 96, 97, 98, 99]. Amongst other noteworthy properties are the spin-liquid ground state [24, 100, 101], spin-glass behaviour [102], order-by-disorder transitions [103, 104, 105], giant or colossal magnetoresistance [106, 107], superconductivity [108] and more subtle effects such as the spin-driven Jahn-Teller distortion [109].

The class of $RE_2V_2O_7$ (Re = Lu, Yb, Tm), which will be described in more detail later, are insulating Heisenberg ferromagnets (FM) [110] that exhibit several remarkable properties, such as large negative magnetoresistance [111, 112, 113] and orbital ordering [114, 115, 116, 117]. These compounds received wide attention with the discovery of the thermal magnon Hall effect

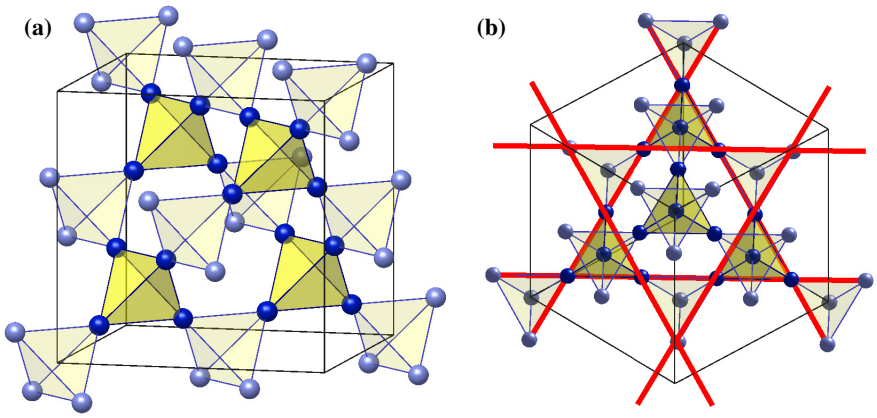

Figure 4.1: View of the magnetic sites in the unit cell of $Lu_2V_2O_7$. There are 16 V^{4+} (dark blue) ions per unit cell (black lines) forming four tetrahedra (yellow faces). Each ion lies in the vertex of two tetrahedra. (a) View from the side. (b) View along the [1 1 1] direction. In this projection, a single plane of magnetic ions has the structure of a Kagome lattice (red lines).

[118, 119, 120, 121, 122, 123].

There are several generalizations of the Hall effect. A multitude of particles, or quasi-particles, and potentials can be involved in a Hall effect equivalent. Notably a *thermal* Hall effect involves the application of a temperature gradient to induce a heat current – and the carriers can be, for example, both electrons or phonons [124, 125, 126, 127]. In conductors this effect is also called the Righi-Leduc effect [128]. In general this is also related to several thermoelectric effects that couple a temperture gradient to a voltage, such as the Seeback, Peltier and Thompson effects.

In the thermal magnon Hall effect, a temperature gradient is applied on the material (typically thin-film like). Since the $RE_2V_2O_7$ compounds are insulating (i.e. electrons are not a convenient carrier due to low mobility), it is quasi-particles such as phonons and magnons that carry the thermal current across the temperature gradient, and it is found that an external magnetic field will cause a transverse thermal response (i.e. one "side" gets warmer than the other). Furthermore once the phonon contribution

to the thermal conductivity has been subtracted, the dependence on the magnetic field of the thermal magnon conductivity shows a remarkable if not unexpected behaviour, shown in Fig. 4.2 [118].

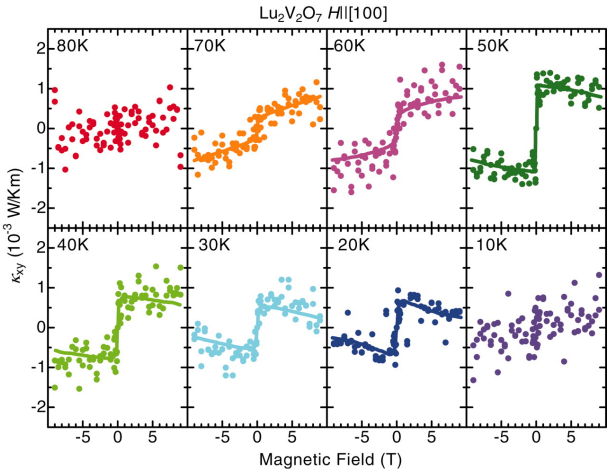

Figure 4.2: The thermal magnon Hall conductivity κ_{xy} as a function of temperature and magnetic field, figure from reference [118]. The solid lines are fits to the model propose by Onose *et al.*

Magnons are electrically neutral and thus unaffected by the Lorentz force, which stimulated theoretical research in order to determine how a magnetic field can modify their path. The conventional explanation for this phenomenon relies on the Dzyaloshinsky-Moriya interaction (DMI) [10, 11], which is present due to the centre of the V-V bonds not being a point of inversion symmetry. For reasons that will be discussed later, the DMI enters the magnon dispersion via its projection to the external magnetic field [118], and thus the magnetic field – by changing the energy of the magnon – effectively forces all magnons to turn in one sense (an "upwards" magnetic field will force the magnons to travel clockwise or anticlockwise depending on the direction of the DMI). Heat will be released on the side the magnons travel through, creating an imbalance with the side that few magnons reach.

To summarize the analogy between the conventional Hall effect and the thermal magnon Hall effect, the temperature takes the place of the electric

potential (used to move the particles from one side to the other) and the DMI substitutes the magnetic field as a vector potential (inducing a statistical drift perpendicular to the current direction).

While this explanation is broadly agreed upon, there have been several competing theoretically formulations. The transverse thermal magnon conductivity can be shown to depend on the ratio between the DMI parameter D and the FM exchange parameter J. However proposed ratios for D/J have been diverse for $Lu_2V_2O_7$. The original study suggested an unusually high value 1/3 [118], while a study based on a DFT calculation proposed 1/20 [113]. A more recent fit of the data suggested 1/200, although this calculation assumed a 2D Kagome geometry and not a 3D pyrochlore structure [121]. Without direct measurements of the DMI, the suggested values for D/J span two orders of magnitude.

Another recently discussed property of $Lu_2V_2O_7$, and in general of materials that display the thermal Hall effect, is a *topological magnon insulator* behaviour: in analogy to conventional topological insulators, edge magnons have non-trivial topological properties that are determined by the bulk [129, 121, 122, 130]. While a discussion of this effect is beyond the scope of this thesis, it potentially allows for the realization of magnon wave guides at the interface between magnon Hall insulators whose Dzyaloshinsky-Moriya constants differ in sign [123].

The disagreement around the value of D/J gives us a prime reason to investigate this compound in an inelastic neutron scattering experiment in order to directly measure the magnon dispersion and determine the spin Hamiltonian. In this chapter I present the results of one experiment on this compound that I performed, and my subsequent analysis, which required a full simulation of the inelastic cross section and a rebinning procedure we devised to maximize the signal to noise ratio.

4.2 Introduction to $Lu_2V_2O_7$

All of the rare-earth compounds $RE_2V_2O_7$ (Re = Lu, Yb, Tm) are cubic pyrochlores that crystallise in the $Fd\bar{3}m$ space group ($a = b = c = 9.9366$ Å for $Lu_2V_2O_7$) [131, 132, 133]. In this structure, both the rare earth and the vanadium sites build a network of vertex-sharing tetrahedra, as sketched in Fig. 4.1.

Magnetically, all of these compounds are described as Mott-insulating ferromagnets with a Curie temperature $T_C \sim 70$ K. In $Lu_2V_2O_7$ the V^{4+} ions are the only to carry an unpaired electron, resulting in a system of spin 1/2 sites (small S). A summary of its magnetic properties is presented in Fig. 4.3.

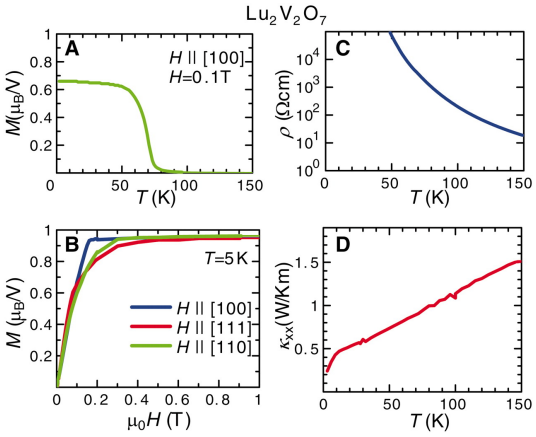

Figure 4.3: Summary of the magnetic properties of $Lu_2V_2O_7$, taken from [118]. (a) Magnetization as a function of temperature, showing a FM phase transition around 70 K. (b) Magnetization as a function of external magnetic field, showing the required fields to fully saturate the sample in any direction. This quasi-isotropic behaviour is typical of soft magnets. (c) Electrical resistivity, showing a typical insulating behaviour. (d) Parallel thermal conductivity as a function of temperature.

4.2.1 The Hamiltonian of $Lu_2V_2O_7$

During the studies of the magnon Hall effect, several Hamiltonians have been considered. In the original paper on this topic, Onose *et al.* considered a minimal Hamiltonian containing only a FM nearest-neighbour direct exchange, of magnitude J, a Dzyaloshinskii-Moriya term $\vec{D}_{jk}$, and a Zeeman term:

$$\mathcal{H} = -J\sum_{j,k}\vec{S}_j\cdot\vec{S}_k - \sum_{j,k}\vec{D}_{j,k}\cdot\big(\vec{S}_j\wedge\vec{S}_k\big) - g\mu_B\vec{H}\cdot\big(\sum_j\vec{S}_j\big). \tag{4.1}$$

Constraints for $\vec{D}_{j,k}$ can be obtained by applying the symmetry rules of Moriya [11]. Namely, labelling the four spins in a tetrahedra from 1 to 4, the vector $\vec{D}_{1,2}$ connecting the site 1 and 2 is parallel to the direction vector that spatially connects the site 3 and the site 4. In other words, the DMI vector between two sites on a side in a tetrahedron is parallel to the opposed side. By symmetry the DMI magnitude is a constant D, and the sign is constrained to two global choices (i.e. one can flip all the directions of the DMI, which is also equivalent to inverting the sign of D): however (as will be explained later) our inelastic neutron scattering experiment is unable to distinguish them. For simplicity we have chosen $D > 0$. It can be simply verified that $\vec{D}_{j,k} = -\vec{D}_{k,j}$, as required by Moriya's rules.

Hamiltonian 4.1 can be simplified using the Holstein-Primakoff transformation [134], i.e. expressing it in terms of a basis of bosons:

$$\mathcal{H}(\vec{Q}) = g\mu_B H + 2SJ\cdot(3-\Lambda(\vec{Q})), \tag{4.2}$$

where

$$\Lambda(\vec{Q}) = \begin{pmatrix} 0 & M_{1,2}\cos(K-L) & M_{1,3}\cos(H+K) & M_{1,4}\cos(L-H) \\ M_{2,1}\cos(K-L) & 0 & M_{2,3}\cos(H+K) & M_{2,4}\cos(H-K) \\ M_{3,1}\cos(H+K) & M_{3,2}\cos(H+Z) & 0 & M_{3,4}\cos(K+L) \\ M_{4,1}\cos(L-H) & M_{4,2}\cos(H-K) & M_{4,3}\cos(K+L) & 0 \end{pmatrix} \tag{4.3}$$

with $M_{j,k} = 1 - i\,\vec{D}_{j,k} \cdot \hat{n}/J$, and $\hat{n} = \vec{H}/|\vec{H}|$. This means that the direction of the magnetic field modifies the dispersion via a projection on $\vec{D}_{j,k}$.

The dispersion is sketched in Fig. 4.4. In general there are four modes, which for $D = 0$ can be described as a gapless acoustic mode between 0 and $2J$, an optical mode between $2J$ and $4J$, and a doubly-degenerate flat mode at $4J$. The introduction of the DMI term splits the modes even further, with particularly visible effects at the zone center Γ, at some points of the zone boundary (e.g. W) and at an energy of $4J$.

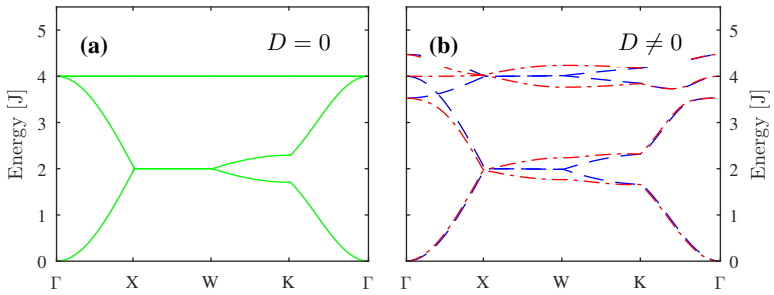

Figure 4.4: Magnon dispersion of $Lu_2V_2O_7$ following Eq. 4.1 for D zero and non-zero. Γ, X, W and K are conventional notations for the reciprocal space of a face-centred cubic symmetry. (a) Dispersion of the simple ferromagnetic pyrochlore. There are four modes (owing to the fact that there are four spins per tetrahedron), resulting in an acoustic mode between 0 and $2J$, an optical mode between $2J$ and $4J$, and a doubly-degenerate flat mode at $4J$. (b) Dispersion in the case of $D/J = 1/3$, for $\vec{H}$ parallel to (1 0 0), in blue, or (0 1 0), in red. The DMI lifts the degeneracy in a way that depends on the direction of the external magnetic field.

While this is the theoretical treatment used by Onose *et al.* in their original study of the magnon Hall effect, this Hamiltonian lacks any single-ion anisotropy. Such terms are however very relevant in several pyrochlores, leading e.g. to the Ising-like spins that are necessary for spin-ice behaviour.

Xiang *et al.* [113] performed a calculation based on density-functional

theory plus on-site repulsion (DFT+U) and obtained an Hamiltonian with an additional anisotropy term $A\sum(\vec{S}_j \cdot \vec{z}'_j)^2$, with the vector $\vec{z}'_j$ pointing along the local threefold symmetry axis (i.e. pointing to the "centre" of the tetrahedra). This calculation found J = 7.09, D = 0.048 and A = -3.64 meV, with a ratio $|D/J| \approx 0.048$, one order of magnitude below the original result.

In the same publication however the author renormalized the single-ion anisotropy term, merging it into the DMI term with a renormalized coupling D^{eff} which depends on the spin configuration but can be as large as 1 meV. If the second-order terms in the renormalized Hamiltonian are small enough, it might be impossible to identify the terms via a measure of the spectrum. Our study, while not sensitive to "bare" couplings, is crucial in order to find deviations from the spectrum predicted by Hamiltonian 4.1.

4.3 Experimental work on $Lu_2V_2O_7$

In order to determine the values of D and J, as well as the overall accuracy of the Hamiltonian, we have performed an inelastic neutron scattering experiment on Merlin (ISIS, RAL, UK) in Autumn 2011.

Two high-quality single crystals, with a total mass of 3.6 g, were co-aligned with (HHL) in the horizontal plane and cooled to base temperature, 4 K, without a magnetic field. Data were collected for incoming energies (E_i) of 25, 50 and 80 meV with an instrumental resolution (FWHM) of 3.0, 5.3 and 7.2 meV, respectively, at the elastic line. Typical measurement times were approximatively 16 hours.

The data were normalized with respect to a vanadium standard and were corrected for detector efficiency and outcoming versus incoming wavevector ratio k_f/k_i using the program MANTID [45, 46], expressing the data in absolute units. The resulting $S(\vec{Q}, \omega)$ datasets were analysed with the HORACE [47] software package. The data will be presented in the next section.

4.3.1 Overview of the data

Figures 4.5-4.7 show slices from the data sets with $E_i = 25$ meV to 80 meV. At this point of the study, the following statements can be made:

- The magnon dispersion has been measured and is well-defined. At low energy transfer, e.g. Fig. 4.5(b), the spin waves are almost perfectly Q^2-dependent, see Fig. 4.4. Around 15 meV the structure of the cubic zone boundary can be observed. The magnon between 30 and 35 meV of energy transfer is observed as mostly flat, despite still having a significant structure in its spectral weight.

- At low energy transfers (below roughly 15 meV) the magnon can be observed dispersing only from the allowed zone centres of a FCC cube - e.g. (1 1 1) and (2 2 2), but not (1 0 1). At higher energy transfers, this becomes less clear.

- A set of features can be observed with $E_i = 80$ meV at an energy of 20 meV and at $|\vec{Q}| \approx 4$ r.l.u. and, due to their distinct spherical symmetry, are unlikely to come from a single crystal. They can be thus identified as aluminium phonons.

Local magnetic field

As explained in section 4.2.1, the effect of the DMI depends on the direction of the local magnetic field. For instance, the degeneracy is lifted in W for $\vec{H} = [1\ 0\ 0]$, where a maximal splitting is observed, but not for $\vec{H} = [0\ 1\ 0]$, where no splitting can be found.

This is experimentally a problem, since we did not apply an external magnetic field (in order to maximize the coverage in $\vec{Q}$). As a consequence, the sample is divided into domains, and thus the observed spectrum is a superposition of all local spectra: in other words, we do not expect splitting of the modes but rather broadening of the lineshapes.

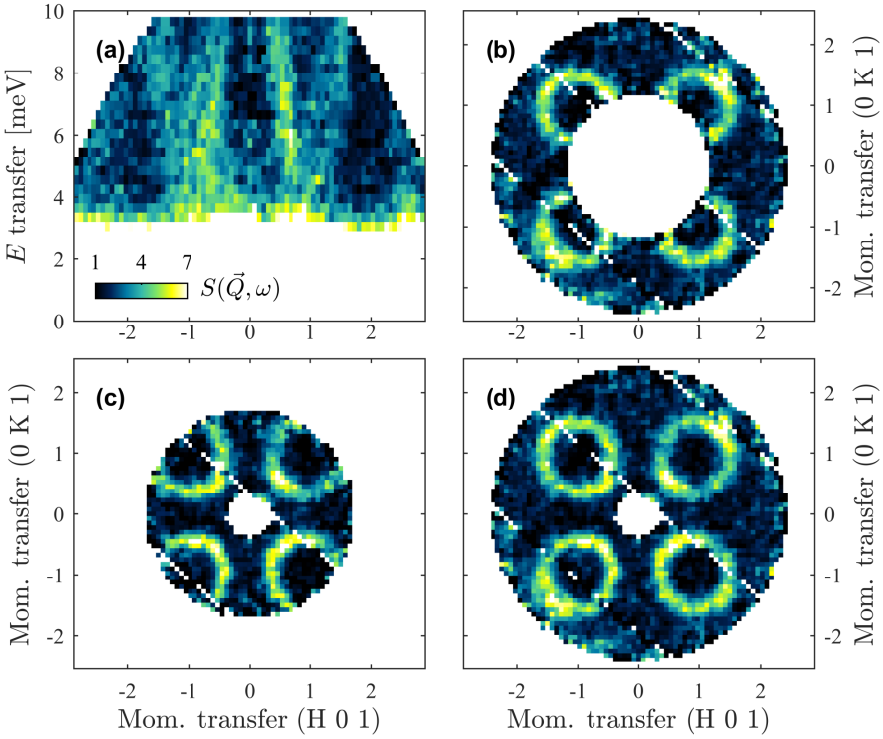

Figure 4.5: Magnon dispersion of $Lu_2V_2O_7$ at 4 K measured with $E_i = 25$ meV. (a) Momentum transfer H versus energy transfer, averaged for -0.8 $< K <$ -0.2 and $0 < L < 1.5$. An intense elastic line extends up to 3.5 meV, above which two magnons centred at $H = \pm 1$ can be identified. Due to the elastic line, it is not possible to tell whether the magnons are gapless or gapped. (b) Slice of the data averaged for $0.9 < L < 1.1$ and $4 < E < 6.5$ meV. The data for an energy transfer of 4 meV lie on the outside, while the data for an energy transfer of 6.5 meV lie on the inside. Four ring-shaped magnons can be seen, centred at the equivalent Γ-points (±1 ±1 1). (c) Slice of the data averaged for $0.9 < L < 1.1$ and $6.5 < E < 9$ meV. (d) Slice of the data averaged for $0.9 < L < 1.1$ and $4 < E < 9$ meV. This slice, which will be used as a reference later, is an average over the whole energy range of (c) and (d).

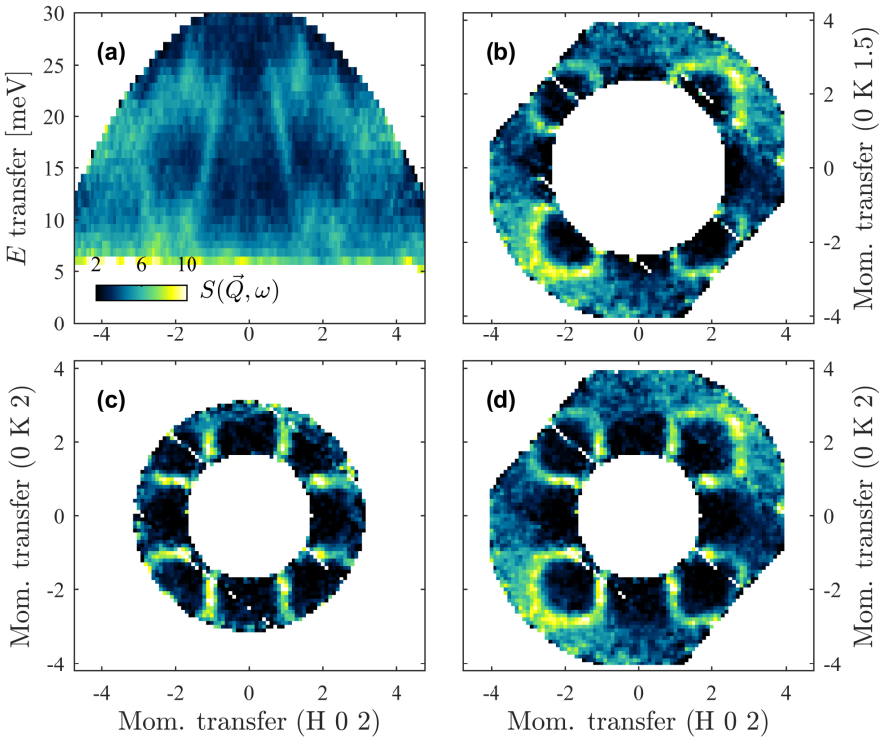

Figure 4.6: Magnon dispersion of $Lu_2V_2O_7$ at 4 K measured with $E_i = 50$ meV. (a) Slice of the data averaged for -5 $< K <$ 5 and 0 $< L <$ 3. At low energy transfers there are conical dispersive modes which extend all the way to 15 meV energy transfer. (b) Slice of the data averaged for 1.8 $< L <$ 2.2 and 10 $< E <$ 16 meV. At this energy transfer, the magnetic signal is still ring-like and centred around ($\pm$2 $\pm$2 2). (c) Slice of the data averaged for 1.8 $< L <$ 2.2 and 16 $< E <$ 18 meV. At this energy transfer the shape of the dispersion resembles straight lines, indicating that this is the typical energy of the magnon at the zone boundary. (d) Slice of the data averaged for 0.8 $< L <$ 1.2 and 10 $< E <$ 18 meV meV.

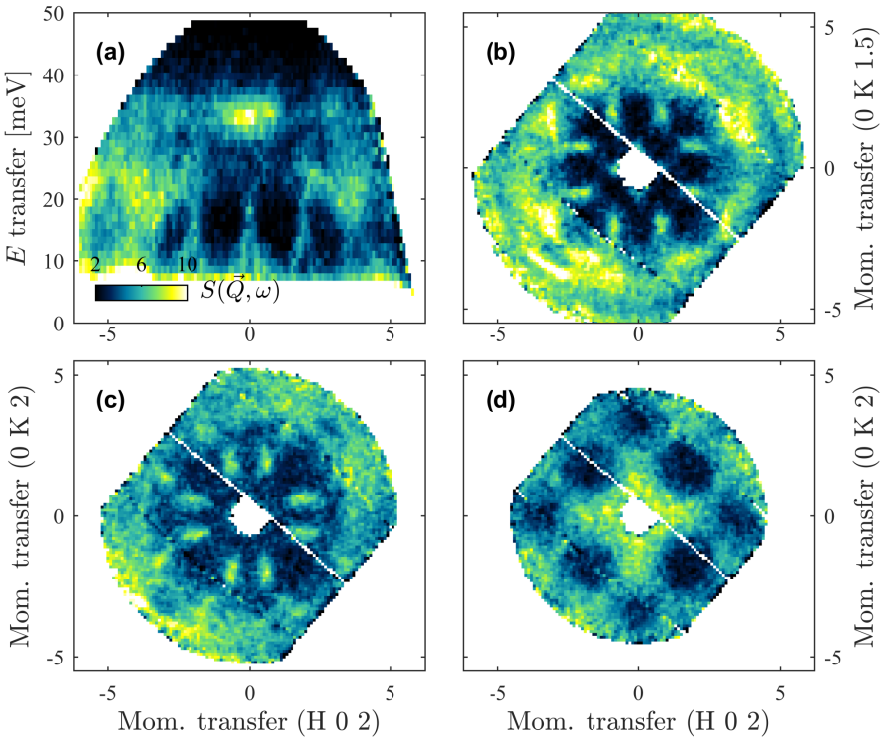

Figure 4.7: Magnon dispersion of $Lu_2V_2O_7$ at 4 K measured with E_i = 80 meV. (a) Slice of the data averaged for -1.5 < K < -0.5 and 0 < L < 4. While the dispersive invensity around 20 meV energy transfer is due to phonons, the magnetic signal at low $\vec{Q}$ extends up to approximately 35 meV. (b) Slice of the data averaged for 0 < L < 3.5 and 18 < E < 24. (c) Slice of the data averaged for 0 < L < 3.5 and 24 < E < 30 meV. (d) Slice of the data averaged for 0 < L < 3.5 and 30 < E < 36 meV.

4.3.2 Reduced axis plot

In order to make use of the symmetry of the lattice and the dispersion, we have developed a new visualization method for this data, which is sketched here.

In the case of $D = 0$ the Hamiltonian 4.2 can be diagonalized, as shown in [118]. Specifically, with the definition

$$A(\vec{Q}) = \cos(\pi H)\cos(\pi K) + \cos(\pi K)\cos(\pi L) + \cos(\pi L)\cos(\pi H) \quad (4.4)$$

the dispersion can simply be expressed as

$$\begin{aligned} \hbar\omega_{1,2}(\vec{Q}) &= J\left(2 \pm \sqrt{1 + A(\vec{Q})}\right) \\ \hbar\omega_{3,4}(\vec{Q}) &= 4J. \end{aligned} \quad (4.5)$$

We define the *reduced axis coordinate* $t(\vec{Q}) = 2 - \sqrt{1 + A(\vec{Q})}$ (for convenience the $\vec{Q}$-dependence of t will be dropped). By definition t is a unitless scalar between 0 and 2[1]. The dispersion can be expressed in very simple terms as a function of t: the acoustic mode for instance is proportional to t. The effect of D will be considered later.

$$\begin{aligned} \hbar\omega_1(t) &= Jt \\ \hbar\omega_2(t) &= J(4 - t) \\ \hbar\omega_{3,4}(t) &= 4J. \end{aligned} \quad (4.6)$$

The rebinning of the experimental data to a reduced axis coordinate is equivalent to reducing a spherically symmetrical system to $|\vec{Q}|$ (commonly done e.g. for powders), with the important distinction that the entire Brillouin zone is rebinned to $0 < t < 2$.

[1] It is trivial that $A(\vec{Q}) \in$ [-1,3] $\forall\ \vec{Q}$.

The experimental data as a function of the reduced axis coordinate

As a further precaution in order to enhance the contrast between magnon modes and the background and avoid contamination from the phonons, it is possible to neglect the data with $|\vec{Q}| > Q_{limit}$ for some empirical value Q_{limit} chosen as to result in optimal contrast (4 r.l.u. for $E_i = 25$ and 50 meV, 3 r.l.u. for $E_i = 80$ meV).

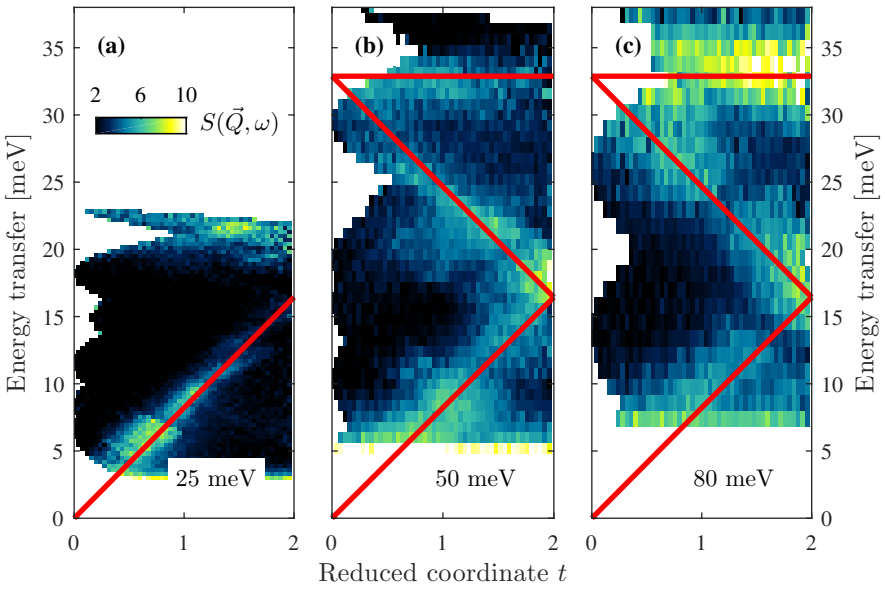

Figure 4.8: Reduced plots for all incoming energies. The dispersion as a function of t, described in the Eq. 4.6, is fitted (red lines) to obtain $J = 8.1(1)$ meV. The different sampling of $\vec{Q}$-space explains the different weight given to specific parts of the dispersion: for instance the node at $t = 2$ and $E \simeq 16$ meV is very intense when measured with an incoming energy of 50 and 80 meV, but is almost absent with 25 meV.

Figure 4.8 shows the result of the rebinning to the reduced axis coordinate on all datasets. The data follows the expectations from the model, folding into a set of lines whose fit suggests $J = 8.1(1)$ meV. These fits are dominated by the doubly-degenerate band at $4J$.

A closer look at the reduced data with 25 meV incoming energy is pre-

sented in Fig. 4.9, where the energy of the mode is extracted (under the assumption of the signal's lineshape being Gaussian) and then fitted to a line, with a direct FM exchange of $J = 7.3(2)$ meV and a gap of 0.8(2) meV. This is not a reliable approximation of the actual gap (these values are inconsistent with the high-energy bound mode due to the much reduced value of J), but serves mostly to establish an upper bound to the gap assuming that the dispersion is proportional to $\vec{Q}^2$ in the proximity of Γ.

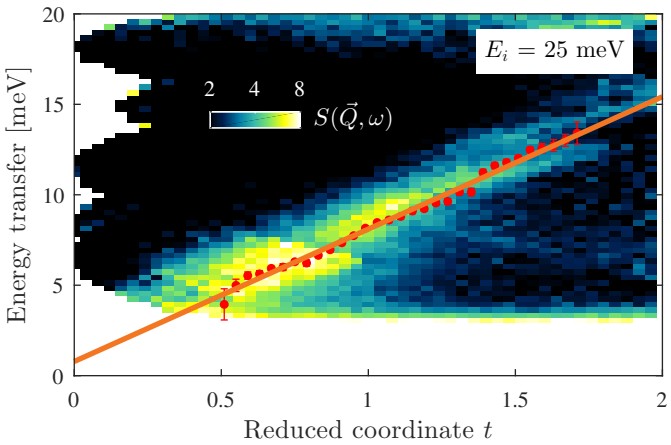

Figure 4.9: Fit of the reduced dataset obtained with $E_i = 25$ meV (logarithmic scale). The energy of the mode (red dots) as a function of t is extracted from the data and fitted to a line (orange).

Despite the extreme simplicity of this analysis, we can already conclude that a minimal model containing only the FM interaction accounts for the main features of the scattering. In particular, we can identify no further spectral modes, meaning that a four-site, four-modes Hamiltonian is sufficient to describe the spectrum (which again suggests that *nnn* interactions can be neglected within the goodness of the data). A second remark is that the spectral intensity in the reduced plots follows straight lines, both confirming the shape of the dispersion and its dependence on J – i.e. linear with respect to t, a coordinate which doesn't depend in any way on the Hamiltonian. Finally, this simple analysis suggests an approximative value for J of 8.1(1) meV.

We also set an upper limit to the gap at 0.8(2) meV, i.e. one order of magnitude below the direct exchange. However, this analysis for now is unable to establish a value for the DMI. The reason is that, as highlighted in Fig. 4.4, the DMI has very little effect on the acoustic and optical branches for most values of $\vec{Q}$ – only at the zone boundary it has an appreciable effect – and, as far as the reduced plots, the DMI manifests itself as a widening of the intrinsic lineshape. A finer analysis is thus required to address the question of the magnitude of D.

4.4 Modelling of the data

4.4.1 Modelling methods

The energy of the magnon can be derived from Eq. 4.2, and the spectral weight can be calculated using a paper by H. Ichikawa [114]. Simulations with $J = 8.1$ meV (as indicated by the reduced plots) are diplayed in Fig. 4.10. While this approach accounts very well for the signal below $2J$, clear discrepancies are found at higher energy transfers. This is most likely due to the Holstein-Primakoff approximation, which is a harmonic expansion on the ground state [134]; while at low energy transfers the magnon can be considered a perturbation of the ground state, the deviation at higher energy transfers is a result of these approximations no longer holding. Specifically, Fig. 4.10(f) seems to lack a phase factor.

In order to simulate the spectrum we therefore use the program suite McPhase [135, 74]. The inputs for this program are the magnetic sites and the Hamiltonian, which are used for a Monte Carlo simulation, simulating the magnetic structure at a given temperature. Then a mean-field spin-wave theory is employed to obtain the dispersion and the spectral weights. This approach is expensive in terms of computation and time, but the mean-field method used to calculate the spectral weight performs equally well at all energies – as it does not rely on approximations on the ground state. McPhase has already been used to explain several interesting properties,

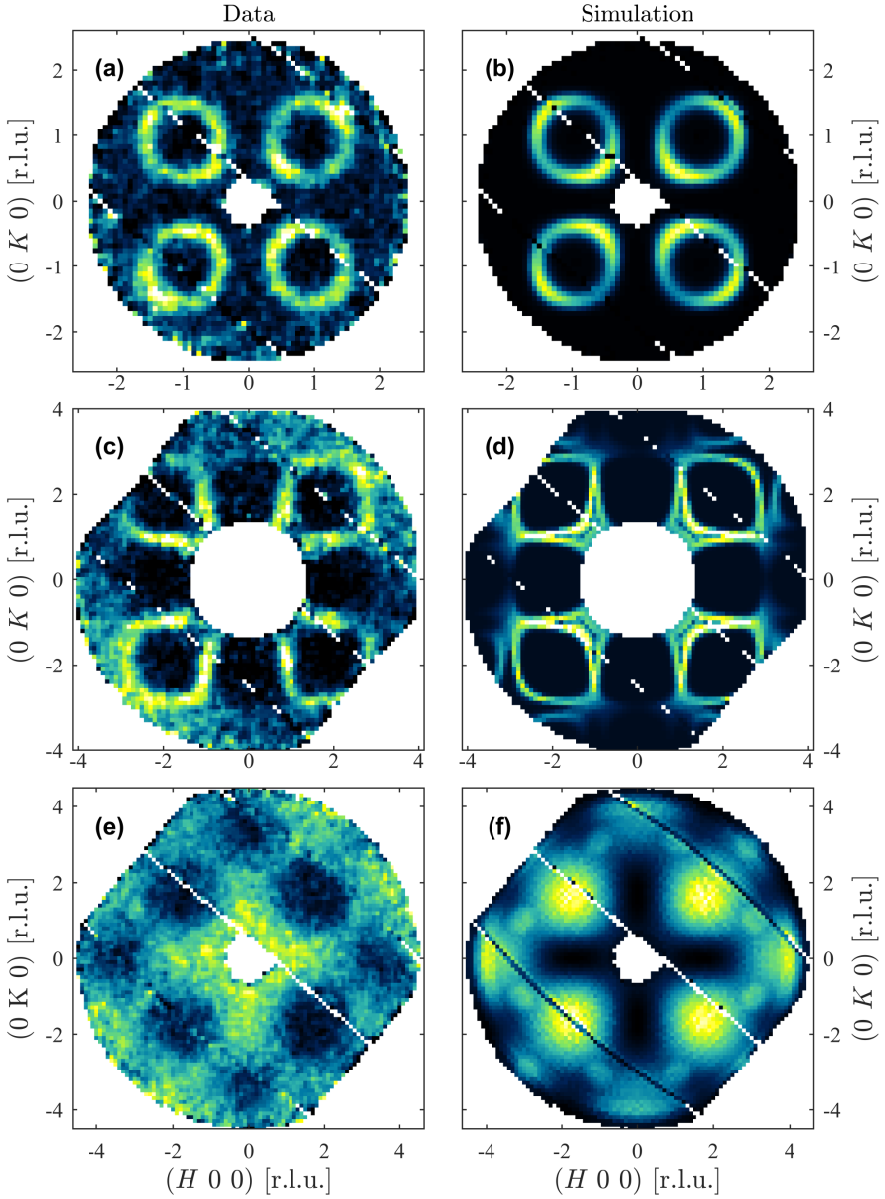

Figure 4.10: Data (left) versus simulations (right) for $J = 8.1$ and $D = 0$ based on the Holstein-Primakoff approximation. The averaging ranges and the color map are as previously explained in Fig. 4.5(d), 4.6(d), and 4.7(d). The agreement is very good at the lowest energy transfer, but poor at higher energy transfers, e.g. between (e) and (f).

such as magnetic phase diagrams and spectra in a number of magnetic systems [136, 135, 137, 138, 139, 140].

A simulation of the spectrum of $Lu_2V_2O_7$ for $J = 8.1$ and $D = 0$ meV is presented in Fig. 4.11. This method is shown to describe adequately the spectrum at all energy transfers, including the doubly-degenerate bound mode at $4J$.

While these simulations are useful in making sure that the general properties of the spin waves are described, they are of little use in determining D, and a full fitting of the spectrum is required.

4.4.2 Fitting of the reduced plots

Reduced plots are suited to perform fits as the collapse the whole data into a limited interval, i.e. [0,2]. Due to the computational requirements of McPhase, a simulation of the whole spectrum is beyond the available resources. Instead of fitting the whole dataset, a simultaneous fit on a number of cuts was performed.

The fitting procedure can be summarized as follows:

- Select a number of cuts to be examined. Specifically we will consider a cut around $2J$ at $t = 2$ and two cuts around $4J$ at t around 0.8 or 1.6.

- All of these cuts are taken from the reduced plots for $E_i = 50$ meV. The data with $E_i = 25$ meV has almost no intensity at $2J$ and does not cover the doubly-degenerate bound mode, the data with $E_i = 80$ meV has a larger instrumental resolution. The data with $E_i = 50$ meV is thus best suited.

- As discussed previously, the sample is divided into domains with different orientations for the local magnetic field. It will be assumed that the domains order according to the easy direction, $\vec{H} = [1\ 0\ 0]$, $[0\ 1\ 0]$ and $[0\ 0\ 1]$. Three spectra will be calculated and averaged.

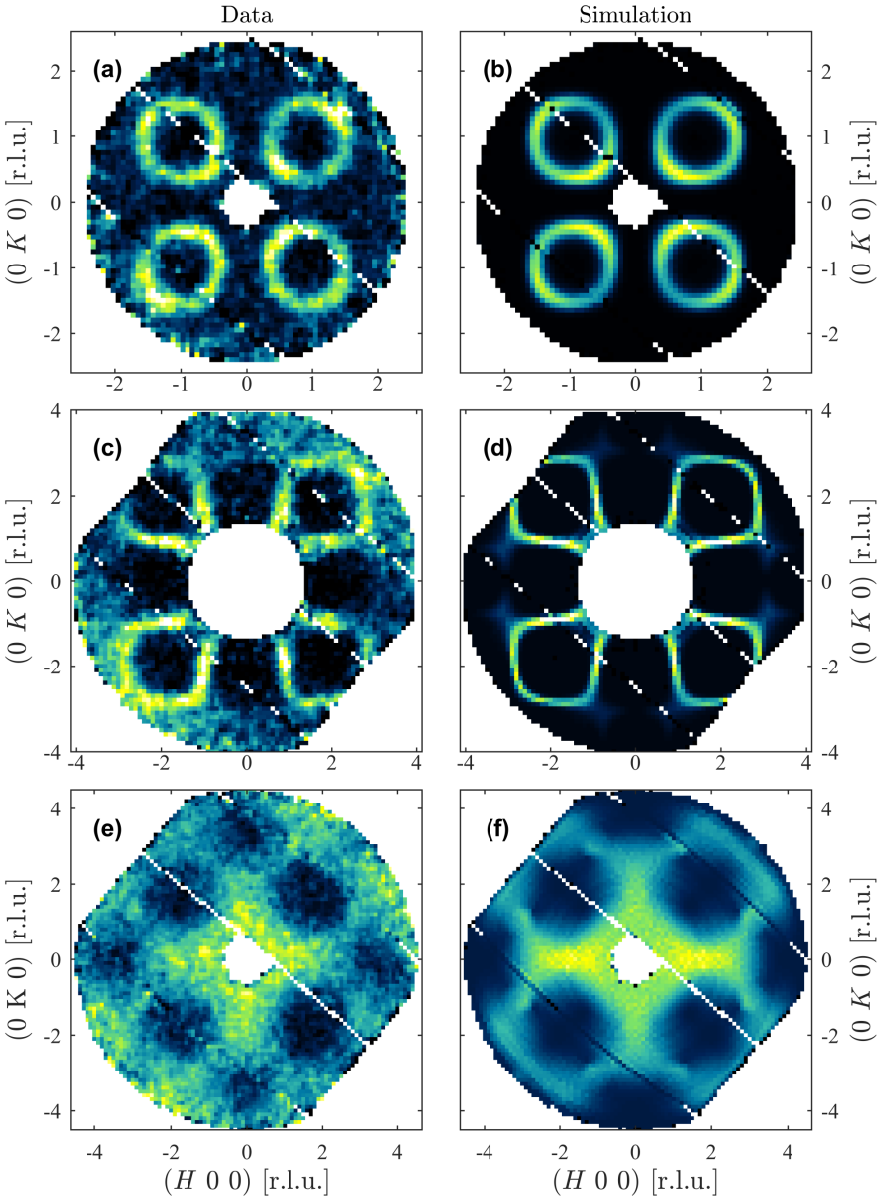

Figure 4.11: Data (left) versus McPhase simulations (right) for $J = 8.1$ and $D = 0$ meV. The averaging ranges and the color map are as previously explained in Fig. 4.5(d), 4.6(d), and 4.7(d). In general, there is good agreement between the data and the simulations.

- The fitting procedure involves selecting the portion of $(\vec{Q}, \omega)$-space that contributes to a specific (t, E) range, simulating the scattering $S(\vec{Q}, \hbar\omega)$ and reducing it to (t, E) coordinates in order to perform the fit.

- The background was modelled as being collinear to the energy.

The instrumental resolution was modelled as a Gaussian of width 2.6 meV (at an energy transfer of 30 meV for an incoming energy of 50 meV), a result derived using Tobyfit [141]. The accuracy in this calculation is crucial as the DMI manifests itself as a widening of the magnon, and thus may correlate with the instrumental resolution.

Figure 4.12 shows fits of the reduced plots. We have obtained a very good agreement between the data and the model for the values of $J = 8.22(2)$ meV (compare with the value of 8.1(1) meV previously obtained) and $D = 1.5(1)$ meV. The best value for χ^2 is 2.9.

At energy transfers below $4J$ no effect of the DMI can be detected even at the zone boundary ($t = 2$), which we explain in terms of the instrumental resolution (around 4 meV) dominating over a potential broadening. At energy transfers around $4J$ the effect of the DMI is markedly t-dependent. It is found, for instance, that the DMI has a particular importance at $t = 1.6$, leading to a very clear alteration of the lineshape.

Figure 4.13 shows McPhase simulations of the experimental data, once again displaying a good agreement of the simulations with the data (which was already established by the simulations with $D = 0$). Furthermore Fig. 4.14 shows comparisons between two selected cuts, fits thereof and simulations performed with $D = 0$. The model explains satisfyingly the spectral distribution and the lineshapes of the magnon.

4.5 Conclusions and outlook

We have performed a high-quality neutron scattering experiment on $Lu_2V_2O_7$ and measured its spin-wave dispersion. In order to analyse the

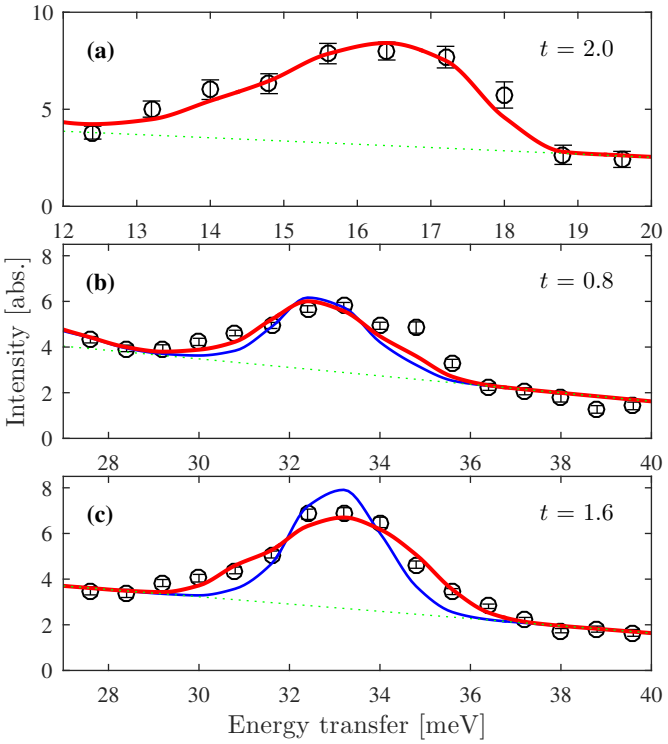

Figure 4.12: Various cuts of the data in rebinned coordinate (black) compared to fits at the optimum values of $J = 8.22(2)$ and $D = 1.5(1)$ meV (red). The blue curves are simulations with $J = 8.22$ and $D = 0$ meV to visualize the effect of the DMI on the dispersion. The dotted green line marks the linear background. (a) At $2J$ the mode is expected to present substantial splitting at the zone boundary $t = 2$. However, the width is dominated by the instrumental energy resolution and no effect can be resolved. (b) A high-energy average for $0.7 < t < 0.9$. In this cut the difference between $D = 0$ and $D = 1.5$ meV is small. (c) A cut for $1.5 < t < 1.7$. In this instance the effect of the DMI is substantial.

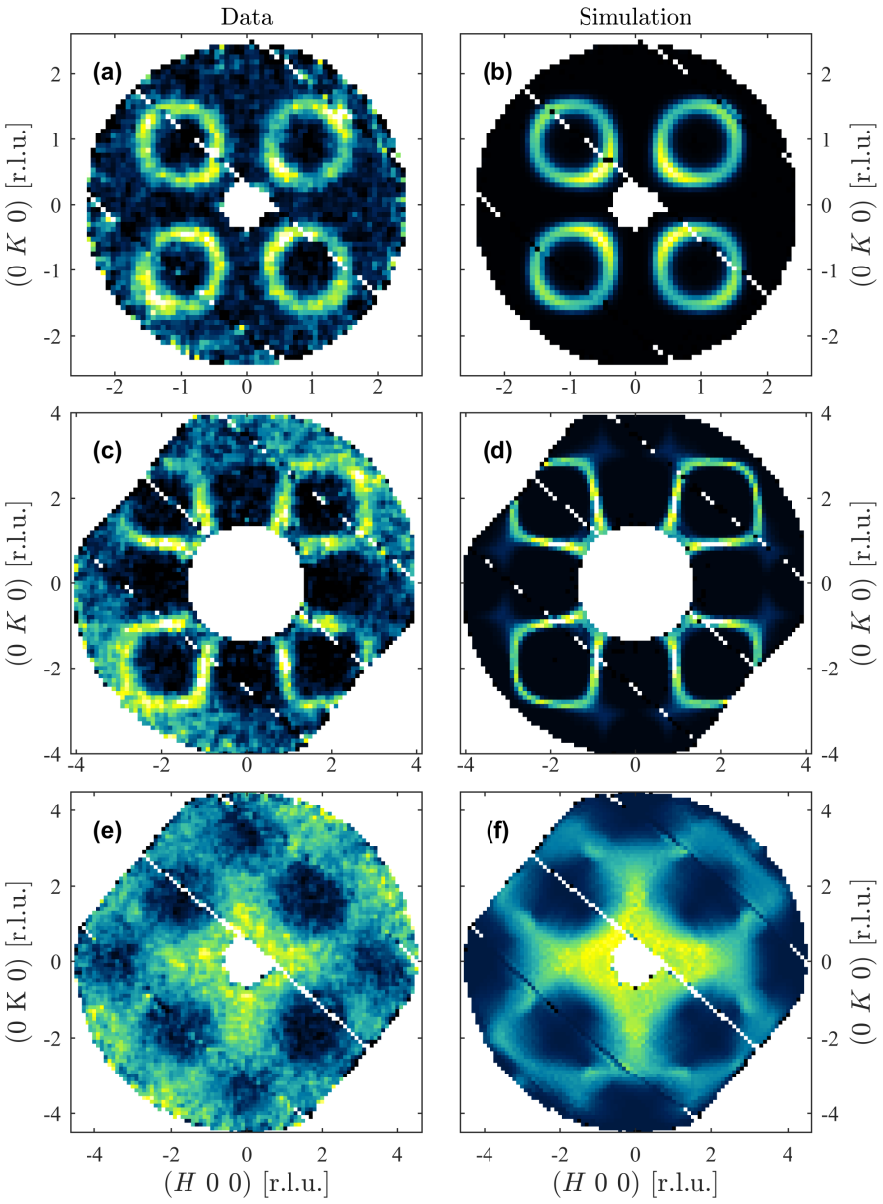

Figure 4.13: Data (left) versus McPhase simulations (right) for $J = 8.22$ and $D = 1.5$ meV. The averaging ranges and the color map are as previously specified in Fig. 4.5(d), 4.6(d), and 4.7(d).

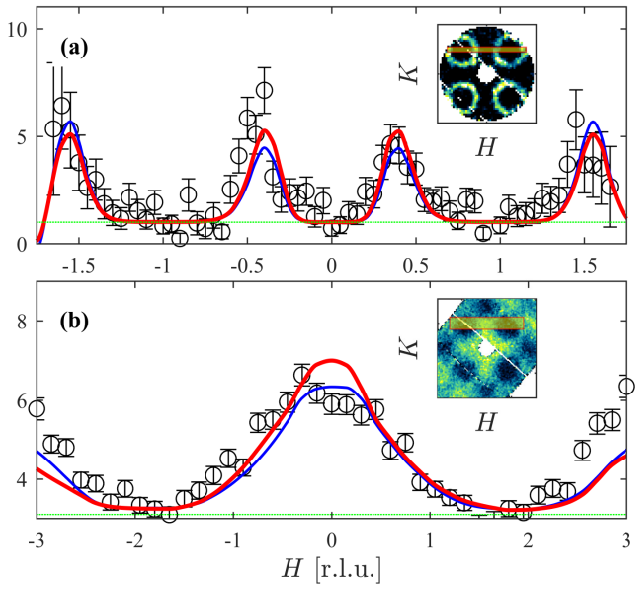

Figure 4.14: Comparison between the experimental data (black circles), the fits (red) and simulations without the DMI (blue) as for two cuts. The green lines mark the constant background. Compare to Fig. 4.5(d) and 4.7(d). (a) Cut performed on the dataset with $E_i = 25$ meV with $0.9 < K < 1.1$, $0.9 < L < 1.1$, and $6 < E < 8$ meV. The inset shows a reference slice at this energy transfer and L value, while the yellow rectangle shows the region of averaging in K. At this energy transfer, there are very little differences due to the DMI. (b) Cut performed on the dataset with $E_i = 80$ meV with $1.5 < K < 2.5$, $2 < L < 6$, and $30 < E < 36$ meV. With the scattering at this energy transfer resembling a cross, this cut goes through the "upper" arm of the cross, displaying a wide peak of scattering (with a FWHM exceeding the reciprocal lattice unit). The effects of the DMI, while perceivable, are very contained.

data we have developed a rebinning technique that allows to reduce all $\vec{Q}$-vectors to a scalar value $t \in [0\ 2]$. In the case of $D = 0$ the dispersion becomes a series of straight lines once rebinned.

Due to the complexity of the spectral weight, modelling of the data was performed with the program McPhase, which provided an outstanding agreement. In general no further interaction or effect is required in order to explain the dispersion within the limits of our data.

Furthermore, fits of the reduced data allowed to identify specific regions where the effect of the DMI is particularly visible. The fits resulted in the values of $J = 8.22(2)$ and $D = 1.5(1)$ meV.

The ratio between the direct FM interaction and the DMI is 0.18(1). While not the value of $\sim 1/3$ originally obtained to explain the thermal transport measurements by Onose *et al.* [118], this ratio is larger than those obtained in other theoretical approaches [113, 121]. Our result highlights the presence of a large DMI in $Lu_2V_2O_7$ and is a strong, independent argument in favour of the existence of the thermal Hall effect.

At the end of this study, some outstanding points are still to be investigated.

- Our Hamiltonian includes no next-nearest neighbour interaction nor single-ion anisotropy (in contrast to other insulating pyrochlores, such as those giving rise to the spin-ice behaviour), and predicts no gap at the Γ point (although we can estimate an upper limit of 0.8(2) meV by assuming linearity). In general measurements with a higher accuracy and energy resolution are required to motivate the presence of these terms or completely exclude them.

- Due to the absence of an external magnetic field during the measurement the data is described as an average of all possible local magnetic directions. A high-resolution in-field measurement is required in order to observe split modes (i.e. at the zone boundary at $2J$, or at $4J$) and decrease the uncertainty on the value of D.

- Our study is by construction symmetric with respect to the sign of D, i.e. we cannot determine the direction of $\vec{D}_{j,k}$. However, measurements of the thermal magnon Hall effect have been interpreted in terms of opposite signs of D [123]. Conventional methods used to determine the sign of D rely usual on structural signatures (e.g. the orientation of a spiralling magnetic order) [142, 143], but $Lu_2V_2O_7$ is a collinear ferromagnet [132]. The question of the direction of the DMI is thus still open and relevant to the development of magnon topological insulators [123].

- We are confident that this result will stimulate further discussion and research in the study of the thermal magnon Hall effect in the hope to establish a solidified model of this phenomenon.

To further the investigations on this compound, we suggest to perform in-field measurements of the spectrum in order to avoid modes overlapping. For instance, a triple-axis measurement at the Γ-point around an energy transfer of $4J$ should highlight two additional peaks at $4J \pm \sqrt{2}D$, allowing a direct measurement of the DMI. Similarly, measurements at the Γ-point close to the elastic line might be attempted to confirm the gaplessness of the system. We have carried out several attempts in this direction, using for instance polarized neutron spectroscopy at ILL, but the energy resolution has proven to be a challenge.

Chapter 5

Triplon-to-triplon interactions in the 2D dimerized antiferromagnet $SrCu_2(BO_3)_2$

5.1 Scientific background

Lattice geometry can induce a wide array of interesting and unexpected effects even in the simplest symmetries. It is the case for the so-called Shastry-Sutherland geometry [144, 145], a 2D square structure that potentially exhibits dimerization and frustration due to the next-nearest neighbour (*nnn*) antiferromagnetic interaction being stronger than the nearest-neighbour (*nn*) exchange, as sketched in Fig. 5.1(a).

The frustrated nature of the Shastry-Sutherland lattice means that usually there is no long-range order [145]. However, several forms of short-range order, such as dimers, plaquette and stripy order [146, 147] have been proposed. One of the few material realizations of the Shastry-Sutherland model is the compound $SrCu_2(BO_3)_2$ (SCBO) [148, 149, 150], whose structure is sketched in Fig. 5.1(b). Another material that realizes this geometry is the tetragonal rare-earth-metal TbB_4 [151]. In these compounds, magnetization plateaus appear at certain ratios of the full magnetization, as shown in Fig. 5.2 [148, 152, 153]. A full explanation of the reason behind these plateaus is available in Ref. [154].

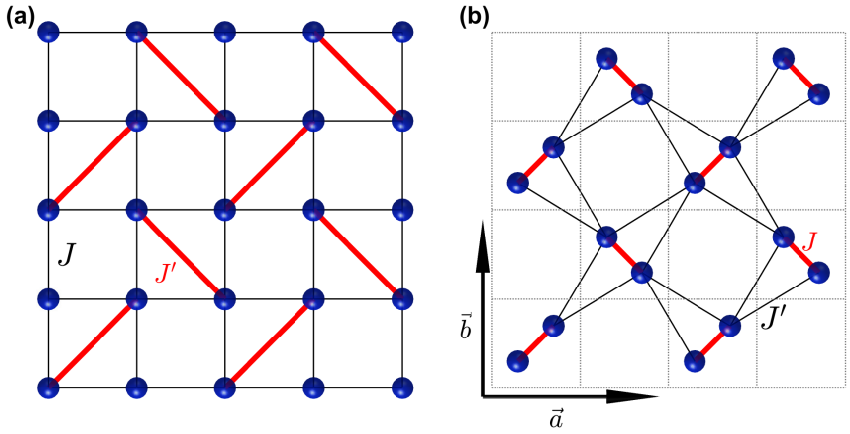

Figure 5.1: Structure of $SrCu_2(BO_3)_2$. (a) In the Shastry-Sutherland geometry, ions form a square lattice and their interactions are dominated by the diagonal next-nearest neighbour exchange J' (red lines). If J' is an antiferromagnetic interaction, the lattice is geometrically frustrated. (b) SCBO crystallizes in a topologically equivalent structure with pairs of Cu^{2+} ions lying perpendicular to their four neighbouring pairs.

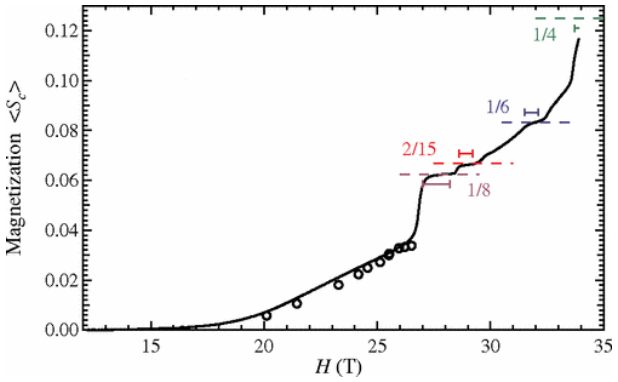

Figure 5.2: Magnetization as a function of external magnetic field in SCBO. The solid black line and the open circles are obtained using various techniques. The horizontal colored lines mark the positions of the magnetization plateaux as determined via NMR: they can be found at 1/8, 2/15, 1/6 and 1/4 of the full magnetization [153].

In SCBO, which cristallizes in the tetragonal $I\bar{4}2m$ symmetry ($a = b =$ 8.995 and $c = 6.649$ Å), the magnetic Cu^{2+} ions ($S = 1/2$) lie on 2D planes (the a-b planes) that are topologically equivalent to the Shastry-Sutherland lattice, with the notable difference in terminology that the dominant interaction is between the couples of ions that lie the closest to each other. Theoretical studies have suggested a phase diagram as shown in Fig. 5.3 [155], where the ratio between two exchange parameters in the plane (J and J') and one out-of-plane parameter (J'') can lead to several ground states. Further states, such as quadrimerized, have been suggested [156]. The exchange parameters of SCBO position it very near to the quantum phase transition, as shown in Fig. 5.3 so that it is possible to trigger a phase transition from a dimerized state to a plaquette state: this can be achieved for instance by using pressure to change the lattice parameters [157].

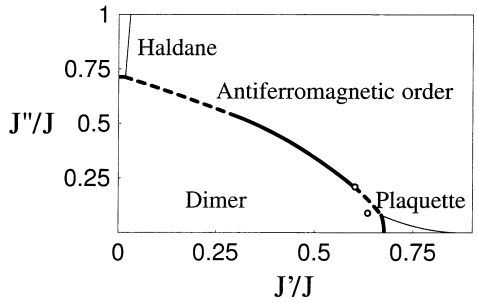

Figure 5.3: Proposed phase diagram of the three-dimensional compound of stacked Shastry-Sutherland planes, such as SCBO. The exchange parameters J, J' and J'' are respectively the intra-dimer, inter-dimer, and inter-plane couplings. The open circle mark the proposed location of SCBO. Reproduced from [155].

I have performed inelastic neutron scattering experiments on SCBO in order to measure its spectrum and determine the Lorentzian widening of its lineshape as a function of $\vec{Q}$. In this chapter I will present the data and my analysis.

5.1.1 The Hamiltonian of SCBO

In first approximation, SCBO is described by the Hamiltonian:

$$\mathcal{H} = \sum_{nn} J\vec{S}_j \cdot \vec{S}_k + \sum_{nnn} J'\vec{S}_j \cdot \vec{S}_k + \sum_{oop} J''\vec{S}_j \cdot \vec{S}_k,$$

where *nn* labels intra-dimer exchanges, *nnn* labels inter-dimer exchanges, and *oop* labels the out-of-plane interactions. The small ratio of $J''/J < 1/10$, and the fact that the interaction is frustrated, mean that out-of-plane contributions can be neglected.

In its ground state, the spins are expected to form antiparallel singlets for $J'/J < 0.68$, a ratio that defines a quantum critical point above which the ground state is unknown but suspected to be quadrumerized [156]. Susceptibility measurements for SCBO [158, 159] suggested $J'/J = 0.62$, right below the quantum critical point.

In this regime the lowest-lying magnetic excitation is a singlet-to-triplet excitation. The resulting quasiparticle, called a triplon, is a hard-core boson (i.e. two such bosons cannot share the same dimer site). The frustrated interaction between dimers drastically reduces the hopping probability [160], resulting in a flat triplon dispersion despite the strong inter-dimer interaction.

However, the symmetry together with a slight buckling of the Cu^{2+} ionic planes allow for the Dzyaloshinskii-Moriya interaction (DMI) [10, 11], thus introducing new terms in the Hamiltonian:

$$\mathcal{H} = \sum_{nn} \left(J\vec{S}_j \cdot \vec{S}_k + \vec{D}_{j,k}(\vec{S}_j \times \vec{S}_k)\right) + \sum_{nnn} \left(J'\vec{S}_j \cdot \vec{S}_k + \vec{D'}_{j,k}(\vec{S}_j \times \vec{S}_k)\right),$$

with two sets of DM vectors. First order perturbation theory allows to reduce the number of variables in this Hamiltonian by applying a local rotation of the spins $\vec{S}$ to $\vec{S}'$. In this new system,

$$\mathcal{H} = \sum_{nn} J\vec{S'}_j \cdot \vec{S'}_k + \sum_{nnn} \left(J'\vec{S'}_j \cdot \vec{S'}_k + \tilde{D}_{j,k}(\vec{S'}_j \times \vec{S'}_k) \right) + \mathcal{O}(\frac{D}{J});$$

where the new DMI vector $\tilde{D_{j,k}}$ has two components: an a-b component $D_\parallel$ and a component along the c axis $D_\perp$:

$$\begin{aligned} \tilde{D}_\parallel &= D'_\parallel + \frac{J'}{2J} D_\parallel \\ \tilde{D}_\perp &= D'_\perp. \end{aligned}$$

Neglecting the higher orders $\mathcal{O}(D/J)$ of the Hamiltonian leads to the matrix form

$$\mathcal{H}(\vec{Q}) = \begin{pmatrix} J+\tilde{D}_\perp f(\vec{Q}) & -i\tilde{D}_\parallel g(\vec{Q}) & 0 \\ i\tilde{D}_\parallel g(\vec{Q}) & J & i\tilde{D}_\parallel g(\vec{Q}) \\ 0 & -i\tilde{D}_\parallel g(\vec{Q}) & J-\tilde{D}_\perp f(\vec{Q}) \end{pmatrix} \tag{5.1}$$

for some functions $f(\vec{Q})$ and $g(\vec{Q})$, whose solutions are

$$\begin{aligned} \hbar\omega(\vec{Q})_0 &= J \\ \hbar\omega(\vec{Q})_{1,2} &= J \pm \sqrt{\tilde{D}_\perp^2 f(\vec{Q}) + 2\tilde{D}_\parallel^2 g(\vec{Q})}. \end{aligned} \tag{5.2}$$

These solutions are symmetrical with respect to J. A simulation of the spectrum (including the spectral weight) is shown in Fig. 5.4.

We note that, as the dispersion without DMI is perfectly flat and thrice degenerate (up to higher expansions in J'/J), any dispersion is dominated by the DMI. The low dispersion of the triplons is expected from the low mobility: an ideally localized excitation is expected to have a flat Fourier transform. The DMI dominating the dispersion is in stark contrast to most known materials.

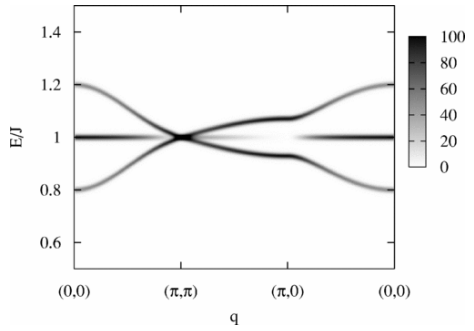

Figure 5.4: Dispersion relations of the three triplon branches derived from the Hamiltonian 5.1, figure from reference [161].

5.1.2 Exact diagonalization

The Hamiltonian 5.1 however did not explain the experimentally observed dispersion. This was explained in terms of the first order perturbation theory, which was used in deriving this analytical Hamiltonian, not being adequate – especially due to the closeness of a quantum critical point at $J'/J = 0.68$.

Exact diagonalization was performed on a 32-site cluster in order to compute the lowest-lying excited states of SCBO [161]. The result is shown in Fig. 5.5 for $\tilde{D}_{\perp} = 0.18$ meV and $\tilde{D}_{\parallel} = 0.07$ meV. Despite the cluster size and the constraint on J'/J to be 0.62, there is general agreement between the experimental data and the exact diagonalization.

To conclude, the singlet-to-triplet excitations in SCBO are three modes centred around an energy transfer of 3 meV, ranging from the most dispersive at the bottom to the least dispersive at the top, residing in a bandwidth of roughly 0.4 meV.

Of further note is the magnitude of the gap. Dispersionless dimers could be expected to have a flat dispersion with a gap of J. It has however been shown that for the Shastry-Sutherland geometry, the size of the gap is a function of J'/J: for $J' = 0$ then the gap Δ is equal to J, but as J'/J increases the gap decreases [164], see Fig. 5.6. In the case of SCBO, fits of the susceptibility measurements [158, 159] suggested that $J = 85$ K, $J' =$

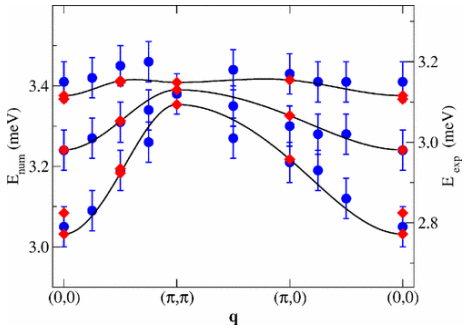

Figure 5.5: Comparison between experimentally measured data for the dispersion of SCBO [162, 163] (diamonds) and the result of exact diagonalization (circles) taken from [161]. The solid lines are a guide to the eye.

54 K, $J'' = 8$ K and $\Delta = 35$ K.

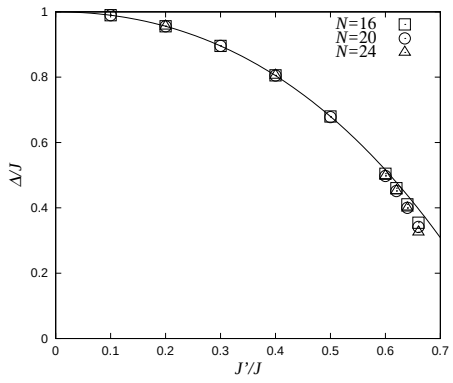

Figure 5.6: Ratio between the gap energy Δ and the AF interaction J as a function of J'/J. N indicates the size of the system that was used in the computation. Figure reproduced from [164].

5.1.3 Temperature dependence of the spectrum

In dimerized materials a non-zero temperature leads to a thermal population of quasi-particles, characterised by increased repulsion, reduced mobility, and a reduction of the dispersive bandwidth [165]. As a rule of thumb, in a system with a gap the excitation is expected to remain visible up to a temperature comparable to the gap (as is the case to varying degrees in

both $RbCoCl_3$ and $Lu_2V_2O_7$).

However, this is not true in SCBO, as the intensity of the triplon is strongly suppressed above $T = 5$ K $\ll \Delta = 35$ K $\ll J = 85$ K, and turns into a flat continuum around 15 K. A summary of previous results from inelastic neutron scattering investigations is presented in Fig. 5.7.

This unusual phenomenon has been explained in terms of a triplon-to-triplon interaction. The mechanism is as follows: a triplon, be it thermally excited or created by an incident neutron, polarizes its surrounding singlets (it lifts the local degeneracy for the two singlets perpendicular to its direction). Previous studies using exact diagonalization suggested that this locally ordered state can extend for 1.3 lattice units, i.e. ∼5 unit cells [157]. Figure 5.8 shows a simplified picture of the triplon-to-triplon polarized shell. In the lower part of the grid, a thermally-excited triplon polarizes the singlets around itself, creating a polarized shell (light blue circle). In the upper part of the grid, a new triplon is excited (e.g. by a neutron) several unit cells away, but their shells overlap resulting in an effective interaction and a much faster decay channel. One polarized shell covers ∼10 dimers: thus a relatively small number of thermally excited triplons (one in nine) guarantees a substantial, if not complete, coverture of the plane. This is the reason why even with $T < \Delta$ the triplons interact strongly and may not be long-lived.

In previous neutron scattering measurements, the magnetic signal has been divided into two components, as shown in Fig. 5.9. Firstly the so-called *sharp* (i.e. resolution-limited) component, which is the manifestation of triplons excited far away from any other triplon. The intensity of the sharp component is expected to be maximal and dominant at $T = 0$ K, and to drop quickly as triplons are thermally excited. Secondly the so-called *broad* component, which is characterized by a temperature-dependent Lorentzian convolution induced by the decay time of triplons (which is a function of the triplon density). The intensity of this component is expected to be zero at low temperature, to then rise as spectral weight moves away from the sharp

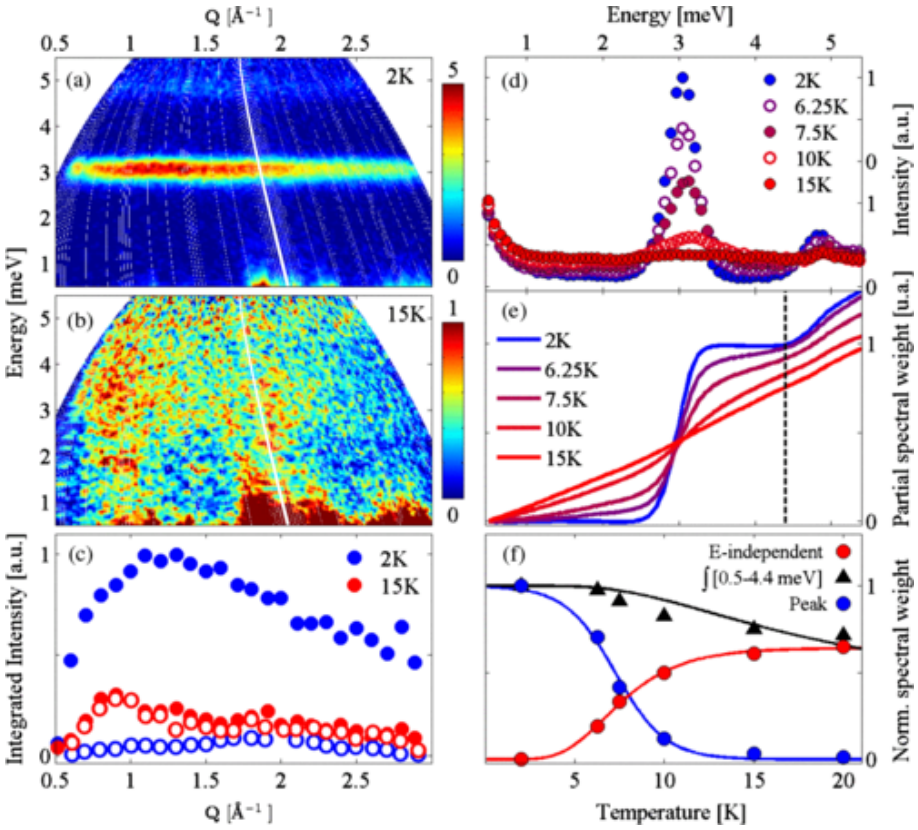

Figure 5.7: Results from previous INS studies on a SCBO powder sample performed on FOCUS (PSI) [160]. (a,b) Dispersion of SCBO at 2 and 15 K. (c) $\vec{Q}$-dependence of scattered intensities. Solid dots are integrations centred on the triplon energy ($2.8 < E < 3.2$) while empty dots are averaged in other energy-regions ($1.5 < E < 2.2$ and $2.8 < E < 4.2$). (d) $\vec{Q}$-integrated spectrum. (e) Partial spectral weights. (f) Fitted components of the spectrum: the peak intensity in blue, the flat background in red, and their sum in black.

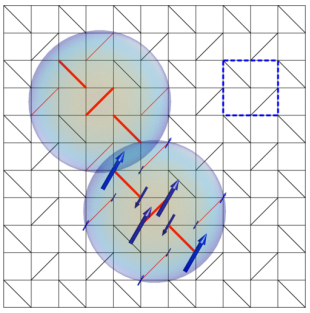

Figure 5.8: Illustration of the triplon-to-triplon interaction in SCBO, further explained in the text. The blue dashed line represent one unit cell. Image from [157].

to the broad component, and then to diminish at even higher temperatures.

While previous studies only studied this behaviour at a very limited number of $\vec{Q}$-points, the technique of ToF spectroscopy allows us to address the question of the $\vec{Q}$-dependence of the intensity of the two components, as well as of the Lorentzian width. This will be necessary for future studies in order to confirm the properties of the decay channels, as well as the spatial distribution of the magnetized shells of the triplons.

5.2 Experimental work on SCBO

In order to measure the dispersion of SCBO as a function of temperature two experiments were performed at LET (ISIS, RAL, UK) in Autumn 2011, and Spring 2013. Eleven high-quality single crystals, with a total mass of 10.3 g, were coaligned with (HHL) in the horizontal plane. Data were collected for the incoming energy E_i of 7 meV with an instrumental resolution (FWHM) of 0.153(7) meV at the elastic line, and datasets were collected for an average of 20 hours at the temperatures 2.5, 5.5, 7.3, 8.0, 8.5 and 10 K.

The data were corrected for detector efficiency and outcoming versus incoming wavevector ratio k_f/k_i using the program MANTID [45, 46]. The resulting $S(\vec{Q},\omega)$ datasets were analysed with the HORACE [47] software package. Unless otherwise noted, the results will be presented averaged

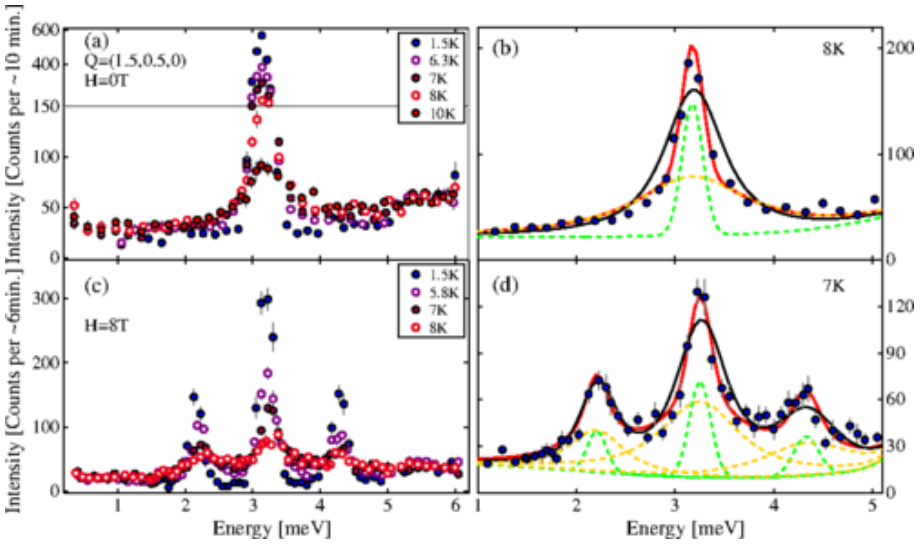

Figure 5.9: Scans and fits at $\vec{Q} = (1.5\ 0.5\ 0)$ from previous INS studies on a SCBO single crystal performed on the triple-axis spectrometer TASPby M. Zayed (PSI). (a) Scans at several temperatures. (b) Fit (red) of the magnetic signal at 8 K. The signal is separated in two components: a resolution-limited sharp Gaussian (green) and a broad Voigt curve (yellow). The black line is a fit to a single Lorentzian. (c,d) Effect of the magnetic field on the triplon.

along the direction L due to the strong two-dimensionality of the system. The resulting file had 40960 pixels and 501 time-bins.

5.3 Experimental results

Figure 5.10 shows the dispersion at base temperature $T = 2.5$ K. As expected from previous experiments, three dispersive modes are observed, ranging from the strongly dispersive lowest-lying mode to the almost-flat highest-lying mode. This confirms previous measurements on this compound. The excitations are centred around $\Delta \approx 3$ meV, which is equivalent to a temperature of 34 K.

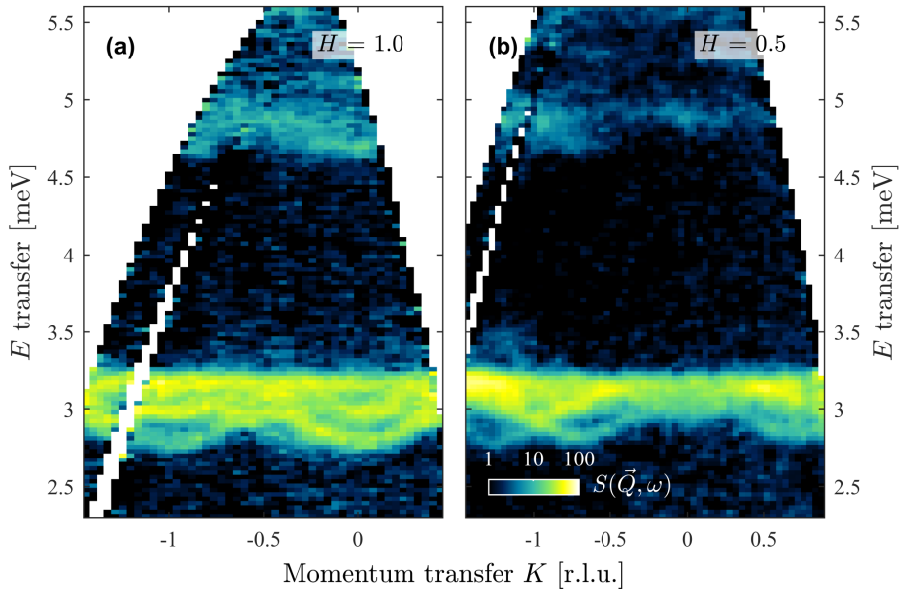

Figure 5.10: Triplon dispersion in SCBO at $T = 2.5$ K in two distinct $H - K$ planes shown in a common logarithmic color scale. The data is averaged with (a) $0.925 < H < 1.075$, (b) $0.425 < H < 0.575$ r.l.u., and shows the three singlet-to-triplet excitations around 3 meV energy transfer. The signal above 4.5 meV is magnetic in nature and explained as two-triplon excitations. The oblique line of white pixels originates from a gap in the detector coverage of LET.

Figure 5.11 shows the evolution in temperature of the magnetic excitation in a specific subset of the data. The triplon excitations are sharp at the lowest temperature, and as expected are broadened to the point of being flat at 10 K $< \Delta$. Moreover, Fig. 5.12 displays cuts data performed around the excitation at three $\vec{Q}$-points at all temperatures. These show with more clarity the trend towards increased broadness and the decreased intensity of the triplons.

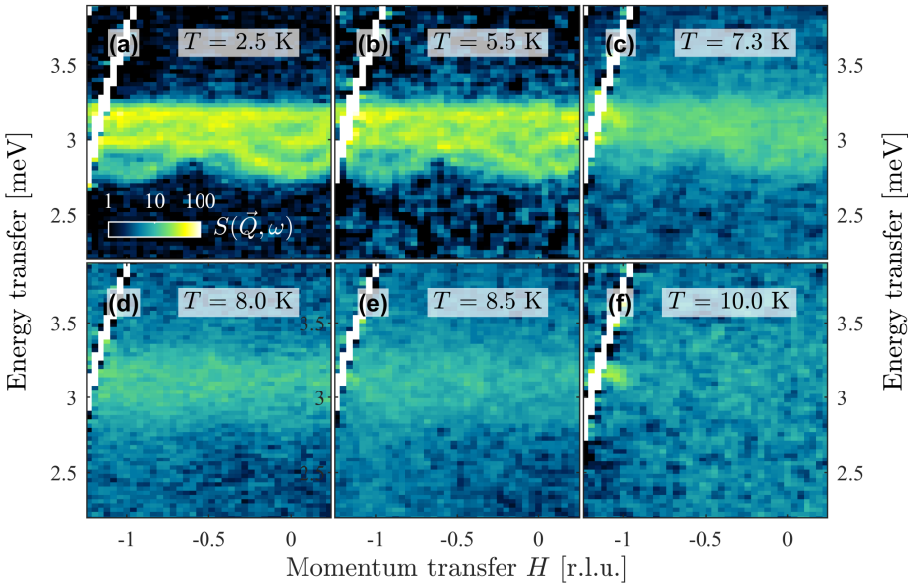

Figure 5.11: Triplon dispersion in SCBO at all experimental temperatures, shown on a common logarithmic scale. The averaging conditions are the same as in Fig. 5.10(a). The magnetic signal at 2.5 and 5.5 K is comparable, but it decreases in maximum intensity and becomes much wider at higher temperatures, becoming almost featureless at 10 K.

This data is consistent with the many studies previously conducted on SCBO. The FWHM of LET at an energy transfer of 3 meV, estimated by fitting the data at 2.5 K with a set of Gaussian functions, is 0.125(9) meV. This width is comparable to the maximum splitting between the triplon branches, which is why the tails of the modes overlap even at the Γ-point.

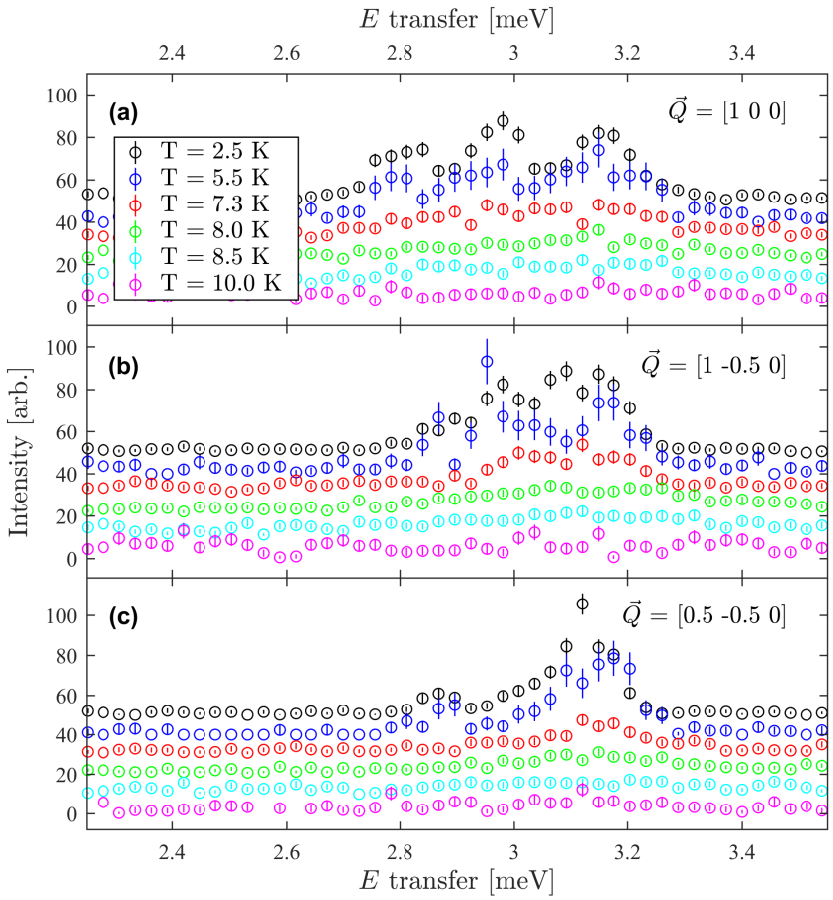

Figure 5.12: Effect of temperature on the dispersion of SCBO at three $\vec{Q}$-points. The data has been averaged over an interval of 0.1 r.l.u. width (except for the total integration around L) and a small offset in intensity has been introduced for clarity. (a) and (b) clearly show three peaks, while in (c) the dispersion is close to being degenerate and the intensity is concentrated in a single peak, around 3.15 meV: the presence of a peak around 2.85 meV in the last panel will be shown to be spurious in the next section.

5.3.1 Alignment of the sample

A number of spurious lines can be seen in the data. For instance in Fig. 5.10(b) two lines can be seen crossing around K = -1, a result in contrast with previous studies of the material (see Fig. 5.5). This was due to misaligned crystal or of crystallites.

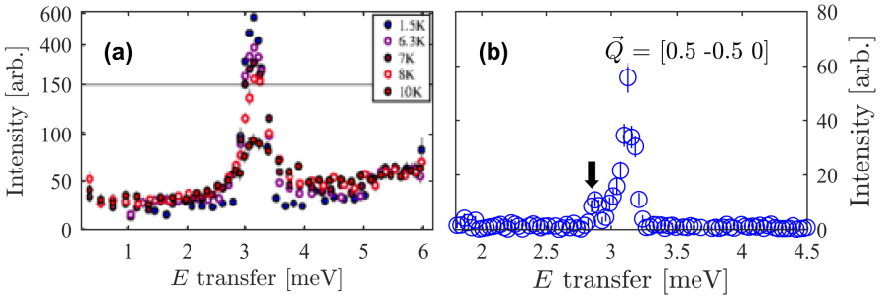

Figure 5.13: Comparison between (a) data from previos experiments [160] and (b) the present data. At $\vec{Q}$ half-integer (i.e. the midpoint of the unit cell) the mode is expected to be fully degenerate (within resolution) by both previous experiments and theoretical considerations; however a small peak, marked with a black arrow, can be seen in our data. This is the result of a misaligned crystallite in the sample.

Figure 5.13 provides a further clear example of a peak appearing at an unexpected energy. This introduces a further challenge in the analysis, as will be explained in the next section.

5.4 Discussion of the data

5.4.1 Fitting procedure

Once the equivalence with previous result in the literature has been established, a fitting procedure is applied here. Due to the misaligned crystals providing spurious triplon lines that cannot be separated from the data, writing a complete cross section is impossible. As these lines are generally weaker than the main branches of the excitation and have slightly different

energies, they could be treated like tails by a fitting procedure. Including these spurious modes is thus crucial if one wants to separate the physical broadening of the modes from the crystal misalignments.

The approach we will follow here instead assumes that the signal at 2.5 K is the cross section. This approach has the advantage that the signal at 2.5 K already including all spurious signals, preventing any unrequired broadening. The procedure is as follows.

- The procedure progresses analyzing one $\vec{Q}$-point at a time at all temperatures. The width of the $\vec{Q}$-binning can be varied, but will be 0.125 r.l.u. for the purpose of this calculation.

- The data at 2.5 K is separated into the background and the triplon excitations. Being the data at the lowest temperature, it is assumed that it presents no broadening and that its width is the instrumental resolution. The data of the triplon excitation is therefore used as a "cross section" $S_{2\mathrm{K}}(\vec{Q}, \hbar\omega)$.

- The cross section at higher temperatures is obtained by scaling and convolving $S_{2\mathrm{K}}(\vec{Q}, \hbar\omega)$. By scaling $S_{2\mathrm{K}}$ we obtain the sharp component, while by scaling and convolving with a Lorentzian we obtain the broad component.

- The fit parameters are the background, sharp intensity, broad intensity and Lorentzian broadening $\Gamma_{\vec{Q}}(T)$.

- As $\Gamma_{\vec{Q}}(T)$ is fitted freely, a map $\Gamma(T, \vec{Q})$ can be obtained.

A further fitting parameter already introduced in previous studies [157, 160] is the shift in energy $\delta\omega$, an upward shift of the center of mass of the triplon with increasing temperature. This empirical parameter accounts for the fact that, as triplons are populated, due to their repulsive nature it becomes more difficult to excite them, which leads to an effective increase in the singlet-to-triplet excitation energy. Previous studies provide maximal values for $\delta\omega$ in the order of magnitude of 0.1 meV, or 10 K.

5.4.2 Presentation of the fits

Two examples of a fit are provided in Fig. 5.14 and 5.15.

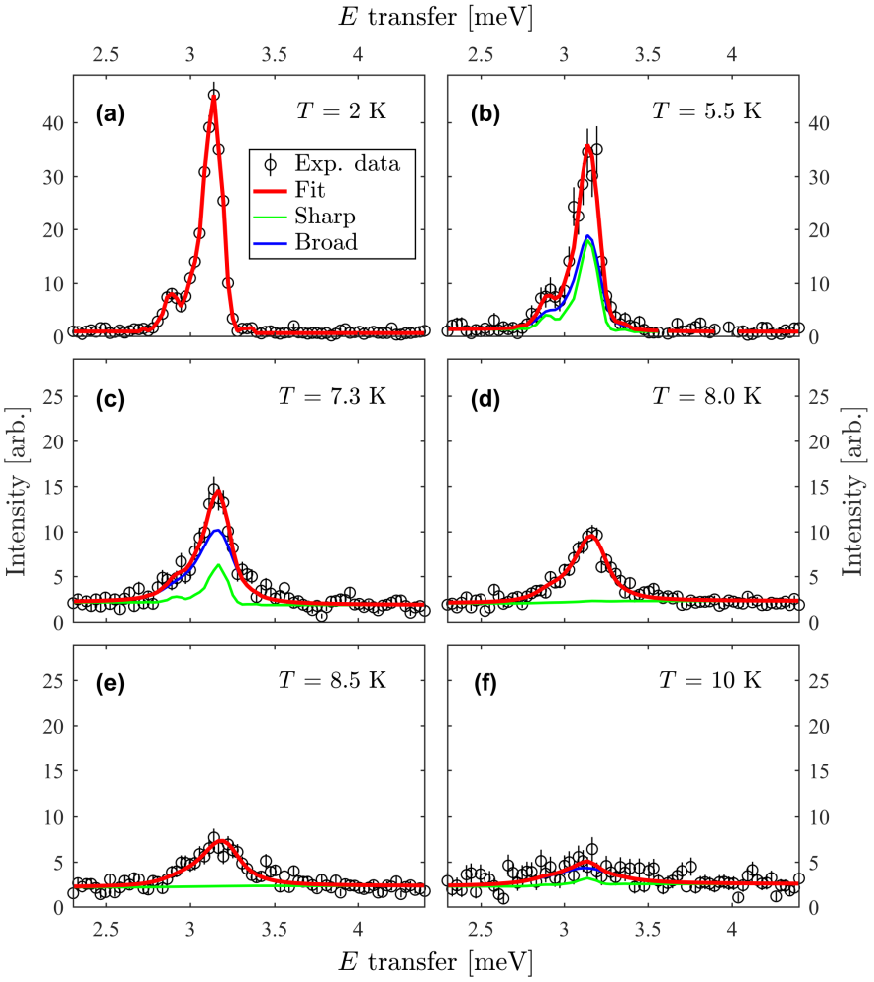

Figure 5.14: Fits of the data at $\vec{Q} = (0.5\ {-0.5}\ 0)$ as a function of temperature, showing the fit as well as the two components - broad and sharp. Already at 5.5 K the sharp component (which dominates the scattering at 2 K) has dropped significantly in intensity, disappearing at 8 K.

There is overall good agreement between the data and the models, resulting in χ^2 between[1] 1.1 and 2.5 as a function of $\vec{Q}$. By averaging over

[1]The value of χ^2 is not entirely representative since it also takes into account the data at 2 K, for which by construction χ^2 is 1.

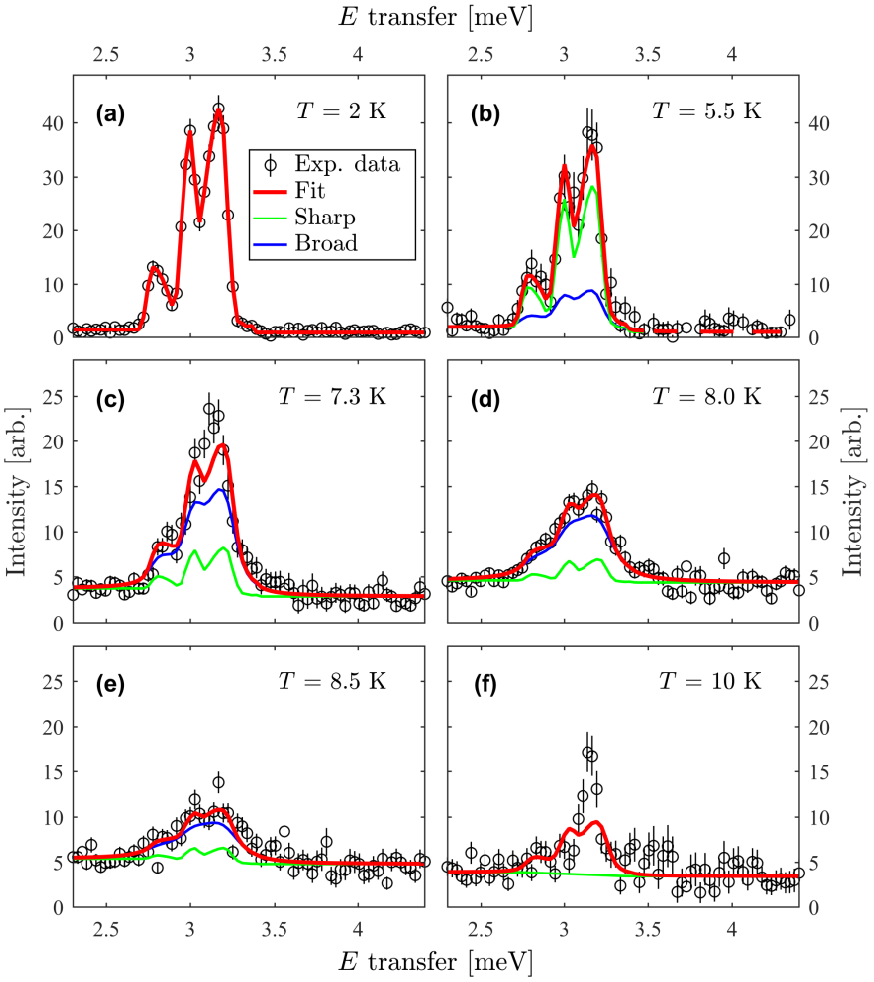

Figure 5.15: Fits of the data at $\vec{Q}$ = (1.0 -0.5 0) as a function of temperature, done as in Fig. 5.14.

$\vec{Q}$ the overall trend for each fitted parameter can be extracted. The overall intensity, as displayed in Fig. 5.16, decreases as a function of temperature, while spectral weight is transferred from the sharp component, which dominates at 2 K (by construction) to the broad component, which becomes dominant and almost exclusive at 8 K. This trend confirms broadly the previous studies on SCBO and it highlights the change in the decay channel of triplons due to their thermal activation.

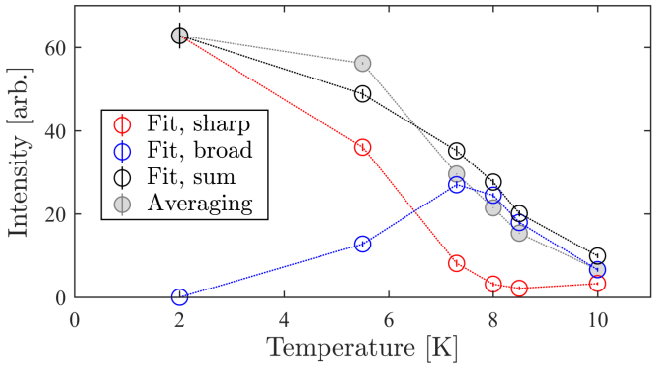

Figure 5.16: Integrated intensities of the sharp and broad components of the fit (red and blue) and their sum (black), averaged over all $\vec{Q}$, compared to intensities calculated by averaging the data (gray). The dotted lines are guides to the eye. While the overall intensity decreases following a roughly sigmoidal curve, there is a transfer of intensity from the sharp component to the broad component, which dominates above 6 K.

Figure 5.17 shows the averaged evolution in temperature of the Lorentzian broadening Γ and of the energy shift $\delta\omega$. As expected from the argument from thermal activation, the broadening increases meaning that the lifetime is decreasing, and the energy shift is positive meaning that new triplons experience an average repulsive force from other triplons.

This consolidates the understanding of the effect of temperature on this compound, providing a coherent and cohesive picture of the effect that a thermal population of triplons has on newly excited triplons.

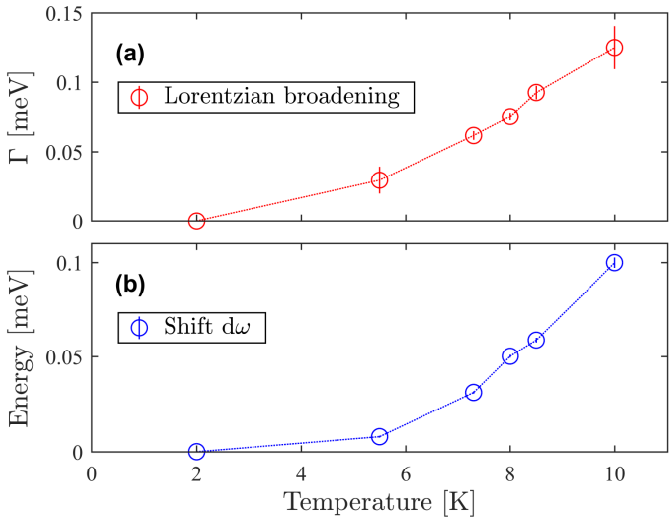

Figure 5.17: Fitted (a) Lorentzian broadening Γ and (b) energy shift dω as a function of temperature, averaged over all $\vec{Q}$. The dotted lines are guides to the eye. Both the broadening and the shift in energy increase continuously with temperature.

5.4.3 $\vec{Q}$-dependence of the decay

While the fitted results already show the trend for Γ to increase with temperature, the $\vec{Q}$-dependence can be studied in more detail. Figure 5.18 shows the change of Γ over $\vec{Q}$-space at each temperature except for 2 K (where, by construction, no broadening is fitted) and for 10 K (where the analysis did not converge). Due to the relatively large errorbars (which cannot be shown in the colormap) the $\vec{Q}$-dependence is noisy and no pattern emerges.

Fig. 5.19 shows Γ at three temperatures along K for $H = 0.5$. The fitted parameters are dominated by the the statistical uncertainty. This analysis is clearly affected by a two-fold problem. Firstly, the broadening is in the same order of magnitude as the intrinsic instrumental resolution, meaning that the experimental statistical quality importantly affects Γ. Furthermore this makes it difficult for the fitting algorithm to separate the broad and sharp components since the are very similar. As a result the fitting procedure had problems converging, as shown in Fig. 5.18(a), where the holes in the

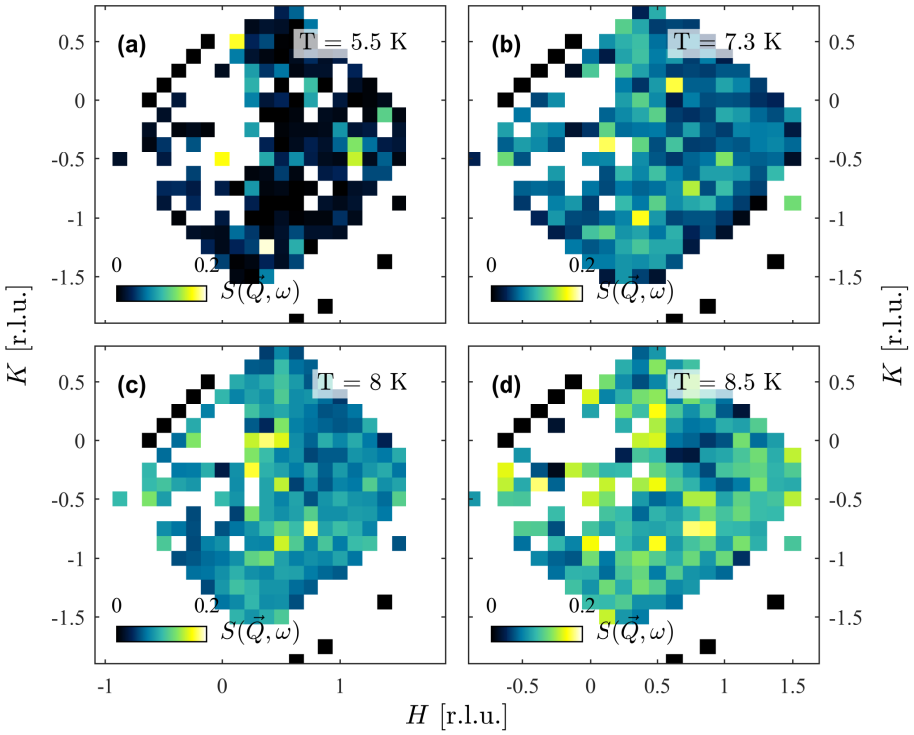

Figure 5.18: Fitted values of the broadening Γ as a function of $\vec{Q}$ at several temperatures. The presence of holes in the map are due to fits that didn't converge.

colormap mark the points where the algorithm failed to produce a reliable value for Γ. At 10 K the data also displays very substantial errorbars since the intensity of the mode has decreased to a point where the artifacts of the background start to dominate. Our estimate of Γ is therefore hindered by the background to signal ratio. It is thus at this point possible to conclude that the Lorentzian broadening Γ does vary with $\vec{Q}$ and that a ToF experiment with a large detector is an ideal tool to investigate this phenomenon, but presently a detailed $\vec{Q}$-map has not been obtained. More will be discussed in the outlook.

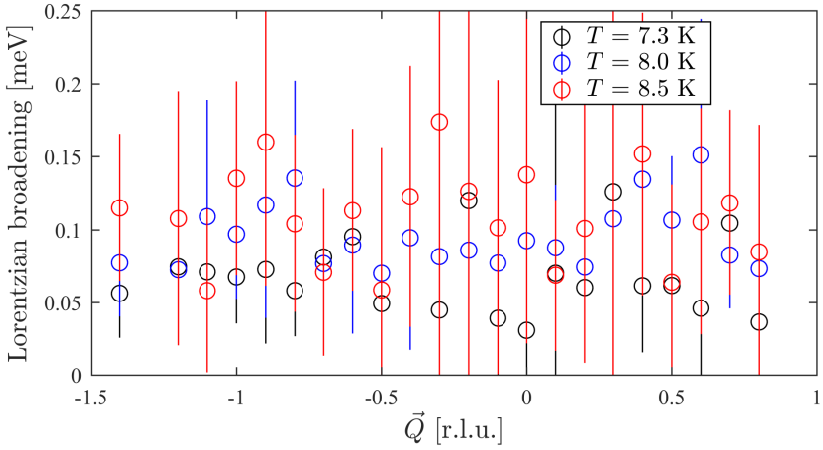

Figure 5.19: Fitted values of the broadening Γ along the main crystallographic directions at all temperatures. The data has been folded according to symmetry over the whole $\vec{Q}$-space. The gray vertical lines mark the M point at (0.5 0) and the X point at (0.5 0.5), and the axis runs in a straight line between these points in steps of 0.125. Shaded areas were added to increase visibility.

5.5 Outlook and conclusions

We have performed an inelastic neutron scattering experiment on SCBO and measured its singlet-to-triplet excitation, obtaining data on a large section of $\vec{Q}$-space. Furthermore, we have characterised the excitation and confirmed

several results already reported in literature. We have studied the temperature dependence of the spectrum in terms of a triplon-to-triplon interaction, reconstructing correctly the drop in intensity of the sharp component and the rise and fall of the broad component. This analysis has allowed us to map the Lorentzian broadening Γ as a function of $\vec{Q}$ along the main axis of a square unit cell.

Despite not being able to provide a reliable value for Γ, these results highlight the power of modern ToF instruments such as LET in investigating detailed aspects of the dynamics of a system. It is conventional wisdom that determining the energy of an excitation for spectroscopy data is the easiest task, as that requires being able to detect a peak position. Determining the intensity (i.e. the spectral weight) with accuracy is a task that demands more statistics than that. Determining the a finite lifetime of a particle requires to reliably measure the tails of the mode and not its peak intensity – and, in our case, to differentiate a mode with the instrumental resolution from a broadened mode. The errorbars are inversely proportionately to the square root of the counting time, making it increasingly more difficult to improve the data.

While the results of this study might not deliver all the information needed to reconstruct a complete picture of the decay mechanics of triplons in SCBO and its $\vec{Q}$-dependence, we feel that it is a very strong illustration of the power of an instrument such as LET, and of its present limitation.

Chapter 6

Conclusions and outlook

During this thesis I have investigated three magnetic systems of varying dimensionality and interacting Hamiltonians using the technique of inelastic neutron scattering in order to characterise their excitations. Furthermore, the excitations have been modelled mathematically and an agreement between theoretical predictions and observed data has been established.

The $\vec{Q}$-dependence of the lifetime of triplons in SCBO remains an open question due to the inconclusivity of our results due to the technical difficulties of such an experiment: at an instrument such as LET, which is required to sample large sections of $\vec{Q}$-space, the energy resolution at the triplon energy can be comparable to the splitting between triplon modes, while the lifetime of the particle can only be measured in the tails of the lineshape. However, applying a magnetic field splits the triplon modes so that their tails no longer overlap. I have participated in a series of experiment performed on LET by Diane Lançon, of EPFL, where the in-field $\vec{Q}$-dependence of the triplon mode has been measured with success.

Our study of $RbCoCl_3$ has highlighted the importance of the local exchange geometries on Ising chains that rely on a staggered field to order: this is of particular interest in a frustrated hexagonal lattice where the temperature allows to select different configurations of the frustrated planes – namely creating an ordered phase and two disordered phases. We have shown how staggered fields change with temperature, and as a consequence how the spectrum is modified by displaying more or less branches of bound domain wall excitations, i.e. solitons. With temperature solitons acquire a finite lifetime and a reduced mobility, two effects that we approximate us-

ing a phenomenological description but that offer an opportunity for more theoretical studies in the properties of the thermal Ising chain.

This co-dependence between frustration, staggered fields and magnetic modes should be expected to be observed in many of the ABX_3 compounds mentioned through this thesis (e.g. $CsCoCl_3$), as they all share a comparable Hamiltonian, but it can be extended to other compounds: the candidates are in general Ising chains on frustrated lattices (for instance the Kagome lattice). The first question is whether this compounds as well exhibit two magnetic phase transitions, and whether the dynamic correlations in these two magnetic phases are meaningfully distinct.

Ising chains are furthermore relevant because of their QPT (in a perpendicular magnetic field strong enough). While the critical magnetic field in $RbCoCl_3$ cannot be experimentally achieved with the current technology in a neutron scattering facility, it can be expected that frustration will no longer play a role in that magnetic state ($H_C > J > J_{nn}$) and so this temperature-dependence of the spectrum might be expected not to be observed. Still, direct observation of this quantum phase transition, and of the quantum critical region, are required before reaching any conclusion.

We have measured the spin-wave spectrum of the thermal Hall effect ferromagnet $Lu_2V_2O_7$, verified a minimal model of the Hamiltonian and provided values for its two dominant interactions, J and D. This will stimulate more discussion on the subject of this whole class of insulating pyrochlores. While we have proven that a minimal model is sufficient to explain the main features of the dispersion, we cannot exclude the presence of next-nearest neighbour exchange, or estimate their magnitude or their effect. Equally, there are other terms of the Hamiltonian that could be included in a description of the magnetic system: for instance a recent study [166], using a combination of DFT and exact diagonalization of Hubbard-like finite clusters, studied the Hamiltonian

$$\mathcal{H}_{spin} = \mathcal{J}(\vec{S_j} \cdot \vec{S_k}) + \mathcal{D}_{jk} \cdot (\vec{S_j} \times \vec{S_k}) + \vec{S_j}^{\,T} \cdot \hat{\mathcal{K}}_{jk} \cdot \vec{S_k} \tag{6.1}$$

and concluded that $|\hat{\mathcal{K}}|/|\mathcal{J}| = 0.02$, i.e. below the instrumental resolution used in our experiment. Their estimate for $|\vec{D}|/|\mathcal{J}|$ was 0.07, less than a half of the value of 0.18(1).

Many outstanding questions remain in the context of the broader research on the magnon Hall effect. For the pyrochlores, one particularly important question is the direction of the DMI [167], which we have been unable to establish via a direct observation of the spectrum due to the symmetry of the spin waves with respect to the sign of the DMI. Understanding this detail is crucial in order to explain some thermal conductivity data, and to lead to the developement of magnon topological insulators [121], which rely on the interface between materials of different sign of the DMI.

While other novel equivalent phenomena have been suggested for these pyrochlores, such as the Nernst effect [168, 169], another relevant problem is finding other systems where the magnon Hall effect can be observed. As it relies on the DMI there are restrictions to the possible symmetries and to magnetic ions with a relevant spin-orbit coupling. A further experimental constraint is that the magnitude of the magnon contribution to the thermal conductivity must be measurable when compared to the other contributions: while a phonon contribution from the lattice can't be avoided, it is better to avoid conducting systems, as the electronic contribution to thermal conductivity tends to be dominant over all others.

In terms of dimensionality, the magnon Hall effect should not be expected to play a significant role in one-dimensional systems (as the one-dimensionality of the correlation will prevent magnons from experiencing any perpendicular drift), there have been suggestions for the observation of the magnon Hall effect in a two-dimensional Kagome lattice [123] or on the honeycomb lattice [170], potentially opening a new field in low-dimensional magnetism.

Chapter 7

Acknowledgements

The only thing left to do is to thank every person who contributed to my thesis and made it possible. Although there are too many to be mentioned,

I would like to start by profusely thanking my supervisors, Professors Des McMorrow and Christian Rüegg. Their continuous guidance, suggestions, advice and patience have been essential during my PhD, which literally couldn't have happened without them.

For my collaborative study of $RbCoCl_3$ I would like to thank Nora Hänni and Eva Hirtenlechner. Nora also grew the crystals, and for that I also thank her group, based in Bern and headed by Karl Krämer. For $Lu_2V_2O_7$ I'd like to thank Robin Perry, who grew the crystals, Zhao Feng and Sebastian Guerrero, who helped with the experiments and with the analysis. For SCBO I shall thank Diane Lançon and Paul Freeman, who spent several weeks with me in an experimental cabin.

Special thanks go to Duc Le, Toby Perring and Simon Ward, who helped me sorting out my code and answered many questions, making my MATLAB scripts a better place.

My heartfelt thanks go to the instrumental scientists who made the experiments possible and succesfull: in alphabetical order, Devashibhai Adroja, Rob Bewley, Franz Demmel, Mechthild Enderle, Tatiana Guidi, Vladimir Pomjakushin, Louis-Pierre Regnault, Uwe Stuhr and Helen Walker. Furthermore, I would like to signal my boundless appreciation to the technicians at ISIS, PSI and ILL, who keep the facilities running.

I shall also thank my colleagues and friends, who were always happy to listen to my problems and sometimes talk about theirs. In alphabetical or-

der, Alexander, Christian, Gianluca, Giulio, James, Manuel, Martin, Nikola, Noriko, Paul and Sándor.

A deeply felt thanks to my family: my parents and my three brothers, my uncles and my aunt, and my grandmother.

And the last acknowledgment, and certainly not the least, goes to my partner Kim, who stood by me stoically during this last year.

References

[1] J. D. Jackson, *Classical Electrodynamics* (John Wiley & Sons, Inc., 1962).

[2] R. Feynman, *The Feynman Lectures on Physics* (Basic Books, 1963).

[3] J. C. Maxwell, Philos. Trans. R. Soc. **155**, 459 (1865).

[4] J. C. Maxwell, *A Treatise on Electricity and Magnetism* (Oxford at the Clarendon Press, 1873).

[5] J. C. Maxwell, *The Electrical Researches of the Honourable Henry Cavendish* (Cambridge: University Press, 1879).

[6] O. Heaviside, Philos. Trans. R. Soc. **183A**, 423 (1892).

[7] O. Heaviside, Philos. Mag. **5**, 324 (1889).

[8] E. Ising, Zeitschrift für Phys. **31**, 253 (1925).

[9] W. Heisenberg, Zeitschrift für Phys. **49**, 619 (1928).

[10] I. Dzyaloshinsky, J. Phys. Chem. Solids **4**, 241 (1958).

[11] T. Moriya, Phys. Rev. **120**, 91 (1960).

[12] R. L. Carlin, *Magnetochemistry* (Springer Berlin Heidelberg, 1986).

[13] L. J. de Jongh and A. R. Miedema, Adv. Phys. **23**, 1 (1974).

[14] M. Dirken and L. de Jongh, Solid State Commun. **64**, 1201 (1987).

[15] G. E. Everett and P. Streit, J. Magn. Magn. Mater. **12**, 277 (1979).

[16] W. J. Hu, J. Du, B. Li, Q. Zhang, and Z. D. Zhang, Appl. Phys. Lett. **92**, 192505 (2008).

[17] P. W. Anderson, Phys. Rev. **86**, 694 (1952).

[18] P. W. Anderson, Phys. Rev. **102**, 1008 (1956).

[19] X. Obradors *et al.*, Solid State Commun. **65**, 189 (1988).

[20] S. Blundell, *Magnetism in condensed matter* (Oxford Univ. Press, 2001).

[21] C. Lacroix, P. Mendels, and F. Mila, *Introduction to Frustrated Magnetism* (Springer, 2011).

[22] A. P. Ramirez, Czechoslov. J. Phys. **46**, 3247 (1996).

[23] I. S. Hagemann, Q. Huang, X. P. A. Gao, A. P. Ramirez, and R. J. Cava, Phys. Rev. Lett. **86**, 894 (2001).

[24] R. Moessner and J. T. Chalker, Phys. Rev. Lett. **80**, 2929 (1998).

[25] S. T. Bramwell and M. J. P. Gingras, Science **294**, 1495 (2001).

[26] D. Bitko, T. F. Rosenbaum, and G. Aeppli, Phys. Rev. Lett. **77**, 940 (1996).

[27] S. Sachdev, Phys. World **12**, 33 (1999).

[28] M. Greiner, O. Mandel, T. Esslinger, T. W. Hänsch, and I. Bloch, Nature **415**, 39 (2002).

[29] A. Osterloh, L. Amico, G. Falci, and R. Fazio, Nature **416**, 608 (2002).

[30] M. Vojta, Reports Prog. Phys. **66**, 2069 (2003).

[31] S. Sachdev, Quantum Phase Transitions, in *Handb. Magn. Adv. Magn. Mater.*, John Wiley and Sons, Ltd, 2007.

[32] https://commons.wikimedia.org.

[33] http://sachdev.physics.harvard.edu/physworld/.

[34] G. L. Squires, *Introduction to the Theory of Thermal Neutron Scattering*, Third ed. (Cambridge University Press, 2012).

[35] S. W. Lovesey, *Theory of Neutron Scattering from Condensed Matter* (Oxford University Press, 1971).

[36] S. N. E. Ward, *Spin Ladder Physics and the Effect of Random Bond Disorder*, PhD thesis, University College London, 2015.

[37] N. Hänni *et al.*, submitted to PRB, 2015.

[38] R. Coldea *et al.*, Science **327**, 177 (2010).

[39] B. Grenier *et al.*, Phys. Rev. Lett. **114**, 017201 (2015).

[40] N. Hänni, *Crystal Structures and Magnetic Interactions of the Ising Type Co2+ Halides RbCoCl3 and Ba4Co2Cl12*, Master thesis, Universität Bern, 2012.

[41] E. Hirtenlechner, *Neutron scattering studies of excitations in spin chains*, PhD thesis, ETH Zürich, 2014.

[42] I. Cabrera *et al.*, Phys. Rev. B **90**, 14418 (2014).

[43] N. J. Robinson, F. H. L. Essler, I. Cabrera, and R. Coldea, Phys. Rev. B **90**, 174406 (2014).

[44] N. Ishimura and H. Shiba, Prog. Theor. Phys. **63**, 743 (1980).

[45] O. Arnold *et al.*, Nucl. Instruments Methods Phys. Res. Sect. A Accel. Spectrometers, Detect. Assoc. Equip. **764**, 156 (2014).

[46] Available at http://www.mantidproject.org.

[47] Available at http://horace.isis.rl.ac.uk.

[48] D. W. Hone and P. M. Richards, Annu. Rev. Mater. Sci. **4**, 337 (1974).

[49] M. Steiner, J. Villain, and C. G. Windsor, Adv. Phys. **25**, 87 (1976).

[50] R. J. Birgeneau and G. Shirane, Phys. Today **31**, 32 (1978).

[51] H. Bethe, Zeitschrift für Phys. **71**, 205 (1931).

[52] L. Hulthén, Ark. Mat. Astr. Fys. **26A**, 11 (1938).

[53] R. Orbach, Phys. Rev. **112**, 309 (1958).

[54] J. Des Cloizeaux and J. J. Pearson, Phys. Rev. **128**, 2131 (1962).

[55] J. Des Cloizeaux and M. Gaudin, J. Math. Phys. **7**, 1384 (1966).

[56] Y. Endoh, G. Shirane, R. J. Birgeneau, P. M. Richards, and S. L. Holt, Phys. Rev. Lett. **32**, 170 (1974).

[57] B. D. Metcalf, Phys. Lett. A **46**, 325 (1974).

[58] M. Kaburagi and J. Kanamori, Proc. 2nd Int. Conf. Solid Surfaces, Kyoto , 145 (1974).

[59] Y. Tanaka and N. Uryû, J. Phys. Soc. Japan **39**, 825 (1975).

[60] W. B. Yelon, D. E. Cox, and M. Eibschütz, Phys. Rev. B **12**, 5007 (1975).

[61] M. Mekata, J. Phys. Soc. Japan **42**, 76 (1977).

[62] H. Shiba, Prog. Theor. Phys. **64**, 466 (1980).

[63] W. Breitling, W. Lehmann, T. P. Srinivasan, R. Weber, and U. Dürr, Solid State Commun. **24**, 267 (1977).

[64] W. Breitling, W. Lehmann, and R. Weber, J. Magn. Magn. Mater. **10**, 25 (1979).

[65] D. J. Scalapino, Y. Imry, and P. Pincus, Phys. Rev. B **11**, 2042 (1975).

[66] W. P. Lehmann, W. Breitling, and R. Weber, J. Phys. C Solid State Phys. **14**, 4655 (1981).

[67] F. Matsubara, S. Inawashiro, and H. Ohhara, J. Phys. Condens. Matter **3**, 1815 (1991).

[68] J. P. Goff, D. A. Tennant, and S. E. Nagler, Phys. Rev. B **52**, 15992 (1995).

[69] H. Shiba, Y. Ueda, K. Okunishi, S. Kimura, and K. Kindo, J. Phys. Soc. Japan **72**, 2326 (2003).

[70] N. Todoroki and S. Miyashita, J. Phys. Soc. Japan **73**, 412 (2004).

[71] A. Oosawa, Y. Nishiwaki, T. Kato, and K. Kakurai, J. Phys. Soc. Japan **75**, 015002 (2006), 0511179.

[72] S. E. Nagler, W. J. L. Buyers, R. L. Armstrong, and B. Briat, Phys. Rev. B **27**, 1784 (1983).

[73] D. J. Lockwood, I. W. Johnstone, H. J. Labbe, and B. Briat, J. Phys. C Solid State Phys. **16**, 6451 (1983).

[74] Available online at http://www2.cpfs.mpg.de/.

[75] A. J. A. James, W. D. Goetze, and F. H. L. Essler, Phys. Rev. B **79**, 214408 (2009).

[76] Available at https://www.ill.eu/instruments-support/computing-for-science/cs-software/all-software/matlab-ill/spec1d/.

[77] S. G. Brush, Rev. Mod. Phys. **39**, 883 (1967).

[78] L. Onsager, Phys. Rev. **65**, 117 (1944).

[79] I. Manno, *Introduction to the Monte-Carlo method* (Akadémiai Kiadó, 1999).

[80] M. E. J. Newman and G. T. Barkema, *Monte Carlo Methods in Statistical Physics* (Oxford University Press: New York, USA, 1999).

[81] A. A. Markov, Izv. Fiz. Obs. pri Kazan. Univ. **2**, 135 (1906).

[82] N. Metropolis and S. Ulam, J. Am. Stat. Assoc. **44**, 335 (1949).

[83] N. Metropolis, A. W. Rosenbluth, M. N. Rosenbluth, A. H. Teller, and E. Teller, J. Chem. Phys. **21**, 1087 (1953).

[84] W. K. Hastings, Biometrika **57**, 97 (1970).

[85] N. Metropolis, Los Alamos Sci. **15**, 125 (1987).

[86] S. Chib and E. Greenberg, Am. Stat. **49**, 327 (1995).

[87] A. Baumgärtner *et al.The Monte Carlo method in condensed matter physics* Vol. 71 (Springer Science & Business Media, 2012).

[88] F. Matsubara, A. Sato, O. Koseki, and T. Shirakura, Phys. Rev. Lett. **78**, 3237 (1997), 9704114.

[89] O. Koseki and F. Matsubara, J. Phys. Soc. Japan **66**, 322 (1997).

[90] O. Koseki and F. Matsubara, J. Phys. Soc. Japan **69**, 1202 (2000).

[91] J. S. Gardner, M. J. P. Gingras, and J. E. Greedan, Rev. Mod. Phys. **82**, 53 (2010).

[92] M. J. Harris, S. T. Bramwell, D. F. McMorrow, T. Zeiske, and K. W. Godfrey, Phys. Rev. Lett. **79**, 2554 (1997).

[93] A. P. Ramirez, A. Hayashi, R. J. Cava, R. Siddharthan, and B. S. Shastry, Nature **399**, 333 (1999).

[94] B. C. den Hertog and M. J. P. Gingras, Phys. Rev. Lett. **84**, 3430 (2000).

[95] S. T. Bramwell *et al.*, Phys. Rev. Lett. **87**, 47205 (2001).

[96] T. Fennell *et al.*, Phys. Rev. B **70**, 134408 (2004).

[97] C. Castelnovo, R. Moessner, and S. L. Sondhi, Nature **451**, 42 (2008).

[98] T. Yavors'kii, T. Fennell, M. J. P. Gingras, and S. T. Bramwell, Phys. Rev. Lett. **101**, 37204 (2008).

[99] T. Fennell *et al.*, Science **326**, 415 (2009).

[100] B. Canals and C. Lacroix, Phys. Rev. Lett. **80**, 2933 (1998).

[101] I. Mirebeau *et al.*, Nature **420**, 54 (2002).

[102] B. D. Gaulin, J. N. Reimers, T. E. Mason, J. E. Greedan, and Z. Tun, Phys. Rev. Lett. **69**, 3244 (1992).

[103] O. Tchernyshyov, R. Moessner, and S. L. Sondhi, Phys. Rev. Lett. **88**, 67203 (2002).

[104] S. T. Bramwell, M. J. P. Gingras, and J. N. Reimers, J. Appl. Phys **75**, 5523 (1994).

[105] J. D. M. Champion *et al.*, Phys. Rev. B **68**, 20401 (2003).

[106] Y. Shimakawa, Y. Kubo, and T. Manako, Nature **379**, 53 (1996).

[107] M. A. Subramanian *et al.*, Science **273**, 81 (1996).

[108] H. Sakai *et al.*, J. Phys. Condens. Matter **13**, L785 (2001).

[109] Y. Yamashita and K. Ueda, Phys. Rev. Lett. **85**, 4960 (2000).

[110] A. A. Biswas, Y. Jana, J. Alam, and P. Das, AIP Conf. Proc. **963**, 963 (2013).

[111] H. D. Zhou *et al.*, Phys. Rev. B **77**, 020411 (2008).

[112] K.-Y. Choi *et al.*, Phys. Rev. B **82**, 054430 (2010).

[113] H. J. Xiang *et al.*, Phys. Rev. B **83**, 174402 (2011).

[114] H. Ichikawa *et al.*, J. Phys. Soc. Japan **74**, 1020 (2005).

[115] T. Kiyama *et al.*, Phys. Rev. B **73**, 1 (2006).

[116] S. Miyahara, A. Murakami, and N. Furukawa, Journal of Molecular Structure **838**, 223 (2007), Proceedings of the Symposium on the Jahn-Teller Effect.

[117] T. Shiraoka *et al.*, AIP Conf. Proc. **850**, 1231 (2006).

[118] Y. Onose *et al.*, Science **329**, 297 (2010).

[119] R. Matsumoto and S. Murakami, Phys. Rev. Lett. **106**, 197202 (2011).

[120] T. Ideue *et al.*, Phys. Rev. B **85**, 134411 (2012).

[121] A. Mook, J. Henk, and I. Mertig, Phys. Rev. B **90**, 024412 (2014).

[122] A. Mook, J. Henk, and I. Mertig, Phys. Rev. B **89**, 134409 (2014).

[123] A. Mook, J. Henk, and I. Mertig, Phys. Rev. B **91**, 174409 (2015).

[124] E. H. Putley and G. Landwehr, J. Electrochem. Soc. **109**, 42C (1962).

[125] T. Amundsen, Philos. Mag. **20**, 687 (1969).

[126] R. Fletcher and A. J. Friedman, Phys. Rev. B **8**, 5381 (1973).

[127] C. Strohm, G. L. J. A. Rikken, and P. Wyder, Phys. Rev. Lett. **95**, 155901 (2005).

[128] J. N. Lalena and D. A. Cleary, *Principles of Inorganic Materials Design* (Wiley, 2010).

[129] L. Zhang, J. Ren, J.-S. Wang, and B. Li, Phys. Rev. B **87**, 144101 (2013).

[130] M. Mochizuki *et al.*, Nat. Mater. **13**, 241 (2014).

[131] T. Shin-ike, G. Adachi, and J. Shiokawa, Mat . Res . Bull . **12**, 1149 (1977).

[132] L. Soderholm and J. E. Greedan, Mater. Res. Bull. **17**, 707 (1982).

[133] L. Soderholm, C. V. Stager, and J. E. Greedan, J. Solid State Chem. **43**, 175 (1982).

[134] T. Holstein and H. Primakoff, Phys. Rev. **58**, 1098 (1940).

[135] M. Rotter, J. Magn. Magn. Mat. **Suppl.**, E481 (2004).

[136] M. Rotter, M. Doerr, M. Loewenhaupt, and P. Svoboda, J. Appl. Phys. **91**, 8885 (2002).

[137] A. Severing *et al.*, Phys. Rev. B **83**, 155112 (2011).

[138] M. Charilaou, D. Sheptyakov, J. F. Löffler, and A. U. Gehring, Phys. Rev. B **86**, 24439 (2012).

[139] P. S. Normile *et al.*, Phys. Rev. B **88**, 54413 (2013).

[140] K. Balamurugan *et al.*, Phys. Rev. B **90**, 104412 (2014).

[141] Available online at http://tobyfit.isis.rl.ac.uk/.

[142] J. K. V. E. Dmitrienko, E. N. Ovchinnikova and K. Ishida, JETP Letters **92**, 383 (2010).

[143] V. E. Dmitrienko *et al.*, Nat. Phys. **10**, 202 (2014).

[144] B. S. Shastry and B. Sutherland, Phys. Rev. Lett. **47**, 964 (1981).

[145] B. S. Shastry and B. Sutherland, Phys. B+C **108**, 1069 (1981).

[146] E. Müller-Hartmann, R. Singh, C. Knetter, and G. Uhrig, Phys. Rev. Lett. **84**, 1808 (2000).

[147] C. H. Chung, J. B. Marston, and S. Sachdev, Phys. Rev. B **64**, 134407 (2001).

[148] H. Kageyama *et al.*, Phys. Rev. Lett. **82**, 3168 (1999).

[149] K. Sparta *et al.*, Eur. Phys. J. B **19**, 507 (2001).

[150] H. Kageyama, *An Experimental Realization of the Shastry-Sutherland Model* (Springer Berlin Heidelberg, Berlin, Heidelberg, 2005), pp. 611–651.

[151] S. Yoshii *et al.*, Phys. Rev. Lett. **101**, 087202 (2008).

[152] F. Levy *et al.*, EPL **81**, 67004 (2008).

[153] M. Takigawa *et al.*, Phys. Rev. Lett. **110**, 067210 (2013).

[154] J. Dorier, K. Schmidt, and F. Mila, Phy. Rev. Lett. **101**, 250402 (2008).

[155] A. Koga, J. Phys. Soc. Japan **69**, 3509 (2000).

[156] A. Läuchli, S. Wessel, and M. Sigrist, Phys. Rev. B **66**, 014401 (2002).

[157] M. E. Zayed, *Novel States in Magnetic Materials under Extreme Conditions: A High Pressure Neutron Scattering Study of the Shastry-Sutherland compound SrCu2(BO3)2*, PhD thesis, EPFL Lausanne, 2010.

[158] S. Miyahara and K. Ueda, Phys. Rev. Lett. **82**, 3701 (1999).

[159] O. Cépas *et al.*, Phys. Rev. Lett. **87**, 167205 (2001).

[160] M. E. Zayed *et al.*, Phys. Rev. Lett. **113**, 067201 (2014).

[161] Y. F. Cheng, O. Cépas, P. W. Leung, and T. Ziman, Phys. Rev. B **75**, 144422 (2007).

[162] K. Kakurai *et al.*, *Quantum Properties of Low-Dimensional Antiferromagnets* (Kyushu University Press, 2002).

[163] K. Kakurai *et al.*, Prog. Theor. Phys. Supp **159**, 22 (2005).

[164] S. Miyahara and K. Ueda, J. Soc. Phys. Jpn. Suppl. **72** (2000).

[165] C. Rüegg *et al.*, Phys. Rev. Lett. **95**, 267201 (2005).

[166] K. Riedl, D. Guterding, H. O. Jeschke, M. J. P. Gingras, and R. Valentí, Phys. Rev. B **94**, 014410 (2016).

[167] N. Arakawa, (2016), 1606.03822.

[168] V. A. Zyuzin and A. A. Kovalev, (2016), 1606.03088.

[169] A. A. Kovalev and V. Zyuzin, Phys. Rev. B **93**, 161106 (2016).

[170] S. A. Owerre, (2016), 1603.04331.